Transducer Arrays for 3D Ultrasound Computed Tomography

Zur Erlangung des akademischen Grades eines

DOKTORS DER INGENIEURWISSENSCHAFTEN
(Dr.-Ing.)

von der KIT-Fakultät für
Elektrotechnik und Informationstechnik
des Karlsruher Instituts für Technologie (KIT)

angenommene

DISSERTATION

von

M.Sc. Martin Angerer
geb. in Peißenberg

Tag der mündlichen Prüfung:	06. Oktober 2022
Hauptreferent:	Prof. Dr. Marc Weber
Korreferent:	Prof. Dr. Ulrich Lemmer

Abstract

Ultrasound computed tomography (USCT) is a promising imaging method for early breast cancer detection. A third-generation 3D USCT device (3D USCT III) is currently under development at the Karlsruhe Institute of Technology. The transducer arrays are among the most critical and technologically challenging components of this device. They have to enable pseudo-random positioning of single transducers, exhibit high bandwidths, large opening angles, isotropic sound emissions and comply with medical device regulations.

This thesis presents the realization of new transducer array systems (TAS III) for 3D USCT. This includes the definition of requirements, system design, automated manufacturing, characterization and design optimization. The core elements of the TAS III design are piezocomposite disks, containing 18 piezoelectric fibers spatially distributed in polymer. Additional disks for acoustic matching and backing were attached to finalize the arrays. A semi-automated manufacturing process was developed to produce the required 256 TAS III. Quantitative quality evaluations showed that more than 96% of the produced transducers were fully functional. The amplitude and phase angle of the generated acoustic field of 54 transducers were measured and analyzed. Most of the defined requirements were met. A mean center frequency of 2.6 MHz was determined, with a -10 dB fractional bandwidth of 134% resulting from two distinct vibration modes. Full 3D measurements showed isotropic sound emissions with a mean opening angle of 42.8°.

Advanced models were developed for design analysis and optimization. Minor changes in length and diameter of the piezoelectric fibers and a higher lateral damping were found to improve the performance to some extent. The limited possibility for further improvements showed that the TAS III design is close to

the achievable optimum. Alternative transducer technologies were explored to overcome fundamental limitations of the piezoelectric fiber composites with respect to opening angle and bandwidth. Replacing the fibers with a single-crystal piezoelectric material promises an increase in bandwidth by 35%, but requires extensive adjustments in the manufacturing process. Characterizations of micromachined ultrasound transducers showed a significant increase in opening angle, but lower emitted sound pressures. Nevertheless, the properties and available design freedom makes this transducer technology very promising for future 3D USCT generations.

The designed and realized TAS III proved to be well-suited for the intended use and were implemented in two 3D USCT III devices. Extensive clinical tests will follow to assess the sensitivity and specificity of this new 3D ultrasound imaging method.

Kurzfassung

Die Ultraschall-Computertomographie (USCT) ist ein vielversprechendes medizinisches Bildgebungsverfahren zur Früherkennung von Brustkrebs. Am Karlsruher Institut für Technologie wird derzeit ein Gerät der dritten Generation (3D-USCT-III) für 3D-Aufnahmen entwickelt. Unter den kritischsten und technologisch anspruchsvollsten Komponenten dieses Geräts sind die Schallwandlerarrays. Diese müssen eine pseudozufällige Positionierung einzelner Wandler ermöglichen, hohe Bandbreiten, große Öffnungswinkel und eine isotrope Schallabstrahlung aufweisen sowie den Vorschriften für Medizinprodukte genügen.

In dieser Arbeit wird die Realisierung neuer Schallwandlerarrays (TAS-III) für die 3D-USCT-Bildgebung umfassend vorgestellt. Dies beinhaltet die Definition von Anforderungen, Systemdesign, automatisierte Fertigung, Charakterisierung und Entwurfsoptimierung. Kernelement des TAS-III-Designs sind Scheiben aus piezoelektrischen Verbundwerkstoffen, die 18 in Polymer eingebettete, räumlich verteilte piezokeramische Fasern enthalten. Zusätzliche Scheiben zur akustischen Anpassung und Dämpfung werden auf beiden Seiten angebracht, um die Arrays zu finalisieren. Für die Herstellung der benötigten 256 TAS-III wurde ein teilautomatisierter Fertigungsprozess entwickelt. Quantitative Qualitätsprüfungen ergaben, dass mehr als 96% der produzierten Wandler voll funktionsfähig waren. Die Amplitude und der Phasenwinkel des akustischen Feldes von 54 Wandlern wurden gemessen und ausgewertet. Die meisten der definierten Anforderungen wurden erfüllt. Es wurde eine mittlere Mittenfrequenz von 2,6 MHz, mit einer fraktionellen Bandbreite von 134% bei -10 dB ermittelt. Die Bandbreite resultiert dabei aus zwei unterschiedlichen Schwingungsmoden. Messungen in 3D zeigten isotrope Abstrahlcharakteristiken mit einem mittleren Öffnungswinkel von 42,8°.

Für die Analyse und Optimierung des Designs wurden verschiedene Modellierungsansätze entwickelt. Geringfügige Änderungen der Länge und des Durchmessers der piezoelektrischen Fasern sowie eine höhere laterale Dämpfung konnten die Leistung in gewissem Maße verbessern. Der Umfang weiterer möglicher Verbesserungen zeigte jedoch, dass das TAS-III Design nahe am erreichbaren Optimum liegt. Alternative Wandlertechnologien wurden untersucht, um die grundsätzlichen Grenzen von Verbundwerkstoffen bestehend aus piezoelektrischen Fasern in Bezug auf Öffnungswinkel und Bandbreite zu überwinden. Der Ersatz der Fasern durch einkristalline piezoelektrische Materialien verspricht eine Erhöhung der Bandbreite um 35%, erfordert jedoch umfangreiche Anpassungen in den Herstellungsprozessen. Die Charakterisierung von mikromechanischen Ultraschallwandlern ergab eine signifikante Vergrößerung des Öffnungswinkels, aber geringere erzeugte Schalldrücke. Dennoch machen die Eigenschaften und die verfügbare Designfreiheit diese Schallwandlertechnologie sehr vielversprechend für zukünftige 3D-USCT- Generationen.

Die entworfenen und realisierten TAS-III erwiesen sich als rundum geeignet für den vorgesehenen Einsatz und wurden in zwei 3D-USCT-III-Geräten integriert. Ausführliche klinische Tests werden in naher Zukunft durchgeführt, um die Sensitivität und Spezifität dieser neuartigen 3D-Ultraschallbildgebungsmethode zu bewerten.

Contents

Abstract i

Kurzfassung iii

1 Introduction and Motivation 1
1.1 3D Ultrasound Computed Tomography 2
1.2 Context and Aim of this Thesis 5

2 Ultrasound Transducer Fundamentals 9
2.1 Piezoelectric Properties 9
2.2 Piezoelectric Transducers 13
2.2.1 Acoustic Matching 15
2.2.2 Acoustic Backing 17
2.3 Transducer Characteristics 18
2.4 State of the Art of Transducers for USCT 20

3 Transducer Array Design and Production 25
3.1 Design History of TAS 25
3.2 Design Requirements 29
3.3 New Array Design 31
3.3.1 Composite Disk 33
3.3.2 PCB Disk 34
3.3.3 Matching Disk 35
3.3.4 Acoustic Backing 36
3.4 Production Process 38
3.4.1 Process Overview 39
3.4.2 Challenges 41

3.4.3 Stack Assembly . . . 44
3.4.4 Packaging . . . 47
3.5 Summary and Discussion . . . 50

4 Quality Control and Inspection . . . 53
4.1 Electromechanical Impedance Characteristics . . . 53
4.2 Quality Control Measure . . . 55
4.2.1 Dataset from Manufacturing States . . . 56
4.2.2 Classification Method . . . 58
4.2.3 Results . . . 63
4.3 Temperature Cycling . . . 64
4.4 Tomographic Inspection . . . 69
4.5 Summary and Discussion . . . 72

5 Performance Characteristics . . . 73
5.1 Measurement Setup . . . 73
5.1.1 Signal Processing . . . 74
5.1.2 Phase Angle Reconstruction . . . 78
5.2 3D Ultrasound Performance . . . 83
5.3 Functional Ultrasound Characteristics . . . 84
5.4 Summary and Discussion . . . 89

6 Transducer Models for Analysis and Optimization . . . 93
6.1 Equivalent Circuit Model . . . 93
6.1.1 2D KLM Model . . . 95
6.1.2 Model Fit . . . 98
6.1.3 Estimation of Directivity . . . 102
6.2 Finite Element Analysis . . . 104
6.2.1 Initial FE Model . . . 104
6.2.2 Modeling of Losses in the Passive Materials . . . 108
6.2.3 FE Model Fit . . . 111
6.3 Summary and Discussion . . . 114

7 Design Analysis and Optimization . . . 117
7.1 Lower Frequency Limit . . . 117
7.2 Opening Angle . . . 120

7.3 Sensitivity Fluctuations . . . 124
7.4 Redesign and Discussion . . . 127

8 Alternative Transducer Technologies . . . 131
8.1 Overview of Explored Technologies . . . 131
8.2 Single-Crystal Test Transducer . . . 132
8.3 PMUT Test Transducer . . . 137
8.3.1 Manufacturing of Prototypes . . . 137
8.3.2 Characterization and Evaluation . . . 140
8.4 Polymer-based CMUTs . . . 145
8.5 Summary and Discussion . . . 147

9 Conclusion . . . 149

A Appendix . . . 153
A.1 Calculation Scheme of Analytical Model . . . 153
A.2 Tables with Material Parameters . . . 157
A.3 Student Supervision . . . 162

Acronyms and Symbols . . . 163

List of Figures . . . 167

List of Tables . . . 171

List of Publications . . . 173
Journal Articles . . . 173
Conference Contributions . . . 173

Bibliography . . . 175

1 Introduction and Motivation

Breast cancer is the most commonly diagnosed cancer type and the main cause of cancer-related death in women worldwide [8]. According to current estimates, one in eleven women in the European Union develops breast cancer before the age of 74 [9]. After diagnosis, the survival rate varies by country and region. In the EU, the average five-year survival rate was estimated 84% [8]. If secondary cancers (metastases) are found, the probability of survival decreases significantly. The occurrence of metastases correlates with the size of the primary cancer, making early diagnosis essential [10].

Since breast cancer shows almost no symptoms in early stages, regular screening is offered in many countries. X-ray mammography is the current imaging standard, with a high detection rate of cancerous tissue. However, mammography requires ionizing radiation and exhibits limited sensitivity for denser breasts [11]. Another screening method is magnetic resonance imaging (MRI). It exhibits very high sensitivities for detection [12], but can be a financial burden and requires the use of contrast agents. The latter may cause a variety of secondary effects such as allergic reactions [13] and kidney damages [14].

Ultrasound imaging or ultrasonography is a well-suited complementary method for breast imaging. Ultrasound is more sensitive than mammography in detecting cancer, especially when imaging dense breasts [15]. Additional benefits of using ultrasound are the essentially harmless nature of acoustic waves and lower costs. However, the use of manual ultrasound probes is operator-dependent and the resulting images can be challenging to interpret. Another imaging approach is ultrasound computed tomography (USCT), offering several benefits compared to manual probes. Subject of this work are electromechanical converters that

generate and receive ultrasound (henceforth referred to as transducers) for a full 3D USCT system.

1.1 3D Ultrasound Computed Tomography

The general idea of USCT for breast imaging is to surround the breast by many ultrasound transducers in a fixed setup. This allows for cross sectional imaging without the necessity of manual deformation. Surrounding the breast enables simultaneous scanning of tissue reflectivity, speed of sound and attenuation. The possibility of combining these three modalities makes USCT a highly specific and operator-independent alternative to the aforementioned imaging approaches [16]. In contrast to manual probes, the transducers emit unfocused ultrasound waves. Focusing is achieved by the applied image reconstruction algorithms.

Early work on USCT dates back to the 1970s [17]. Though until recently, clinical applications were limited due to challenges in data readout, image processing, and the required computational power. Today, several USCT setups are under investigation. Most rely on encircling the breast with a 2D ring of transducers (see [18–20]). Volumetric structures are obtained by moving this ring up and down and combining the respective slices.

A full 3D USCT approach is investigated at the Karlsruhe Institute of Technology (KIT). Here, the breast is completely surrounded by a semi-ellipsoidal or hemispherical measurement vessel. Figure 1.1 gives an overview of the third generation 3D USCT device at KIT (3D USCT III). The patient lies prone on top, while one breast is immersed in the water filled measurement vessel during the scan. The vessel holds space for 128 circular transducer array systems (TAS III), with 18 transducers integrated in each array. This sums up to in total 2304 individually controllable ultrasound transducers. The entirety of all transducers results in an unfocused 3D ultrasound aperture [21].

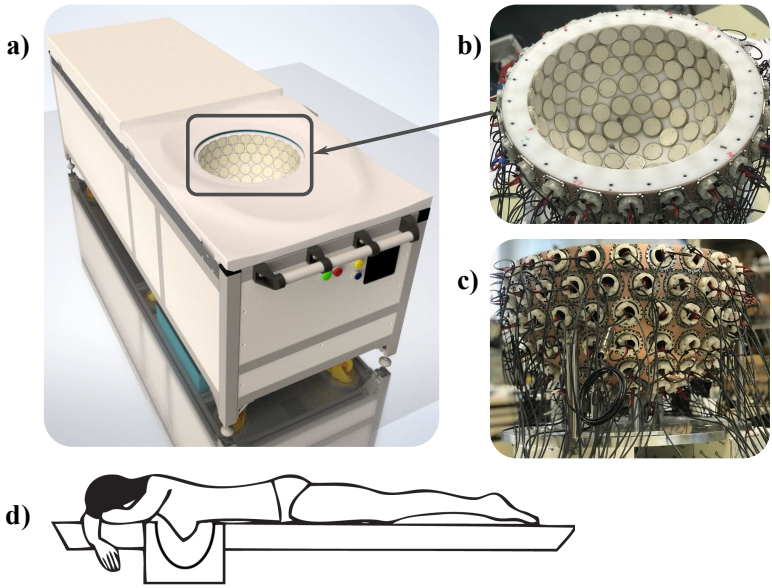

Figure 1.1: Third generation 3D USCT device at KIT: Rendered image of the imaging device (a), with magnified view of the measurement vessel holding 128 TAS III (b). Side view of the measurement vessel showing the cabling of the front-end electronics (c). Schematic depiction of patient position during the scan (d).

The measurement principle is as follows: One transducer emits an unfocused wave, while all other record the arriving sound pressure signals over time (A-scans). Depending on the time the emitted wave travels to the receiver, a separation in transmission and reflection signals is possible. Earlier signals correspond to direct transmissions, while later signals originate from reflections. This concept is emphasized in Fig. 1.2 with an example of a simple point scatterer (red sphere). From the received amplitude and delay, tomographic images of the breast can be reconstructed. Permutation of all available transducer leads to millions of A-scans to be used for subsequent image reconstruction [22].

Extensive amplification is required to obtain processible signals. Therefore, each TAS III is equipped with specifically designed front-end electronics for signal conditioning (see Fig. 1.1c) [23, 24]. The large number of generated A-scans

requires high-speed data readout and processing. FPGA-based data acquisition hardware used in particle physics experiments (e.g. MTCA.4 standard) provides a suitable and configurable platform [25].

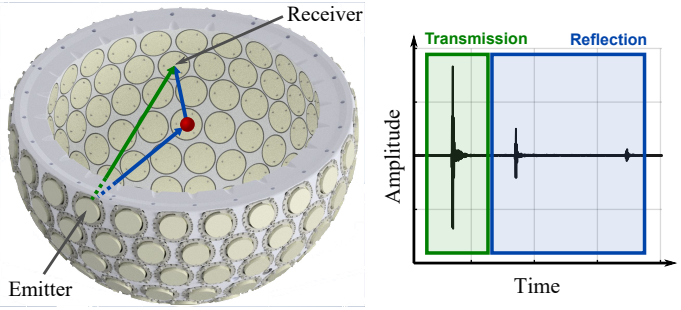

Figure 1.2: Simplified measurement principle of the 3D USCT imaging approach. An unfocused ultrasound pulse generated by the emitter travels either directly to the receiver or interacts with structures, in this example with a single point scatterer (left). Depending on the measured time of the received signals, a separation between direct transmission and later reflections is possible (right).

Distinct algorithms for transmission and reflection are applied to reconstruct images from the data. Transmission images, enabling the estimation of the tissue's speed of sound and attenuation, are typically based on iterative algorithms. The different acoustic properties of cancerous and healthy tissue are the basis of the images [26]. The achievable resolution depends on the assumptions made to model the wave propagation in the breast. These approaches range from straight rays, which neglects diffraction and scattering, to full wave inversion techniques. The more complex the assumptions, the higher the computational demands but the better the image quality [27, 28].

Reflectivity images are reconstructed using the synthetic aperture focusing technique (SAFT). The basic idea of SAFT is to sum many unfocused images generated from different geometric position to achieve focusing. The characteristics of the reflections correspond to changes in the acoustic impedance within the breast. This allows for differentiation between different tissue types, such as cancer or fat. For the 3D USCT III device, the hemispherical aperture enables the direct

reconstruction of volumetric structures with SAFT. The large amount of generated volumina (several million per scan) results in high computational demands, with reconstruction times up to several days if processed sequentially using standard CPUs. GPU based parallelization is applied to shorten the process down to a few hours [29, 30].

In contrast to conventional ultrasound, no realtime images are displayed during the scan. On one hand, this is not feasible due to the high amount of data and the complexity of image reconstruction. On the other hand, it is not necessary since volumetric data is stored for subsequent analysis. The limited number of individual transducers leads to a sparse imaging approach. This means that the Nyquist theorem to sample the breast volume with sufficiently high resolution can not be fulfilled. As a consequence, imaging artifacts are unavoidable. Non-regular distribution of the transducers in the measurement vessel reduces the impact of these artifacts [31].

1.2 Context and Aim of this Thesis

Extensive clinical tests are required to assess the sensitivity and specificity of new medical imaging devices. For this purpose, two 3D USCT III systems are currently under construction. The utilized ultrasound transducers are key components of the imaging concept since their properties are directly related to the achievable image contrast and resolution.

Requirements from image reconstruction as well as the integration in a hemispherical aperture result in design rules fundamentally different from conventional ultrasound transducer arrays. Therefore, commercially available arrays cannot be used or repurposed for 3D USCT.

Each 3D USCT III device holds space for 128 transducer arrays. Manufacturing this amount of arrays requires reliable and reproducible processes. Automation and quality control routines are suitable measures to meet these challenges.

Reliability has to be another key aspect of the design. Standardized tests defined in international norms are a viable source to estimate the limits of operation and long-term performance. Since extensive testing with patients will be conducted, the arrays have to comply with high safety standards to prevent harm to patients and operators.

After producing functional arrays, the ultrasound characteristics have to be characterized and evaluated with respect to the requirements. Strengths, weaknesses and limitations of the utilized technologies can then be assessed, and possible improvements identified. Analytical and numerical modeling techniques are essential tools in this regard.

Based on the aforementioned characteristics and requirements, the central aim of this thesis is defined as follows:

The central aim of this thesis is the realization of ultrasound transducer arrays to enable clinical tests with the 3D USCT III imaging technology.

In order to achieve the central aim, the following sub-aims are defined:

- Investigation and identification of key transducer requirements for the 3D USCT imaging technology.
- Development of a new transducer array design which complies with the identified requirements.
- Development of a manufacturing process which enables the production of several hundred arrays with high yield and low variability.
- Design of the manufacturing process in terms of scalability for future industrialization of the 3D USCT technology.
- Characterization of the ultrasound performance and derivation of statistical parameters for comparison and evaluation.
- Identification of strengths, weaknesses and limitations of the transducer array design.

If proven safe and effective in the following clinical study, 3D USCT will greatly aid in early detection of breast cancer to lower the mortality rate of affected females. Since the transducer arrays are among the most critical and technologically challenging components of this device, they play a fundamental role in achieving clinical feasibility.

2 Ultrasound Transducer Fundamentals

This chapter provides an introduction to piezoelectric transducers for medical ultrasound applications. Fundamental concepts of piezoelectricity and transducer design are introduced for later reference. Furthermore, a brief overview of currently investigated USCT systems is provided to highlight the unique features of the 3D USCT concept.

2.1 Piezoelectric Properties

Piezoelectricity arises in asymmetric crystalline structures. If an electric field is applied to such a material, mechanical deformation can be observed. Inversely, when a mechanical force is applied, an electrical field is measurable [32]. The deformation caused by an electric field is called the reverse piezoelectric effect. A measured voltage caused by a mechanical force is called the direct piezoelectric effect. The piezoelectric effect and its origin are described in great detail in literature (see [32–34]). This work focuses primarily on piezoelectric properties and an approach to derive a set of piezoelectric constants from sparse literature data.

Since piezoelectricity is based on interactions at the atomic level, a complex theory is required for analytical modeling. A more practical approach is a phenomenological description of the effects from a macroscopic point of view. There it was found that an approximately linear relation between an applied electric field E and the resulting strain S can be observed within certain limits [35]. In addition,

piezoelectric materials exhibit elastic properties and thus a linear dependence between an applied stress T and the resulting S. Due to the electromechanical (EM) coupling of the material, those two effects add up to form the resulting total strain.

Since piezoelectric materials possess highly anisotropic behavior, a set of equations is required to describe the relations in all spatial dimensions. A common definition in the field of ultrasound transducers is given in Eq. 2.1 and Eq. 2.2 (matrix equations in strain-charge form), where s^E is the mechanical compliance (inverse of mechanical stiffness), d the piezoelectric charge constant (^{t} for transposed), ϵ^T the absolute permittivity and D the electric displacement field [36, ch. 2].

$$S = s^E \cdot T + d^t \cdot E \tag{2.1}$$

$$D = d \cdot T + \epsilon^T \cdot E \tag{2.2}$$

With T and S second rank tensors in three spatial directions, the constitutive matrix equations exhibit in total 63 constants. These can be reduced to 10 when the hexagonal crystallographic symmetries of poled ferroelectric ceramics are considered [37]. The remaining independent constants for the stated constitutive matrix equations are given in Eqs. 2.3-2.5. These constants describe how stress, strain, electric field and displacement field in the piezoelectric material interact with each other, dependent on the geometric directions.

The two-digit subscript indicates the directivity of the respective constant. The first digit relates to the direction of an action and the second to the respective reaction, e.g. the mechanical stiffness in lateral direction under axial compression. The superscript defines the mechanical and electrical boundary conditions under which the parameters are valid. Superscript ^{E} states that the property was obtained at a constant electric field, achieved e.g. by shorting the electrodes. Superscript ^{T}

relates to constant mechanical stress in an open, non-clamped operation of the piezoelectric material.

$$s^E = \begin{bmatrix} s_{11}^E & s_{12}^E & s_{13}^E & 0 & 0 & 0 \\ s_{12}^E & s_{11}^E & s_{13}^E & 0 & 0 & 0 \\ s_{13}^E & s_{13}^E & s_{33}^E & 0 & 0 & 0 \\ 0 & 0 & 0 & s_{55}^E & 0 & 0 \\ 0 & 0 & 0 & 0 & s_{55}^E & 0 \\ 0 & 0 & 0 & 0 & 0 & 2(s_{11}^E - s_{12}^E) \end{bmatrix} \tag{2.3}$$

$$d = \begin{bmatrix} 0 & 0 & 0 & 0 & d_{15} & 0 \\ 0 & 0 & 0 & d_{15} & 0 & 0 \\ d_{31} & d_{31} & d_{33} & 0 & 0 & 0 \end{bmatrix} \tag{2.4}$$

$$\epsilon^T = \begin{bmatrix} \epsilon_{11}^T & 0 & 0 \\ 0 & \epsilon_{11}^T & 0 \\ 0 & 0 & \epsilon_{33}^T \end{bmatrix} \tag{2.5}$$

The aforementioned 10 constants allow for a comprehensive description of the behavior of many piezoelectric materials. Among those is lead zirconate titanate (PZT), which is often used in ultrasound transducers. Usually, not all constants are available in material datasheets or other literature sources. In order to obtain all required constants, extensive measurements with specially prepared material samples and geometries have to be conducted [38, 39]. Hence, a conversion of the constants from given data is more practical but requires approximations and assumptions.

In order to obtain a full set of constants, the method proposed in [40] was used in this work. It states a simple procedure based on the definitions of the shear and planar EM coupling k_{15} and k_p. This enables the calculation of two mechanical

constants according to Eq. 2.6 and Eq. 2.7, which are often missing in material datasheets.

$$s_{55}^{E} = \frac{d_{15}^{2}}{\epsilon_{11}^{T} \cdot k_{15}^{2}} \tag{2.6}$$

$$s_{12}^{E} = -s_{11}^{E} + 2 \cdot \frac{d_{31}^{2}}{\epsilon_{33}^{T} \cdot k_{p}^{2}} \tag{2.7}$$

The shear compliance s_{13}^{E} can be determined according to Eq. 2.8, where ν_{13}^{E} is the Poisson's ratio of the material at a constant electric field. With these formulas and assumptions, the required 10 constants can be obtained and the anisotropic elastic behavior of PZT materials modeled.

$$s_{13}^{E} = -\nu_{13}^{E} \cdot s_{11}^{E} \tag{2.8}$$

Equation 2.1 and 2.2 are merely one possible form of stating the constitutive piezoelectric interactions. Other forms can be achieved by converting the piezoelectric constants to obtain different relationships. For instance, when multiplying d with the inverse of ϵ^{T}, one obtains the piezoelectric voltage constant g and a dependency between S and D [41].

Two additional constants are introduced since they are needed in later chapters of this thesis. These are the permittivity at constant stress ϵ^{S}, and the stiffness at constant dielectric displacement c^{D} (open circuit conditions). By rearranging and substituting several relations between different piezoelectric constants, the parameter matrices for ϵ^{S} and c^{D} can be calculated according to Eq. 2.9 and Eq. 2.10, respectively [41, 42]. This enables a direct conversion of constants by using only those found in the constitutive equations in strain-charge form.

$$\epsilon^{S} = \epsilon^{T} - d \cdot \left[d \cdot (s^{E})^{-1} \right]^{t} \tag{2.9}$$

$$c^D = (s^E - \left[(\epsilon^T)^{-1} \cdot d\right]^t \cdot d)^{-1} \tag{2.10}$$

It is important to note that the presented conversions are only valid under certain limited circumstances. The mechanical and electrical boundary conditions as well as the material geometry play a key role in obtaining accurate results [42]. Hence, a design approach using different modeling techniques with a careful choice of constants is important to obtain reasonable results.

2.2 Piezoelectric Transducers

Much of the theoretical foundation of ultrasound transducers for medical imaging was formulated as early as the 1970s and 1980s. These range from fundamental research [43, 44], to detailed design guidelines [45, 46]. This section introduces some basic concepts to understand the nomenclature and design ideas for transducers used in USCT. More detailed information can be found in the cited literature.

A conventional piezoelectric ultrasound transducer is shown in Fig. 2.1a. For the EM conversion, a piezoelectric ceramic material (piezoceramic), in many cases PZT, is utilized. Typically, either the planar or thickness vibration modes are used to generate and receive ultrasound, shown schematically in Fig. 2.1b. The material and its dimensions have to be carefully selected to obtain high performance in the desired vibration mode and frequency range [42, 47].

In most cases, a transducer is designed to operate at a single mode of vibration since the resulting characteristics are more consistent and predictable. However, a clear separation of the individual modes is often difficult to achieve, especially when a dominant mode of vibration occurs below the frequency range of interest. Harmonics of this vibration mode may then cause interferences. A common technique to counteract this effect is a dice-and-fill approach. There, a rectangular grid is cut into the piezoceramic and the kerfs are filled with polymer to form a

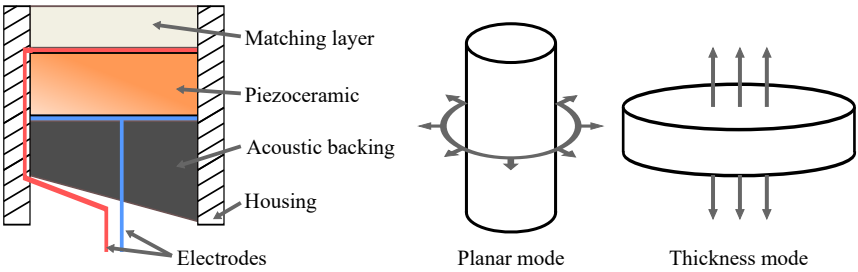

(a) Schematic depiction of a single ultrasound transducer.

(b) Planar (d_{31}) and thickness (d_{33}) vibration modes.

Figure 2.1: Typical structure of a ultrasound transducer (a) and common vibration modes (b).

piezocomposite. The resulting pillar structure is then foreseen with a common electrode, resulting in a superposition of the thickness mode of the pillars, while the planar mode resonance is shifted away from the desired frequency spectrum [48]. Replacing a portion of the ceramic with a polymer is also beneficial with respect to the overall performance since it decreases the acoustic impedance and mechanical quality factor. This increases the effective output pressure and bandwidth [49]. Figure 2.2 shows a photography of an exemplary composite.

One end of the piezoceramic is usually attached to a matching layer. This is necessary to match the acoustic impedance to a coupling medium such as ultrasound gel or water (see Section 2.2.1). On the opposite end, an acoustic backing material is applied (see Section 2.2.2). This increases the transducer's functional bandwidth

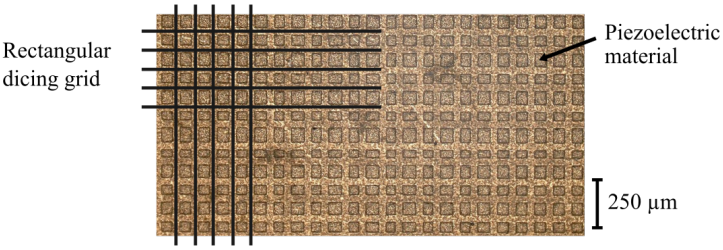

Figure 2.2: Photography of exemplary piezocomposite material produced with the dice-and-fill approach.

and reduces reflections. Both, matching and backing layers have to comply with specific requirements, explained in more detail in the respective sections below.

For a single transducer, the acoustic field is directly defined by the transducer's geometry and the applied frequencies. In clinical practice, the information obtained with a single element is not sufficient for imaging. Hence, arrays are utilized which enable focusing and steering of the acoustic field for real-time imaging [50].

2.2.1 Acoustic Matching

Matching layers are used to connect the piezoceramic with the imaging medium to improve energy transmission. For transducers used in medical imaging, the matching layer has to comply with the following requirements:

- Intermediate acoustic impedance Z_M between the piezoceramic (e.g. PZT) and imaging medium (e.g. water or tissue) to compensate for the large mismatch. This is necessary to improve the energy transmission and ensure fast ringdown of the emitted pulse [51].
- High isolation resistance to ensure protection of the patient and operator from the electrical excitation pulses [52].
- Low water absorption to ensure high isolation and time-invariant performance in the use case.
- High resistance against chemicals and disinfectants to survive clinical routines.
- Good processability to enable simple packaging (e.g. machining or molding processes).

The theory to obtain ideal impedance matching for single transducers was developed in the late 1970s, where the optimum acoustic impedances and thicknesses of single and multiple matching layers were derived using transmission line theory [45]. The use of a single $\lambda/4$ matching layer has the advantage of lower

fabrication complexity, but reduces the achievable energy conversion. In order to maximize the conversion factor, the single matching layer should exhibit an acoustic impedance close to the geometric mean of the respective materials. The ideal value can be calculated with Eq. 2.11 [53], where Z_0 is the characteristic acoustic impedance of the piezoceramic and Z_F the acoustic impedance of the front medium.

$$Z_M = \sqrt{Z_F \cdot Z_0} \tag{2.11}$$

For a thickness-mode piezoceramic transducer, Z_0 can be estimated according to Eq. 2.13 by applying the Newton-Laplace equation given in Eq. 2.12. There, ρ is the density, v_t the material's longitudinal speed of sound and c_{33}^D the stiffness in thickness direction at constant dielectric displacement.

$$v_t = \sqrt{\frac{c_{33}^D}{\rho}} \tag{2.12}$$

$$Z_0 = \rho \cdot v_t \approx \sqrt{\rho \cdot c_{33}^D} \tag{2.13}$$

Most piezoceramics exhibit a Z_0 in the range of 20-30 MRayl. MRayl is an auxiliary unit for the acoustic impedance. In SI units, it is equivalent to $\mathrm{MPa} \cdot \mathrm{s/m}$. Matching the acoustic impedance of piezoceramics to water (1.5 MRayl) results in 5-8 MRayl for Z_{ML}. Not only the desired value for Z_{ML} but also the other aforementioned requirements limit the range of usable materials. Polymers would comply well with most of them, but exhibit too low acoustic impedances [51]. Hence, composite materials or multiple layers are commonly used in bulk piezo-based ultrasound transducers.

2.2.2 Acoustic Backing

For medical ultrasound applications, a transducer should be capable of generating very short pulses to enable high temporal separability of individual signals. This is achieved with transducers whose vibration behavior is strongly damped. For this it is important to cover the rear side of the piezoceramic with an acoustic backing material. This backing material has to comply with the following requirements:

- Specific acoustic impedance to optimize the bandwidth and the sensitivity for the application. For instance, a backing impedance of $Z_B = Z_0$ results in a very high bandwidth, but shows low output pressures [54]. A low Z_B would result in a high peak pressure, but within a very limited frequency range.
- High damping properties to attenuate backside reflections. The overall attenuation depends on the thickness of the material and the frequencies used. As a rule of thumb, an attenuation of the signal amplitude by 40–100 dB is desired [55].
- Good processability of the material to enable machining or molding processes.

These requirements result in the design of specialized materials and composites. One common approach is to utilize electrically conductive solder (e.g. Von Roll E-Solder 3022 [56]) as acoustic backing material. While this simplifies the assembly and the production process, the achievable acoustic impedance is limited (in case of the stated solder to 5.9 MRayl). Another approach is to mix high-density materials with polymers to form viscous pastes that can be dispensed or molded [54, 57]. Depending on the materials used, impedances up to 20 MRayl are achievable. The materials and mixing ratios have to be optimized for each application to identify the best trade-off between sensitivity, functional bandwidth and attenuation properties [55].

2.3 Transducer Characteristics

Resolution and contrast are the image characteristics which need to be optimized for most imaging systems. In case of ultrasonography, both are directly linked to transducer characteristics. To start with, the fundamental relationship between resolution and ultrasound frequency needs to be stated. This means that structures with dimensions smaller than half the wavelength cannot be resolved. For example, to theoretically achieve an axial resolution x_a of 0.5 mm in water, the sound wave has to exhibit a frequency of at least 1.5 MHz, as shown with Eq. 2.14.

$$f_{min} = \frac{v}{\lambda} = \frac{v}{2x_a} = \frac{1500\ \mathrm{m/s}}{2 \cdot 0.5\ \mathrm{mm}} = 1.5\ \mathrm{MHz} \tag{2.14}$$

The use of high frequencies has practical limits, since sound attenuation increases with rising frequency, resulting in lower signal amplitudes at the receivers. This is of special importance for the 3D USCT device, since the sound wave has to travel long distances in water and soft tissue.

The image contrast of the USCT system depends mostly on the number of the transducers and the achievable signal-to-noise ratio (SNR) [58]. The number of transducers is limited by engineering challenges in integration and data processing. The SNR depends on the signal processing, transducer technology, transducer geometry and assembly.

Another important imaging property is the directivity of the emitted sound field, limiting the scannable size of the breast. Small transducers distribute the sound in larger areas and therefore enable a more homogeneous illumination of larger breasts. However, the small size limits the emitted sound pressure and consequently, the achievable SNR.

As usual in science and engineering, many trade-offs are required to comply with given requirements. Carefully balancing the drawbacks while optimizing the performance is difficult without quantifiable acceptance criteria. Three out of the

many characteristics of ultrasound transducers are presented in more detail below since they are central to USCT.

Ultrasound bandwidth

The ultrasound bandwidth bw_{us} represents the frequency range in which the transducer is able to emit and receive sound efficiently. This range is defined by a specified decrease in emitted sound pressure around the center frequency f_c. In this work, a bandwidth definition based on a drop of 10 dB from the peak amplitude is used. It is derived from the measured frequency response magnitude as illustrated in Fig. 2.3a. With this bandwidth definition, the lower and upper frequency limits f_l and f_u can be defined. In other engineering fields such as filter design, the bandwidth is usually defined by a 3 dB drop reflecting the frequencies at which half of the spectral signal power is reached. For the 3D USCT system, the definitions are chosen more generously since the general imaging approach and the applied signal processing methods are capable of compensating for larger amplitude drops. In literature, the bandwidth is often defined as a fraction of the center frequency according to Eq. 2.15 for better comparison.

$$bw_{us} = \frac{f_u - f_l}{f_c} \tag{2.15}$$

Opening angle

The opening angle Φ_t represents the width of the main lobe (bold part of curve in Fig. 2.3b) obtained from the directivity curve of a transducer. It is defined by the angles Φ_l and Φ_u, marking the 10 dB decrease with respect to the center angle Φ_c. An example is illustrated in Fig. 2.3b. Since the opening angle depends on the frequency, different definitions can be found in literature. In this work, a broadband definition of directivity was chosen, explained in more detail in Section 5.3.

Center sensitivity

The center sensitivity S_c is defined as the maximum of the measured sound pressure at a single frequency and angle. Typically it occurs in vicinity of f_c and Φ_c. Since S_c depends on the distance between emitter and receiver, direct comparison

is only possible if the measurement conditions match. By normalization, a more general expression of S_c can be obtained.

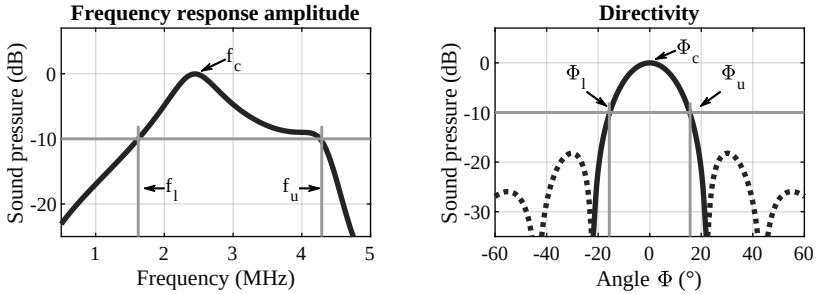

(a) Exemplary frequency response magnitude of a transducer with definitions of characteristic frequencies.

(b) Exemplary directivity with the definition of the opening angle (Φ_u-Φ_l). The bold part of the curve represents the main lobe, the dotted parts the side lobes.

Figure 2.3: Functional ultrasound characteristics of a transducer derived from the frequency response amplitude (a) and directivity (b).

Other important transducer characteristics are the electrical input impedance, crosstalk between adjacent transducers and unwanted echoes. The later two may cause imaging artifacts which are difficult to suppress or remove in image reconstruction [59]. The design goals depend on the application, the desired resolution and the configuration of the ultrasonography device. Therefore, extensive modeling and testing is required to achieve the targeted performance of a transducer.

2.4 State of the Art of Transducers for USCT

Various USCT approaches for breast imaging are being investigated worldwide [60–68]. Most of them combine transmission and reflection imaging. All emit unfocused or plane ultrasound waves with center frequencies varying from 0.9 MHz to 8 MHz. The key difference between the systems is the ultrasound aperture. In general, it can be divided into three groups: 2D linear or ring apertures, 2.5 segments or 3D vessels. An overview of these three groups is shown in Fig. 2.4.

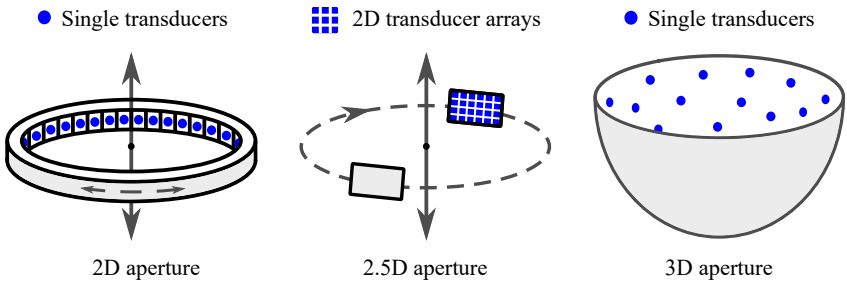

Figure 2.4: Three groups of USCT imaging approaches, ranging from movable 2D apertures with a single row of transducers, 2.5D apertures with movable multi-row arrays to a full 3D setup (left to right).

The differences in the aperture results in a variety of system designs and image reconstruction techniques. Table 2.1 gives a summary of the systems under investigation, with focus on the utilized transducers.

Most systems use 2D ring apertures with a single row of equally spaced transducers. Volumes are sampled by moving this ring up and down. Some systems also allow for rotation to improve the contrast. A slightly different approach is pursued with a system called QT scanner 2000 [67]. This system holds receiver segments with eight rows and 256 columns in transmission mode. Hence, direct volumetric information of the breast can be obtained, leading to the definition of a 2.5D system. To this day, the system at KIT is the only approach based on a full 3D aperture. Here, the breast is fully surrounded by distributed transducers to directly obtain volumetric information.

For most systems, the transducer basis material is PZT. Only the SoftVue system, and the design from the North China University differ in this regard. The first utilizes single-crystal piezoelectrics, while for the second, piezoelectric micromachined ultrasound transducers (PMUTs) are the basis of generating and receiving ultrasound. The achievable gains and possible challenges of these two transducer technologies are discussed in Chapter 8.

Reflection and transmission imaging is usually conducted with the same set of transducers. The QT scanner 2000 design follows a different approach by using separate arrays for the distinct modalities. There, transmission imaging is achieved with the aforementioned planar arrays at a center frequency of 0.9 MHz. Reflections are measured with a circular transducer arrangement consisting of three planar arrays. The center frequency of the reflection-mode transducers is four times higher in order to achieve high resolution images.

Table 2.1: Overview of USCT systems/research groups focusing on the transducer design. Unavailable data is indicated with n/a.

System	Aperture	Techn.	f_c	bw_{us}	Num.	Peculiarities
3D USCT II [60]	3D Semi-ellipsoid	PZT	2.5 MHz	60% (-6 dB)	2041	Full 3D aperture
ANAÏS [61]	2D Semi-circle	PZT	3 MHz	75% (-6 dB)	1024	190° rotatable arc
BUTIS [62]	2D Ring	n/a	2.25 MHz	n/a	1024	
Hitachi Ltd. [19]	2D Ring	n/a	3 MHz	n/a	1024	
HUTT [63]	2D Planar arrays	PZT	8 MHz	50% (n/a)	2x64	Rotatable planar arrays
North China University [64, 65]	2D Planar arrays	PMUTs	3.5 MHz	86.7% (-6 dB)	4x128	Vertical arrangement of a rrays
SoftVue [66]	2D Ring	Single-crystals	2.75 MHz	100% (n/a)	2048	FDA approved*
QT scanner 2000 [67]	2.5D Planar arrays and circular segments	PZT	0.9 MHz 3.6 MHz	100% 70% (-6 dB)	8x256 3x192	Separate arrays for transmission and reflection
Warsaw University [20, 68]	2D Ring	PZT	1.7 MHz	n/a	1024	Focus on transmission

*Since November 2021

Successful clinical studies for several systems were reported (see [69–71]). However, only the SoftVue system is already used in clinical practice, since it got approval from the U.S. Food and Drug Administration (FDA) in November 2021. The conducted multi-center study reported a sensitivity improvement of 20% and a specificity improvement by 8% compared to mammography screening [72]. This gives first prove of the effectiveness of USCT in clinical routine.

3 Transducer Array Design and Production

This chapter presents the design of the TAS III and a semi-automated production process to manufacture the amount of arrays required for two 3D USCT III devices. A brief design history of arrays utilized in previous USCT generations at KIT is given to emphasize the evolution of the technology. This leads to the derivation of requirements acting as guidelines for the new design. The TAS III design combines technologies and processes from previous generations, with substantial improvements with respect to automation and reproducibility. Challenges and countermeasures are discussed, with a step-by-step description of the applied processes.

This work comprises the front end of the transducer arrays used for the physical conversion from electric to acoustic energy. The electronics required for signal amplification and conditioning are discussed in detail in [23] and [24].

3.1 Design History of TAS

The USCT research at KIT started with a manual prototype in the year 2000. Two arrays with 16 elements each were mounted on holders which were connected to a movable ring. This allowed for 360° degree placements of each array as shown in Fig. 3.1a. The transducers contained diced PZT ceramic plates with a center frequency of 2.5 MHz, embedded into a stainless steel housing [73]. These first prototypes enabled the initial evaluation of the USCT technology and the corresponding image reconstruction algorithms.

In 2005, a more advanced 3D prototype system was built by integrating 48 first-generation TAS (TAS I) into a cylindrical aperture, shown in Fig. 3.1b. Each TAS I held 40 elements, leading to 1920 transducers in total. Similar to the previous design, the transducers were based on diced PZT ceramic plates, which exhibited a center frequency of 3.25 MHz. Electrical connection was established via wire bonds to a substrate. This substrate hosted front-end amplifiers and signal conditioning circuits. A single uniform matching layer was glued to the front of the PZT plates and the structure was integrated into a rectangular housing. Finally, the housing was filled with a polyurethane (PU) backing [74].

(a) First USCT prototype at KIT from the year 2000.

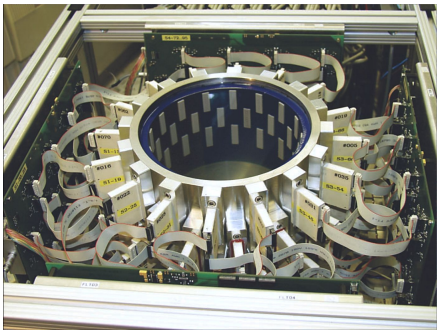

(b) 3D USCT I prototype developed in 2003.

Figure 3.1: First USCT prototype with manual placement of transducer arrays (a), which later evolved to the 3D USCT I system (b). The pictures are taken from [75].

In order to achieve the best possible image quality for SAFT reconstructions, the aperture of the next generation system needed significant adjustments. A study was conducted to optimize resolution, image contrast and object illumination within a breast-shaped region of interest (ROI). As a result, a semi-ellipsoidal aperture with a height of 21.5 cm and an external diameter of 34 cm was produced. The aperture consisted of 157 cylindrical arrays, with 13 single elements integrated in each array and a center frequency of 2.5 MHz. Out of these 13 elements, nine were used as receivers and four as emitters [60].

The transducer technology was once again based on diced PZT plates, glued onto a matching layer substrate and electrically connected with wire bonds, shown in Fig. 3.2a. Amplifiers for the receiver and emitter were connected close to the PZT using a foldable printed circuit board (PCB), integrated into a stainless steel cylindrical housing. This housing was filled in the last step with a PU backing material [22]. In Fig. 3.2b, a set of finalized second-generation TAS (TAS II) is shown.

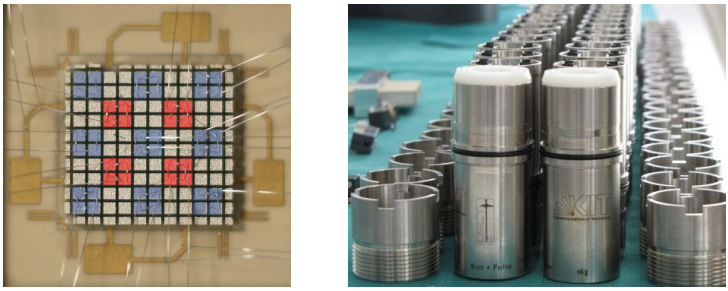

(a) Diced and bonded PZT plate. **(b)** Finalized TAS II.

Figure 3.2: TAS II based on diced PZT plates (a), integrated into a cylindrical housing (b). The pictures are taken from [60] and [76].

A pilot study conducted with the 3D USCT II system provided proof of concept of the imaging approach using a semi-ellipsoidal aperture [71]. Based on the results of this study, it was possible to identify the improvements required to close the gap to clinical implementation of the technology [21, 31]. On transducer level, these improvements were:

- A uniform random distribution of the transducers in the semi-ellipsoid to reduce artifacts and improve the image contrast.
- Increasing the ROI by enlarging the size of the measurement vessel and the opening angle Φ_t of the transducers.
- An increase in the functional bandwidth to enable the emission of short pulses.

- A reduction of the manufacturing costs and improvements in reproducibility and reliability.
- Adjustment of the transducer geometry to obtain an isotropic point spread function (PSF) in all three spatial dimensions.

Implementing the necessary improvements resulted in a profound redesign of the TAS II. In order to gain experiences in achieving the requirements, the dice and fill process of PZT plates used in previous designs was enhanced to form distributed octagons, as exemplified in Fig. 3.3a. With a diameter of 0.7 mm, these octagons exhibited a large Φ_t and closely approximated an isotropic acoustic field [76, 77]. Although the performance was promising, challenges in manufacturing and reproducibility led to developments in a different direction.

In 2015, a novel approach to produce thin cylindrical PZT fibers was presented by Fraunhofer IKTS [78]. With this technology, individual fibers can be placed freely and embedded in polymer. This allows for manufacturing of randomly spaced 1-3 piezocomposites, promising good compliance with 3D USCT requirements. A joint research project was initiated to develop single-fiber piezocomposite disks, subsequently called composite disks, to be integrated into the next generation TAS. First prototypes of the developed disks are shown in Fig. 3.3b. With these, characterization of the technology and design improvements were possible [79].

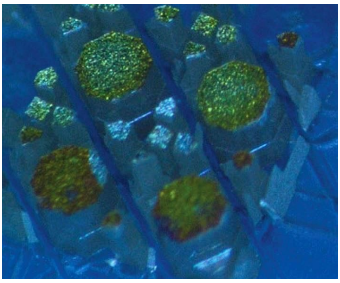

(a) Diced octagon transducers taken from [76].

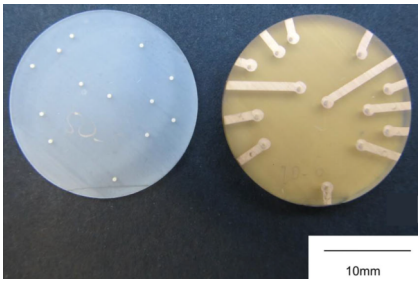

(b) Single-fiber composites before and after electrode sputtering [79].

Figure 3.3: Single-PZT-fiber transducer technologies to implement the improvements derived from the 3D USCT II pilot study.

In order to evaluate the single-fiber technology, a design was developed to replace the dice-and-fill transducers of the TAS II. In this intermediate TAS generation (TAS IIb), each array held 17 irregularly distributed single-fiber transducers. Electrodes were sputtered on both sides for electrical connection. With a thickness of 0.75 mm, the transducers exhibited a center frequency of 2.0 MHz. One of the described composite disks is shown in Fig. 3.4a. A single matching layer was glued to the top side and a PCB was connected to the bottom side to finalize the arrays, schematically shown in Fig. 3.4b. The manufacturing and testing of the TAS IIb generation was the first task within the context of this thesis. The findings obtained led to further improvements and refinements [1]. This resulted finally in the TAS III design, described in detail in the following section.

(a) Bottom view of TAS IIb composite disk.

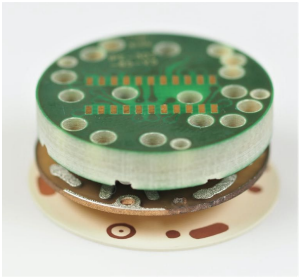

(b) TAS 2.5 transducer stack taken from [1].

Figure 3.4: TAS IIb design to replace the arrays used in 3D USCT II. A composite disk (a) is integrated between a PCB (b, top) and a matching layer (b, bottom) to form a transducer array.

3.2 Design Requirements

Relating the image quality of ultrasonography directly to single transducer characteristics is difficult, especially when it comes to quantification. This also applies for 3D USCT, since the overall design has to be considered for each characteristic.

Interesting in this respect is the work of Gelly et. al, where relations between transducer characteristics and their effect on the achievable image quality is presented graphically [80].

Nevertheless, to be able to efficiently design a transducer array, a specification with clearly defined characteristics and acceptance criteria is required. Table 3.1 summarizes key requirements of the TAS III, derived from imaging physics, system design and medical device regulations. The stated criteria evolved from the design history and can be regarded as goals rather than fixed thresholds. Still, they enable a straightforward design process, evaluation and comparison with future developments. For clarification it is important to state that the center frequency f_c and the desired frequency range from f_l to f_u originate from different requirements. This results in a shift of f_c towards f_l rather than being the arithmetic mean between the stated limits.

The fractional bandwidth derived from the frequency considerations is challenging to achieve. A typical bandwidth of piezoceramic transducers for medical imaging is in the range of 80-90%. This already requires optimized acoustic matching and backing, which comes at the expense of sensitivity [81]. Further increase is possible by optimizing the material or applying advanced transducer geometries, neither of which is easy to achieve [82]. Hence, the feasibility of lower frequencies and thus the easier use of advanced image reconstruction techniques must be balanced against the resolution for reflection imaging.

The acoustic field generated by a transducer should be isotropic, enabling an equal resolution in all spatial dimensions [60]. Furthermore, the sparse imaging approach of 3D USCT III requires a randomized transducer distribution to better suppress imaging artifacts [21].

Since the 3D USCT III device is intended for clinical use, complying with medical device regulations is essential. Harmonized standards, first and foremost ISO-60601 [52], specify the required tests and examinations the device has to pass to prove that it is harmless for patients and operators. Hence, not only functional aspects but also the performance in terms of electrical isolation, generation of heat and biocompatibility must be taken into account.

Table 3.1: Requirements and desired characteristics of the TAS III. The stated values are design goals for efficient development and later comparisons, motivated by the given rationals. Explanations on the functional properties are given in Section 2.3.

Characteristics	**Requirement**	**Rational**
Functional characteristics		
Lower frequency limit f_l	0.5 MHz	Wave equation based transmission tomography [83]
Upper frequency limit f_u	5 MHz	High axial and lateral resolution, improves pulse compression [75]
Center frequency f_c	2.5 MHz	Well suited for centering the frequency range [75]
Fractional bandwidth bw_{us}	180%	See Eq. 2.15
Opening angle Φ_t	60°	Based on simulations, see [76]
Sensitivity S_c	n/a*	To be used for future comparisons
Geometry		
Ultrasound beam	isotropic	Distortion-free imaging and uniform resolution in all dimensions [60]
Transducer arrangement	pseudo-random	Minimize artifacts of the sparse aperture and maximize the contrast [21]
General and manufacturing		
Safe and non-toxic		Comply with medical device regulation [52]
Automatable and scalable		Optimize manufacturing to produce larger quantities
Low cost		Enable accessibility to a large population

*No value defined; depends on the overall concept, data processing, number of transducers etc.

3.3 New Array Design

The TAS III design is an advancement from the TAS IIb design to address the design requirements and optimizations identified in the clinical pilot study. In

addition to the functional requirements, special emphasis was placed on automation of the manufacturing processes to shorten the production time and reduce variability. This resulted in the design shown in Fig. 3.5. The basic idea is to stack three disks on top of each other to form an ultrasound transducer array. This stack can then be integrated into a housing and connected to front-end electronics.

The core component of the new design is a composite disk, holding 18 piezoceramic transducers. The transducers are embedded in polymer to form a composite similar to the TAS IIb design, but adjusted in size and transducer positions. Each transducer is electrically connected by printed electrodes, while all share a common ground (GND). A single acoustic matching layer (matching disk) is connected on the front, and a PCB disk is attached to the back side using conductive and non-conductive adhesives. The acoustic backing is applied to the rear by molding backing material into drill holes provided in the PCB.

In the final state, the piezoceramic fibers are embedded in different materials on all sides to achieve the required ultrasound functionality. A schematic cross section of a finalized single transducer is illustrated in Fig. 3.6. Next to the cross section, a picture of the three disks before interconnection and a relation with the materials and layers is shown. The transducer electrodes, the GND and an integrated temperature sensor can be accessed by connector pads foreseen on the

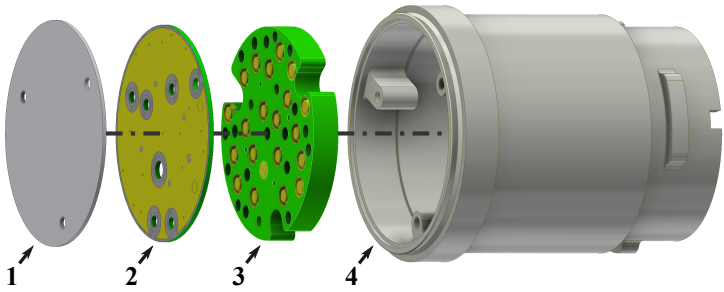

Figure 3.5: Explosion view of the TAS III design encompassing a matching disk (1), a composite disk (2) which holds the piezoceramic elements, a PCB disk (3) and a plastic housing (4).

top side of the PCB. Detailed explanations on each of the components utilized in this design is given in the following subsections.

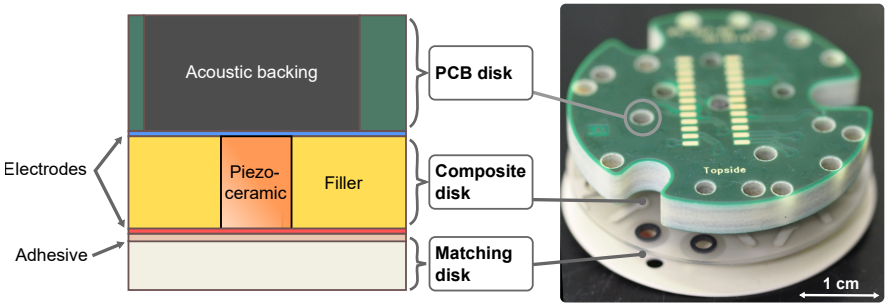

Figure 3.6: Schematic cross section of a single transducer related to a picture of the three components stacked on top of each other. The direction of the emitted ultrasound is towards the bottom.

3.3.1 Composite Disk

The composite disks were produced at Fraunhofer IKTS based on their proprietary 1-3 piezocomposite technology using single piezoelectric fibers [78]. The fibers were manufactured from commercially available PZT powder (Sonox P505, CeramTec, Plochingen, Germany) by means of a polysulfone spinning process. The obtained fibers were next inserted into a CNC machined mask, placed in a casting mold and embedded in epoxy adhesive (EpoTek 301-2, Epoxy Technology, Billerica, USA). This enables an arbitrary placement of single fibers with high design freedom of the array geometries [84].

For the TAS III design, 18 piezoceramic fibers with a diameter of 0.46 mm were integrated. The fibers are distributed over the whole disk to comply with the requirement of a pseudo-random transducer positioning. The fiber diameter was chosen based on simulations to ensure large opening angles of single transducers [79]. Each array features three hollow fibers for mounting pins (2 mm diameter), two for GND connection (2 mm diameter) and one for placing a SMD temperature

sensor (3 mm diameter). The raw mold was machined to an outer diameter of 35.5 mm and cut into disks with a thickness of 0.6 mm. These outer dimensions of the piezoceramic fiber were chosen to match the targeted center frequency. A raw composite disk is shown in 3.7a.

In order to electrically connect the piezoceramic fibers, electrodes were stencil printed on both sides. Fiducial markers in the form of four concentric dots were foreseen to detect the disk's center for automatic positioning. An additional cross allows for rotation correction. Redundant GND connections were provided to ensure reliable connection. In Fig. 3.7b and Fig. 3.7c, the front and back side of one composite disk is shown.

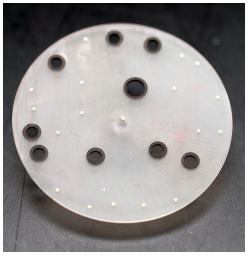

(a) Raw composite disk showing the integrated piezoceramic fibers (golden dots).

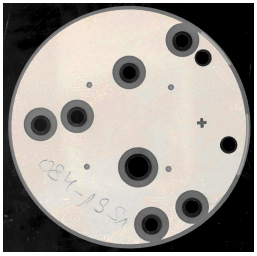

(b) Front view showing the uniformly printed GND electrode.

(c) Back view, showing the printed V_{in} electrodes and additional features.

Figure 3.7: Different views of the TAS III composite disk. Each disk holds 18 piezoceramic fibers and supplementary structures for the assembly. On both sides, fiducial markers (crosses and dots) for detection and alignment were foreseen.

3.3.2 PCB Disk

The PCB connects the transducers with the front-end electronics and holds space to apply acoustic backing material to the back side of the piezoceramic fibers. At the bottom side, the PCB has 20 circular pads to electrically connect the composite disk using conductive adhesive, shown in Fig. 3.8a. A concentric trench is milled around each pad to avoid electrical shorts caused by displaced adhesive. In addition to the pads, 21 drill holes are foreseen out of which 18 are

used for acoustic backing and three act as mounting aids. Each array holds space for a miniature temperature sensor (0402 SMD pad) to monitor the temperature.

In order to ensure high attenuation of the ultrasound emitted to the rear, a sufficiently thick acoustic backing layer is necessary. Therefore, the PCB exhibits a thickness of 4.3 mm which reaches the limits of the manufacturer (HLT Leiterplattentechnik, Beuren, Germany). The top side of the PCB disk holds the footprint for a 26-pin socket used to interface the front-end electronics (see Fig. 3.8b).

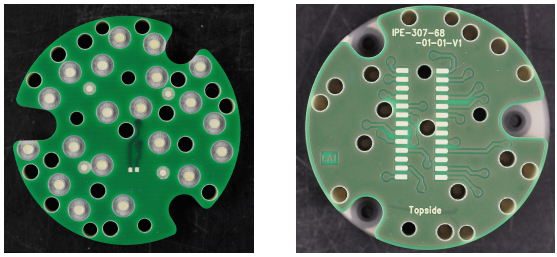

(a) Bottom side of the PCB disk. **(b)** Top side of the PCB disk.

Figure 3.8: PCB disk for electrical connection of the composite disk. The drill holes enable the molding of acoustic backing material to the rear of the piezoceramic fiber.

3.3.3 Matching Disk

The acoustic impedance of the piezoceramic has to be matched to the interfacing material to increase the transducer efficiency (see Section 2.2). When using water as front medium ($Z_F = 1.5$ MRayl) and estimating the impedance of the used piezoceramic material according to Eq. 2.13, the optimal acoustic impedance of a single matching layer is 6.47 MRayl (see Eq. 2.11).

Thermoset microwave materials used in microwave circuits (e.g. microstrips) exhibit suitable properties in this regard. TMM4 (Rogers Corporation, Chandler, USA) was chosen since it showed compliant performance in previous TAS generations. Simulation studies with the aim to maximize the bandwidth resulted in

a thickness of 0.4 mm [76]. The material comes in sheets of 1 m^2 with a 35 µm Cu layer on top, enabling electrical connection and structurization.

The processing of the matching disk was conducted as follows: At first, round samples were CNC-milled from the sheets. Then, the Cu layer was patterned to be used as uniform thickness spacer and fiducial mark for automatic detection and positioning. Structurization was done with photolithography using a negative photoresist and subsequent $FeCl_3$ etching. Sixteen disks were placed in a fixture and the photofilm was laminated on top. The setup was dried for 15 minutes at 35 °C before the photomask was manually aligned. Next, the film was exposed to UV light and developed for one minute using a 1% sodium hydroxide (NaOH) solution. After etching and cleaning, the remaining photoresist was removed using a 3% NaOH solution. Finally, the disks were cleaned and dried for 30 minutes at 35 °C. Figure 3.9 shows a matching disk at different processing stages.

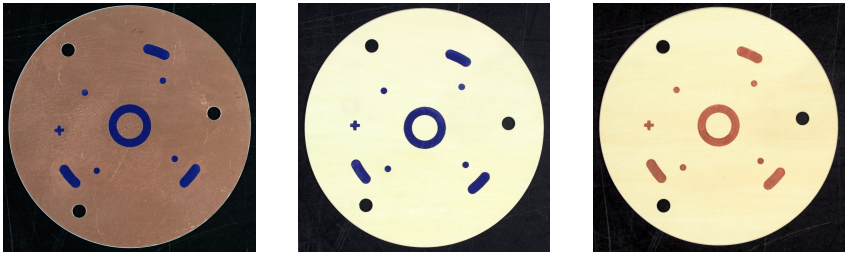

(a) Matching disk after development of the negative photoresist.

(b) Matching disk after $FeCl_3$ etching of the copper layer.

(c) Finalized matching disk.

Figure 3.9: Preprocessing of a matching disk using CNC milling and photolithography. The remaining Cu structures are used as spacers and fiducial markers.

3.3.4 Acoustic Backing

As discussed in Section 2.2.2, applying acoustic backing material to the rear of a piezoceramic results in shorter emission pulses and reduces backside reflections. Several effects have to be considered to find a suitable material. First, the acoustic

impedance has to be chosen carefully to ensure a high bandwidth without loosing too much sensitivity [55]. This is of special importance for the TAS III design since the small size of the piezoceramic fibers results in low sound pressures [85]. In addition, a suitable backing material needs to exhibit high damping properties as the maximum size of the backing layer is limited by the thickness of the PCB disk. Finally, the material has to exhibit a low enough viscosity to allow molding or dispensing.

In order to meet the requirements, a composite material made of PU (Flexovoss K6S, Vosschemie, Uetersen, Germany) and tungsten (W) powder (APS 1-5 micron, Thermo Fisher Scientific, Kandel, Germany) was investigated [77]. Using PU ensures high sound attenuation, while the added W powder increases the acoustic impedance. To minimize the development of air bubbles in the composite, air release additive (Degasser) (BYK-A 501, BYK-Chemie, Wesel, Germany) is added. The applied recipe for mixing the composite is shown in Fig. 3.10.

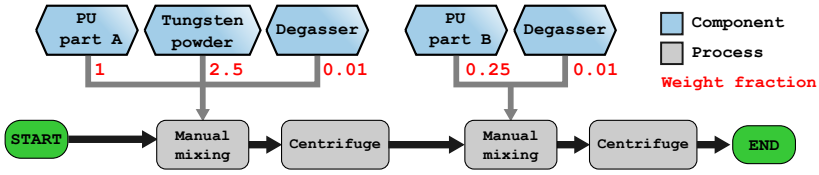

Figure 3.10: Recipe for mixing the acoustic backing composite with weight fractions normalized to the amount of PU part A.

In the following, a practical example to mix two syringes of acoustic backing composite is given:

- Twenty grams of W powder are mixed with eight grams of part A from ADH-3.
- Six drops of air release additive are added and the compound is manually stirred for one minute.
- The compound is mixed in a centrifugal mixer for 40 seconds at 1200 revolutions per minute (RPM) and degassed for 90 seconds at 800 RPM.

- Two grams of part B from ADH-3 are added, with another six drops of air release additive.
- The previously applied manual and centrifugal mixing is repeated and the composite is filled into suitable syringes.

With the stated recipe an acoustic impedance of 5.48 MRayl can be achieved [86]. The piezoceramic exhibits an acoustic impedance of approximately 30 MRayl, leading to a relatively high mismatch between the materials. On one hand, this results in lower damping at resonance and therefore a limited functional bandwidth, but on the other hand, in a higher emission sensitivity. Higher backing impedances could be achieved by increasing the proportion of W powder [57], but this would significantly affect the processability of the composite. Changing the polymer would also raise the impedance, but at the expense of damping. The utilized composite is therefore an acceptable compromise between damping, transducer bandwidth, sensitivity and producibility.

3.4 Production Process

The 3D USCT III system is designed to accommodate 128 TAS in the hemispherical measurement vessel. In order to produce this quantity of arrays, well-controlled processes are essential to maximize yield, shorten production time and reduce costs. Furthermore, the finalized arrays should exhibit low performance variability to simplify system calibration and image reconstruction. Since the assembly plays a crucial role in the functionality of a transducer, manufacturing should also be simple, reliable and reproducible.

A semi-automated manufacturing process was developed to address these requirements. It is based on batch processing techniques, meaning that multiple arrays are processed simultaneously. The production relies on standard machinery for electronic assemblies, which makes the process versatile and transferable. In the following sections, this process is explained in detail.

3.4.1 Process Overview

The production can be divided into stack assembly and packaging. In the stack assembly, the three functional disks are connected (ref. to Section 3.3). Packaging refers to integrating this stack into a protective housing. A process flow diagram is shown in Figure 3.11 including all associated components and process steps. The process steps themselves are either automated or manual. Electromechanical impedance (EMI) measurements and visual inspection are conducted to control the production quality. Additional EMI measurements were performed on eight arrays (144 transducers) at intermediate manufacturing states to derive a quality control metric (double-colored EMI fields).

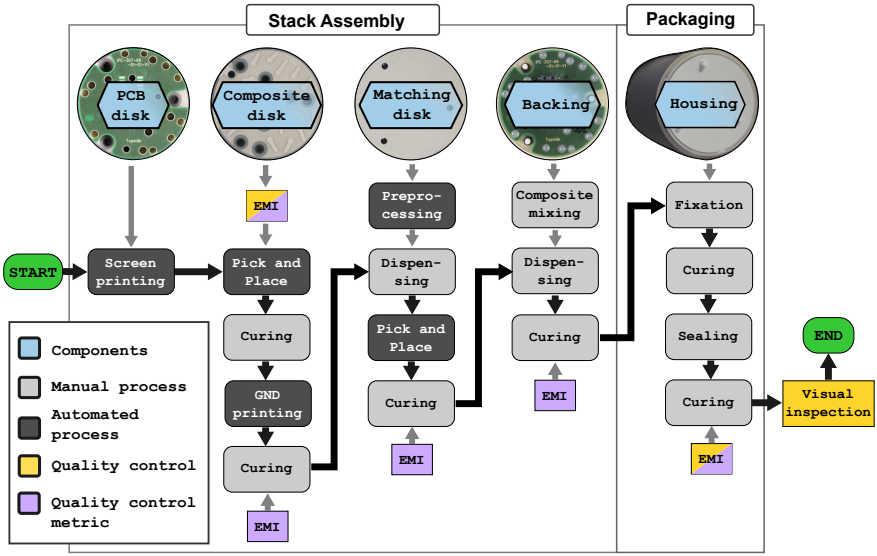

Figure 3.11: Process flowchart of TAS III production, grouped into stack production and packaging.

The connections of the disks and the subsequent packaging were realized with adhesives. Each adhesive was chosen individually to comply with the requirements of the respective bond. An overview of the utilized adhesives and the respective suppliers is given in Tab. 3.2. In order to improve surface adhesion, a solvent wipe

with Isopropyl alcohol was performed in advance [87]. Cleaning was followed by drying for 15 minutes at 35°C to avoid water and solvent residuals. Curing of the epoxies was performed at low temperatures (24°C) to minimize thermal stress. This is particularly important for the conductive adhesives, since these exhibit low bonding strengths. The low temperature required curing times of up to 48 hours for most adhesives, resulting in long manufacturing times for one array. By interleaving array batches at different stages of production, the overall production time was reduced.

The automated processes were carried out by utilizing specifically designed fixtures. These allowed to process 16 arrays simultaneously (corresponds to one batch). The alignment between the machining tools and the fixtures were realized by fiducial markers. For example, when applying a stencil print with conductive adhesive, four circular 1 mm fiducials were foreseen on the stencil. These fiducials are also present on the fixture surface, allowing automatic and accurate alignment.

Table 3.2: Adhesives used to manufacture the TAS III.

ID	Name	Supplier
ADH-1	EJ2189-LV	Epoxy Technology, Billerica, USA
ADH-2	E301-2	Epoxy Technology, Billerica, USA
ADH-3	OG116	Epoxy Technology, Billerica, USA
ADH-4	BondIt B-45	Reltec Llc., Santa Rosa, USA

Quality control measures were required to ensure full functionality of the produced arrays. The electromechanical impedance (see Section 4.1) of eight arrays was therefore measured at intermediate manufacturing states as indicated in the process flowchart in Fig. 3.11. This allows for the derivation of a suitable quality control metric and an easy evaluation of finalized transducers (see Section 4.2).

3.4.2 Challenges

The concept of stacking three functional disks on top of each other enables a simple and compact assembly. However, this also leads to challenges in manufacturing. One challenge is that once a disk is in place, it is not possible to visually inspect the underlying connection. Most joints are realized with adhesives with whom the flow of material is difficult to predict and prevent, especially when used in narrow gaps. Connections performed with conductive adhesive may cause short circuits, if improperly applied, or exhibit degradation for various reasons [88]. Hence, well-controlled processes and extensive testing is required to ensure a reliable outcome.

Another challenge is to ensure a uniform bonding line of the adhesive processes in the stack assembly, which is essential to reduce the variability and to improve the yield. For example, to establish electrical connection between the composite disk and the PCB disk, a uniform pressure must be applied over the whole surface during curing. Each of the components forming the stack have tolerances in thickness which finally add up. Hence, a fixation is required that allows for the application of pressure on each array individually. Achieving a reasonable production throughput is challenging as well. Besides logistics, the different interconnection processes rely on a variety of machinery where the non-finalized stacks are processed. The long curing times require the components to be firmly fixed for the respective time periods, while the entire setup must be portable (e.g. for curing in the oven).

A set of assembly fixtures was designed to address these challenges. Figure 3.12 shows one set of these fixtures in different views. With these, sixteen arrays were processed simultaneously. The fixture used to produce the stack, henceforth called stack-assembly fixture, is compatible with all utilized production machinery, avoiding the necessity to remove the stack at intermediate states. PCB disks are placed in the provided nests which match the outlines of the board. Additional pin holes are foreseen to ensure more accurate positioning. For automatic detection, 1 mm drills are provided in each fixture to serve as fiducial markers.

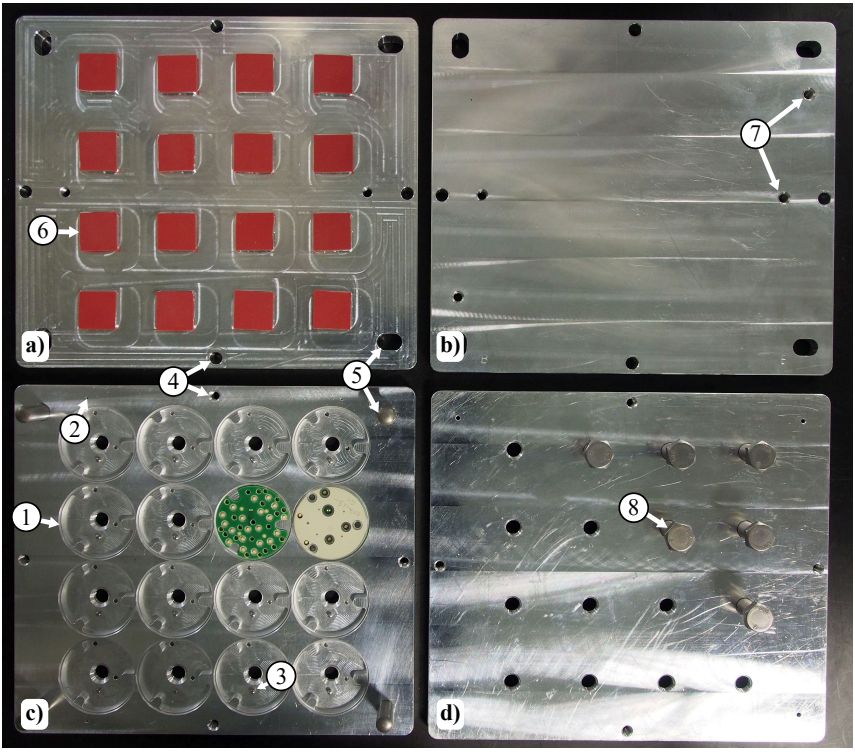

Figure 3.12: Fixtures to enable automated assembly and controlled curing of the adhesives. The upper two images show two cover plates mounted downwards (a) and upwards (b). The lower two images show the stack-assembly fixture mounted upwards (c) and downwards (d). The indicated numbers are: Nest for placing the PCB disk (1); Circular fiducial markers for automatic detection (2); 2 mm dowel pins for more accurate positioning of the PCB disks (3); Fixation screws for connecting the main fixture and the cover plate (4); Removable 8 mm dowel pins for alignment of the fixtures (5); Silicon lids for gentle pressure application (6); Auxiliary threads for placing and removing the cover plate (7); M10x1.5 screws to apply uniform pressure on each nest (8).

In addition to the stack-assembly fixture, a cover plate is required for production. Its purpose is to apply pressure on the stacks during curing of the adhesives. Four dowel pins with a diameter of 8 mm are provided to place the cover plate on top of the stack-assembly fixture with low clearance. After placing the cover plate, the structure is screwed together to enable transport and rotation. This is required

to fasten M10x1.5 screws on the backside provided for each nest. With these screws, pressure can be applied on each of the stacks individually. It is possible to mount the cover plate upwards and downwards. Mounted upwards, uniform pressure over the whole surface of the stack can be applied. Mounted downwards, a more gentle pressure application via silicon lids is realized.

Most of the components used for manufacturing are custom-made, so there is little long-term experience available. This applies to both, functional aspects and reliability. For this purpose, visual inspections as well as functional and destructive tests were performed on the components. One example involves peeling tests to evaluate the adhesion of the electrodes to the surface of the composite disks. For that, ten disks were cleaned before rolling strips of adhesive tape on both sides. The strips were peeled off after two minutes and visually inspected. With most examined composite disks, the tape could be removed without parts of the electrode detaching. However, two disks were found to have significant detachment of the electrode, one of them is shown in Fig. 3.13. As a countermeasure, additional surface preparations and a change of the utilized adhesive were agreed upon with the supplier. This will increases the adhesion of the electrode for future batches.

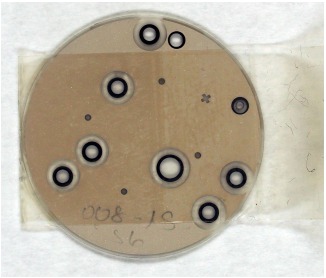

(a) Composite disk with an attached strip of adhesive tape.

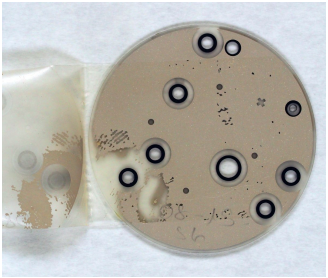

(b) Composite disk after peeling the tape with some of the GND electrode detached.

Figure 3.13: Preliminary peeling tests to evaluate the adhesion of the printed electrodes. Adhesive tape was rolled onto composite disks (a) and subsequently peeled off (b).

3.4.3 Stack Assembly

The process started by establishing an electrical connection of the transducer electrodes V_{in} and GND with the PCB disk using conductive epoxy (ADH-1). This adhesive was selected because it is specified for room temperature curing, exhibits an intermediate viscosity and a high thixotropic index. These properties enable screen and stencil printing with high shape retention of the print [89]. For applying ADH-1 on the PCB pads, an inline screenprinter (Ekra E4, As-Equipment, Hamburg, Germany) was used. The stack-assembly fixture was placed in the device and aligned with the stencil before printing. An example after successful printing is shown in Fig. 3.14a.

In the next step, the composite disk was placed on top of the preprocessed PCB disks. The stack-assembly fixture was removed from the screenprinter and placed in an automatic die bonder (Datacon EVO2200, Besi, Radfeld, Austria). There, the main tool picked up a composite disk from an auxiliary tray, aligned the position and placed it accurately on top of the PCB. The process is visualized in Fig. 3.14b, where the pick-up tool is placing a composite disk. During curing it was crucial to apply uniform pressure over the whole surface of the composite disk to ensure reliable electrical connection of all integrated transducer. Hence, the cover plate was mounted upwards (ref. to Fig. 3.12b).

The production process continued by establishing the GND connection with a through-hole provided on the composite disks. At first, the holes were filled with ADH-1 using a manual dispenser. Then, a screen printing process was conducted. As shown in Fig. 3.15a, approximately nine grams of ADH-1 were horizontally distributed on top of the screen. The squeegee pressed the adhesive through the opened mesh to print a 35 μ m thick layer. This ensured reliable electrical connection of the GND electrode to the underlying pads. A picture emphasizing the printed GND connections is showed in Fig. 3.15b. After curing the GND print, the SMD temperature sensor was soldered to the designated pads.

In order to improve the mechanical stability of the connection between the composite disk and the PCB disk, 15 mg of ADH-2 were dispensed on top of the

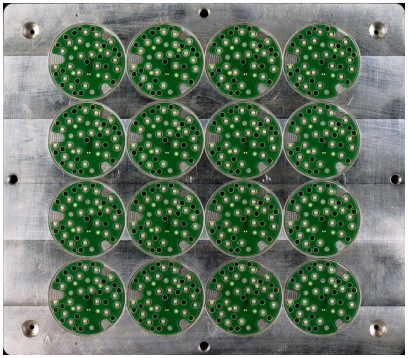

(a) Stack-assembly fixture equipped with 16 PCB disks after stencil printing.

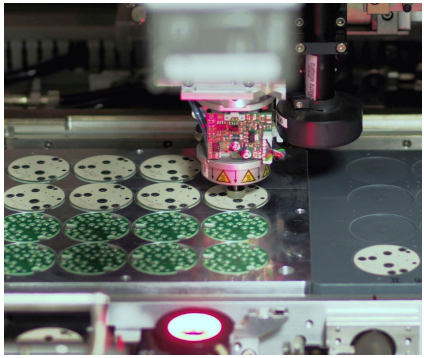

(b) Pick-and-place of composite disks on PCB using an automatic die bonder.

Figure 3.14: Establishing the electrical connection of the PCB disk to the composite disk by stencil printing of conductive adhesive (a) and subsequent pick-and-place of composite disks onto PCB disks (b).

soldered temperature sensor. This two-component epoxy exhibits low viscosity, low water absorption, high mechanical strength and curing at room temperature. In addition, the adhesive is biocompatible and can therefore be used for components of the USCT device that are in contact with patients. Hence, it was also used for the next process step to connect the matching disk with the preprocessed assembly.

When connecting the matching disk, it is crucial to avoid air cavities since these would cause high reflections. In addition, a uniform adhesive layer is required to avoid lens effects or a skewed sound field. Tests were conducted to find the optimum amount and distribution of ADH-2. As a result, dispensing 13 droplets of in total 45 mg of adhesive over the surface of the composite disk led to an uniform bonding layer. Figure 3.16a shows one tray of preprocessed stacks after dispensing ADH-2 in the optimum pattern.

For accurate placement of the matching disk, the automatic die bonder was used. In this process, matching disks were assembled on a tray designed to be compliant with the flip-chip carrier compartment. The disks were picked up using the flip-chip tool, inspected, aligned and finally placed on top of the composite disk (see

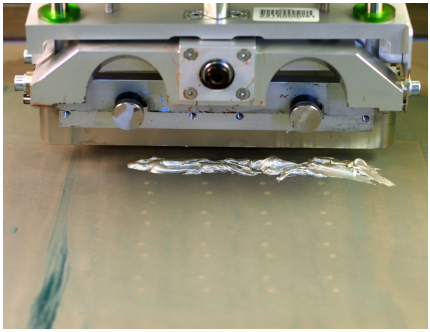

(a) Application of ADH-1 on the screen to establish the GND connection.

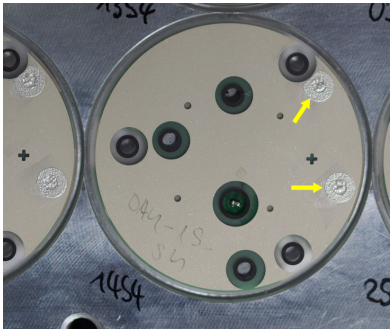

(b) Screen-printed GND connection, emphasized with the yellow arrows.

Figure 3.15: Establishing the GND connection by screen printing a 35 µm thick layer of conductive adhesive.

Fig. 3.16b). The minimum thickness of the bonding layer is defined by the height of the silk-printed GND electrode and the copper spacers from the matching disk. Ensuring this thickness required curing under pressure. Hence, the cover plate was mounted downwards, where the provided silicon sheets distribute the pressure over its surface and avoid cracks in the matching disk. The size of the sheets was chosen slightly smaller than the disk diameter to prevent displaced adhesive.

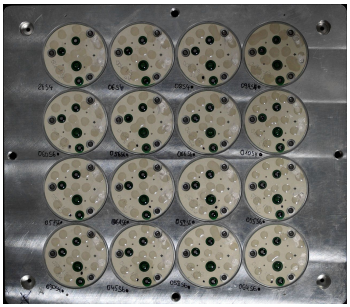

(a) Dispensed droplets of ADH-2 on a tray of preprocessed stacks.

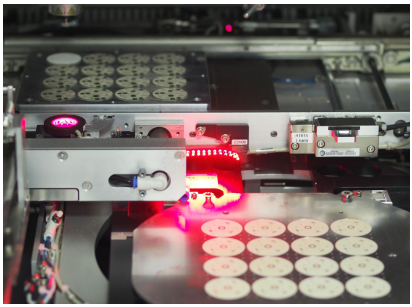

(b) Pick-and-place of matching disk onto preprocessed stacks.

Figure 3.16: Connection of matching disks with composite disks: Droplets of ADH-2 are distributed over the surface of the composite disk (a), with subsequent automatic placement (b).

In order to finalize the stack production, the acoustic backing material was applied to the rear of the piezoceramic fibers. For that, the drill holes provided on the PCB disk were filled with backing composite. The composite was dispensed using a conical tip and low pressure (0.8 bar) to avoid segregation of air inclusions. Since each hole was filled individually, this step was labor-intensive and time-consuming. A key challenge was fast processing, since the composite has a pot life of approximately 30 minutes. Figure 3.17a shows one array after dispensing the backing composite. Before the stacks were integrated into the housing, a pin connector (Samtec RSM-113-02-S-D) was soldered on the PCB and the residual flux removed. The front-end electronics will be plugged into this connector, allowing signal amplification and conditioning close to the piezoceramic. Figure 3.17b shows two trays of finalized stacks before further processing.

(a) Stack after dispensing the acoustic backing material.

(b) Finalized stacks before integration into the housing.

Figure 3.17: Finalizing the stacks by filling the holes with acoustic backing material (a). Final state before packaging (b).

3.4.4 Packaging

The image reconstruction algorithms of the 3D USCT system require accurate positioning of the transducers in the measurement vessel. Position inaccuracies exceeding $\lambda/4$ with respect to the center frequency can already lead to destructive

interference of back projections. This interferes with coherent imaging techniques, resulting in a lower image quality [58].

In order to minimize thickness tolerances of finalized arrays, the integration of the stacks into the housing was conducted in reverse direction. This ensured that the surface of the matching disk is flush with the housing in all cases. An additional fixture was designed where eight stacks can be positioned with dowel pins on a polished aluminum plate, shown in Fig. 3.18a. The housing was then placed on top, and a preliminary fixation was achieved using three drops of ADH-3 according to the arrows displayed in Fig. 3.18b. The high viscosity and quick fixation of this UV-curable adhesive prevented the flow of material into the structure and fixture below.

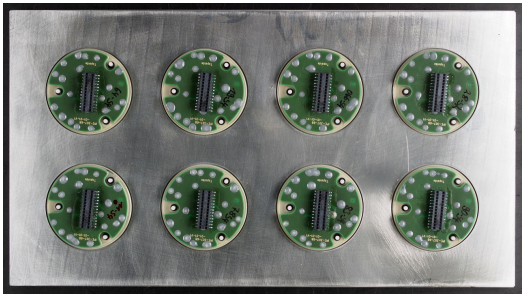

(a) Fixture for inserting the stack into the housing.

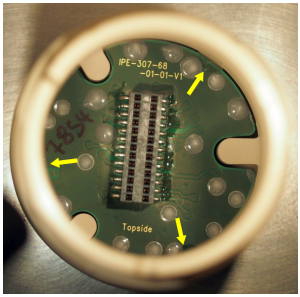

(b) Inner view of one housing where the arrows mark the points of preliminary fixation.

Figure 3.18: Preliminary fixation of the housing with the stack using a fixture (a) and three drops of UV curable adhesive (b).

ADH-3 was exposed to UV light for two minutes using a spot lamp (Dymax Blue-Wave 50, Wiesbaden, Germany) to start the curing process. Then, weights were placed on top of the housings, shown in Fig. 3.19a, to ensure planar alignment. The weights remained for 30 min on the setup to fully cure the adhesive.

In the next step, the assembly was removed from the fixture and the adhesive joints on the front indicated in Fig. 3.19b were sealed with ADH-2. By using ADH-2, reliable filling is ensured due to its low viscosity and high mechanical strength.

Moreover, since ADH-2 is applied to the surface of the arrays, its biocompatibility is an important requirement.

(a) Placement of weights to ensure planar alignment during curing.

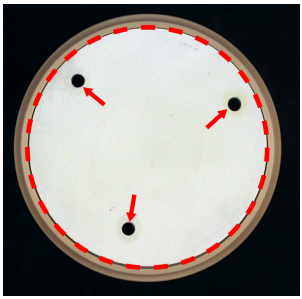

(b) Front view of the assembly with marks where the adhesive sealing is applied.

Figure 3.19: Preparing the assembly for the final sealing process: Applied weights to ensure planar fixation (a); Joints and regions to be filled with ADH-2 (b).

For mounting (and dismounting) the arrays in the measuring vessel, three ceramic pins were inserted into the provided holes. Ceramic was chosen as an electrically non-conductive alternative to stainless steel in order to meet safety requirements. An additional safety measure was foreseen by filling the edge gap with ADH-4 as shown in Fig. 3.20a. This epoxy was used for its high chemical resistance and sealing properties.

The second sealing process is necessary to comply with the single-fault safety requirement from medical device regulation. It states that for critical applications, a second safety measure must be foreseen [52]. This process completes the TAS III manufacturing, where a set of 16 finalized arrays is shown in Fig. 3.20b. In the next step, the produced arrays were tested and evaluated before the integration in the 3D USCT III device.

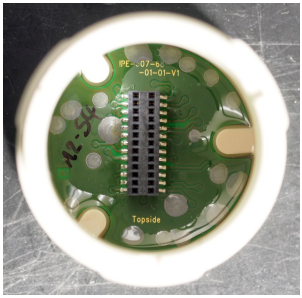

(a) Inner view of finalized transducer with second sealing at the edges.

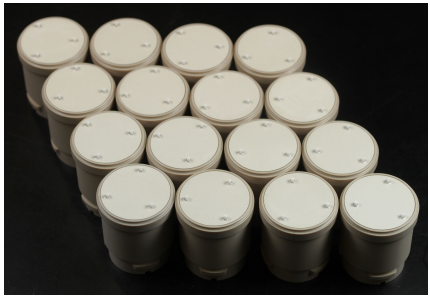

(b) Set of finalized TAS III.

Figure 3.20: Completing the manufacturing by filling the inner edge gap with ADH-4 (a), leading to finalized TAS III (b).

3.5 Summary and Discussion

With the evolution of the 3D USCT technology, a variety of transducer array designs were manufactured and tested. The gained findings resulted in a specific set of required ultrasound characteristics and design features, summarized in Tab. 3.1. Most challenging to achieve are the pseudo-random transducer arrangement, very large bandwidth and isotropic ultrasound emission. An array design was developed, where single PZT fibers can be randomly placed, embedded in polymer and processed into the desired shape [78]. The resulting piezocomposite disks hold 18 single-fiber transducers with a diameter of 460 µm and a length of 600 µm. For finalizing the arrays, a matching disk and PCB disk are attached to the front and back side, respectively. Acoustic backing is applied to the backside of the transducers via cavities foreseen in the PCBs. Interconnections are realized with conductive and non-conductive adhesives. The simple stacking concept enables high integration and automated production. By integrating this stack into a cylindrical plastic housing, a waterproof, rotatable and electrically isolating transducer array is realized to enable randomized transducer positions in the 3D USCT III measurement vessel.

In order to produce the required 256 TAS III for two 3D USCT III systems, a semi-automated manufacturing process was developed. The process relies on batch processing techniques, where 16 arrays are processed simultaneously. This enables easy scaling for future industrialization of the 3D USCT technology. Fiducial markers and a variety of mechanical fixtures enable automated screen and stencil printing of adhesives as well as pick-and-place processes for time-efficient manufacturing. Initial processing and handling difficulties were resolved iteratively, resulting in stable processes for final batches. The application of uniform pressure using cover plates proved to be essential for reliable production.

Automated positioning of composite disks with the die bonder was found challenging in many cases. The printed fiducial markers exhibited a limited sharpness, leading to difficulties in edge and shape detection. Reliable processing was only achievable when reducing the detection accuracy down to 30%. The resulting inaccuracies required manual intervention in about one in ten cases. Positive markers (structures actively printed on the substrate) showed higher detection accuracy and were foreseen for future batches. However, since the resolution of printed structures is limited, different approaches to realize fiducials should be considered. For example, by integrating additional high-contrast structures such as carbon rods or bars in the mold of the composite disk, more robust detection is achievable.

Using adhesives for all mechanical connections requires long resting times since all adhesives were cured at 24°C for safety and stability reasons. This adds up to a total production time of at least two weeks for a single array. By using higher temperatures during curing, the production time could be significantly reduced. The higher thermal stress can be buffered with firm fixation during curing and suitable temperature profiles. First tests at a curing temperature of 80°C and a temperature slope of 20°C/h were found appropriate.

The processes for achieving GND connection were very time consuming since repeated filling and printing of conductive adhesive was required. By directly integrating conductive structures in the composite disks, these process steps could be avoided in future designs. However, a new design should still enable visual

inspection of the connection. Hollow fibers, similar to those currently used for the GND connection, and overprinting of the electrodes could enable a direct connection.

The packaging of the stacks into the housing was mostly performed manually. Hence, it was very time-consuming and prone to larger positioning errors. Especially the integration of the ceramic pins required additional adhesive bonds, inspections and adjustments. Different solutions for mounting the TAS in the measurement vessel should be considered for future designs. This would greatly simplify packaging and enable more automated integration.

4 Quality Control and Inspection

In this chapter, the produced TAS III are evaluated with respect to the achieved quality and yield. For quantitative analysis and evaluation, a quality control metric to derive one-dimensional classifiers is proposed. With these classifiers, finalized transducers can be categorized into groups of "pass" and "fail". This ensures that only functional arrays are integrated in the 3D USCT III device.

Temperature cycling tests are presented subsequently, where the chosen test conditions match those specified in medical device regulations. Thus, a first assessment is possible if important clinical safety standards can be met. In addition, the results of the cycling tests enable a first estimation of reliability and a definition of a safe temperature range for operation.

4.1 Electromechanical Impedance Characteristics

Piezoelectric ultrasonic transducers can be used as transmitters and receivers due to the direct and reverse piezoelectric effect. If excited with signals of varying frequencies, the characteristic vibration behavior of a transducer can be assessed in terms of its EMI. The measured EMI does not only reflect the material's condition and behavior, but also the surrounding structure. This is used for instance in structural health monitoring, where transducers are embedded to monitor changes in material compositions and structures [90].

In order to quantify the transducer condition for performance analysis and statistical evaluation, a variety of characteristics can be derived from a single EMI measurement. These characteristics reflect the resonating behavior, the EM coupling and the electrical impedance [91, ch. 1]. In this work, ten specific characteristics are used to quantify a transducer's condition. These characteristics, together with a short description, are listed in Tab. 4.1. Five of them are directly derived from the EMI measurement and another three are based on the calculated electrical input power. The impedance Z_s and loss factor D are obtained at a frequency of 1 MHz, where the transducer exhibits mostly capacitive behavior. The effective EM coupling k_{eff} is calculated according to Eq. 4.1, and the thickness coupling factor k_{33} according to Eq. 4.2 [42].

Table 4.1: Characteristics derived from EMI measurements to quantify a transducer's behavior.

Char.	Description	Char.	Description
f_r	Resonance frequency	φ_t	Maximum phase angle
f_a	Anti-resonance frequency	Z_s	Impedance at 1 MHz
f_c	Center frequency	D	Loss factor at 1 MHz
k_{33}	Coupling factor in 33-direction	bw_{el}	3 dB bandwidth of input power
k_{eff}	Effective coupling factor	P_{in}	Input power at resonance

$$k_{eff} = \sqrt{\frac{f_a^2 - f_r^2}{f_a^2}} \tag{4.1}$$

$$k_{33} = \sqrt{\frac{\pi}{2} \cdot \frac{f_r}{f_a} \cdot \tan\left(\frac{\pi}{2} \cdot \frac{f_a - f_r}{f_a}\right)} \tag{4.2}$$

For measuring the EMI, a three channel vector network analyzer (Bode100, Omicron Lab, Klaus, Austria) was used. Effects arising from the measurement setup were compensated by an open-short-load calibration procedure at the beginning of each measurement. This procedure is recommended when using non-standard

length cables, since not only offsets but also residual circuit elements such as the cable inductance are compensated [92, ch. 4]. Figure 4.1 shows an exemplary measurement of one TAS III transducer, where the directly obtained EMI characteristics are indicated. In later chapters, these characteristics are compared at different manufacturing and testing states to derive suitable quality control and performance analysis metrics.

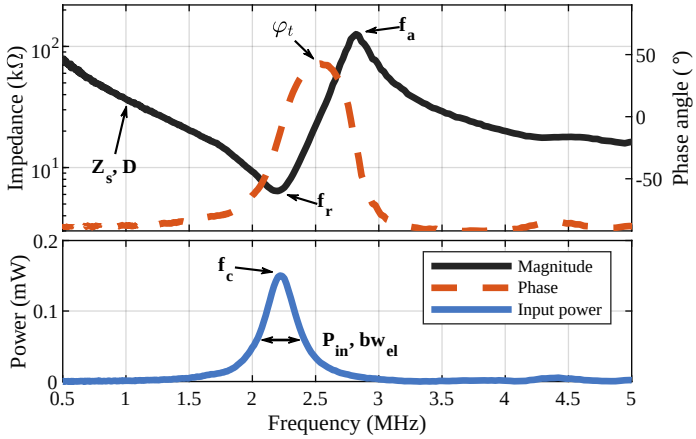

Figure 4.1: Measured EMI of one TAS III transducer and the corresponding electrical input power. The upper graph depicts the impedance magnitude over frequency, the lower graph the phase angle. From each measurement, the indicated characteristics can be derived to quantify the transducer condition.

4.2 Quality Control Measure

Well-defined quality control measures ensure full functionality of the produced arrays. For classification of a transducer into categories, e.g. "pass" and "fail", clearly defined quantitative parameters are needed, which in the best case are easy to obtain. Ultrasound tests are a feasible method but time-consuming and difficult to conduct. In contrast to that, EMI measurements are much easier to perform and

enable condition monitoring of non-finalized transducers (e.g. before packaging). This makes EMI measurements well-suited for quality control.

Transducer performance depends on proper connections with surrounding materials. The formation of cavities on the front or the rear of the piezoceramic fiber (see Fig. 4.2) is a main source of manufacturing defects since adhesives were used for interconnecting all layers and structures. Cavities would cause high reflections, a lower bandwidth and are in most cases not visually detectable. Therefore, a measurable non-destructive classifier is needed. In the following sections, a quality control method based on the relative change of EMI characteristics is presented. This work was already published in [5], but additional details and the application of the method are given below.

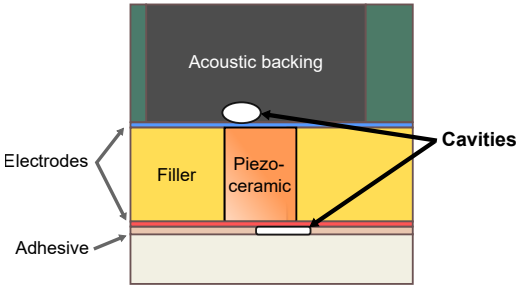

Figure 4.2: Schematic cross section of a single transducer, with cavities or air bubbles which might occur on the front and rear side of the piezoceramic fiber.

4.2.1 Dataset from Manufacturing States

Connecting the front or rear of the piezoceramic fibers causes a change in their EMI, e.g. a shift in the resonance frequency and the corresponding phase angle. To assess if this change can be used as a reliable classifier, statistical analysis of ten EMI characteristics was conducted. These characteristics were already introduced in Section 4.1. A random subgroup of eight TAS III was taken from the production. All transducers from this subgroup were tested at intermediate manufacturing

states, indicated in the process flowchart in Fig. 3.11. This procedure resulted in a dataset containing EMI characteristics of 144 transducers at five manufacturing states. These five states are illustrated in Fig. 4.3.

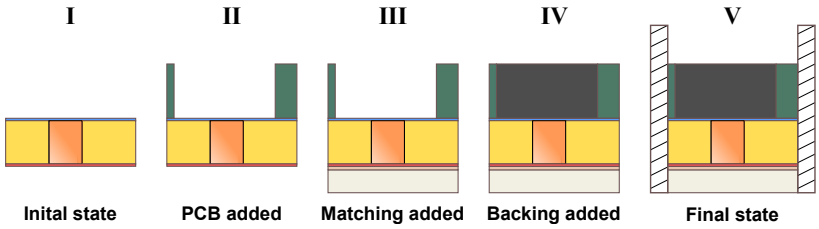

Figure 4.3: Five manufacturing states where EMI measurements were conducted to derive a quality control metric. In state V, an additional adapter is required to measure the EMI.

Not only modifications of the mechanical structure of a transducer but also changes in the electrical circuit conditions influence the EMI. Changing the measurement setup by using different cables, adapters, etc. will therefore affect the derived statistics and might lead to classification errors. To some extent, this can be compensated by a open-short-load calibration method [92, ch. 4], but already small changes in the setup (cable movements, replugging etc.) alters the measured impedance. A suitable classifier should therefore be sensitive to modifications in the mechanical structure, but insensitive to change in the electrical circuit connection. During assembly, modifications and changes occur in both, the mechanical and the electrical domain. Hence, a detailed assessment of the manufacturing states and the respective measurement conditions is required:

I. *Initial state*: Unprocessed composite disk. The piezoceramic fibers vibrate in air and the measurement is conducted using needle probes.

II. *PCB added*: Adding the PCB disk introduces a change in the measurement circuit as the PCB exhibits a considerable parasitic capacitance. The EMI is measured using the pads on the PCB's top side with needle probes.

III. *Matching added*: The matching disk covers one end of the piezoceramic fiber while the other end still resonates in air. The EMI is measured once again with needle probes.

IV. *Backing added*: The acoustic backing covers the other end of the piezoceramic fiber. The EMI is measured with needle probes on the pads of the PCB disk.

V. *Final state*: Finalized arrays after integrating the stacks into the housing. To access the PCB, an additional adapter board is necessary. This adds a parasitic capacitance and inductance to the resonator.

4.2.2 Classification Method

A common procedure to decide if two random variables exhibit a significant difference are hypothesis tests (e.g. the paired T-test) [93, ch. 9]. The decision criteria, the probability or p-value, is set to a certain threshold (often 0.05) and the null hypothesis is either rejected or accepted. If rejected, a significant difference between the two variables is present [94, ch. 10]. These inference methods mostly assume a normal distribution of the population and require a strict definition of the p-value [95, 96].

An alternative way to quantify the difference of two random variables is the overlapping coefficient (OVL) [97]. It represents the total intersected area of two probability distributions $\mathrm{p_A}$ and $\mathrm{p_B}$ from random variables, mathematically stated in Eq. 4.3. The factor 1/2 is needed to normalize the total probability to one.

$$OVL(p_A, p_B) = \frac{1}{2} \int_{\mathbb{R}} \min(p_A(x) \cdot p_B(x)) dx \tag{4.3}$$

Analyzing the EMI characteristics with respect to their probability distribution showed deviations from normal distribution. Fitting a Gaussian curve to this data and calculating the OVL would therefore lead to errors. A solution to account for non-normal distributions is to calculate a probability density function (PDF)

for each characteristic. The unknown distributions $\mathrm{p_A}$ and $\mathrm{p_B}$ can be estimated according to Eq. 4.4 and Eq. 4.5 [98], where K is a Kernel function (e.g. Gaussian) and h is the bandwidth factor, which controls the smoothness of the density curve. More details on this method can be found in [99], with a practical application guide in [100] for the programming environment R.

$$\hat{p}_A = \frac{1}{nh} \sum_{i=1}^{n} K\left(\frac{x - x_i}{h}\right) \tag{4.4}$$

$$\hat{p}_B = \frac{1}{nh} \sum_{i=1}^{n} K\left(\frac{y - y_i}{h}\right) \tag{4.5}$$

Before conducting the evaluation it is important to ensure that the dataset is representative, or in other words that the transducers exhibit a somewhat standard behavior with respect to the entire transducer population. Therefore, a statistical analysis at manufacturing state I was conducted. Figure 4.4 shows the histograms of two EMI characteristics, the center frequency f_c and the EM coupling factor k_{33} from the measured subset. Both histograms contain a group of four transducers which deviate significantly from the mean. To proceed, the error-outlier procedure stated in [101] was followed. First, a visual inspection of the distributions was performed, followed by a quantitative test. As a quantitative test, the generalized extreme studentized deviate [102] was calculated, which marked these four transducers as outliers. These outliers could be traced back to problems in polarizing the piezoceramic fiber and were therefore removed from the dataset.

Calculating the OVLs for the EMI characteristics of the remaining 140 transducers allows for quantification of separability. A graphical example of how OVLs are calculated is given in Fig. 4.5. As shown there, the OVL corresponds to the total intersected area of two estimated PDFs. These PDFs represent the distribution of a single characteristic at the current and the preceding manufacturing state. The point where the two PDFs intersect (ISP) marks the point where the probability of one PDF exceeds the other. This point is well suited to be used as one-dimensional classifier for the respective characteristic. The ISP also enables the division of

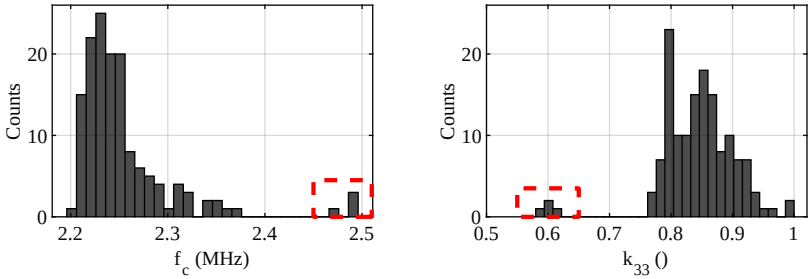

(a) Center frequency f_c at the initial state.

(b) Coupling factor k_{33} at the initial state.

Figure 4.4: Histograms of two EMI characteristics obtained from the TAS III subset at manufacturing state I. Four transducers which deviate significantly from the mean are marked with the red-dashed square.

the OVL in probabilities for false negative and false positive decisions. In this case, a false positive decision means that the matching layer is connected but does not pass the test. A false negative decision means that the matching layer is not properly connected, but still passes the test. Hence, the probability of false negative decisions should be as low as possible to minimize the likelihood that a defective or partially defective transducer will be included in the system.

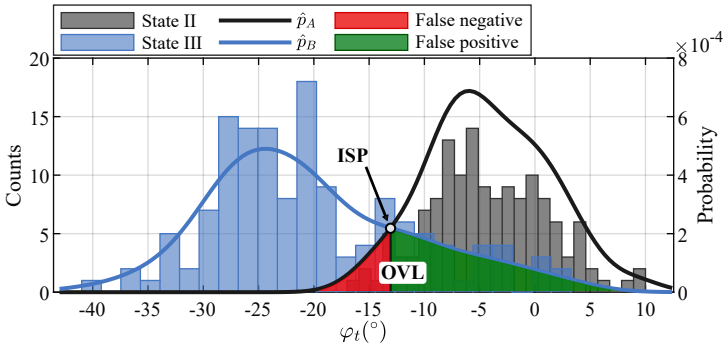

Figure 4.5: Graphical display of the overlap of two PDFs estimated from φ_t at the manufacturing states II and III. The OVL corresponds to the total intersected area and can be divided into a probability for false negative and false positive decisions via the ISP.

In the next step, the OVL was calculated for the ten EMI characteristics and all five manufacturing states. As explained above, characteristics that exhibit high OVLs under varying electrical circuit conditions and low OVLs when changing the mechanical structure are best suited for quality control. Figure 4.6 shows the calculated OVLs for all EMI characteristics between the respective manufacturing states. The closer the OVL is to zero, the smaller the overlap and consequently the better the separability. Based on these results, several characteristics seem suitable for reliably separating one or more manufacturing states. For example, the resonance frequencies f_s and f_c are sensitive to detect a properly connected matching layer and relatively insensitive to changes in the electrical circuit conditions. However, applying the acoustic backing leads only to minor changes in these resonances, which is not sufficient for reliable separation.

The single characteristic best suited for quality control is the bandwidth of the electrical input power $\mathrm{bw_{el}}$. It exhibits OVLs with probabilities above 0.69 when the electric circuit conditions change, and overlaps lower than 0.025 after covering

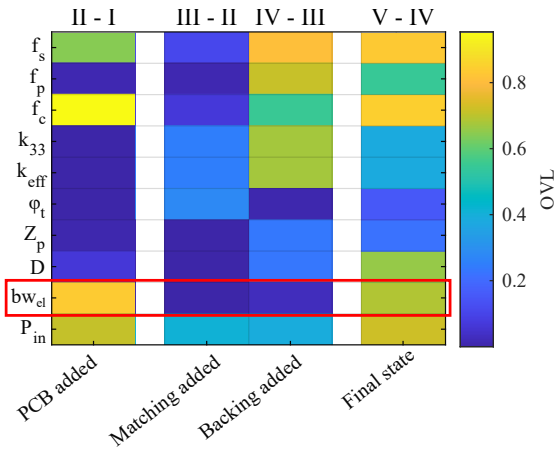

Figure 4.6: Matrix with color-coded OVLs for the EMI characteristics and the manufacturing states. The matrix is separated into changes in the electrical circuit conditions (II-I and V-VI), and in changes in the mechanical structure of the transducers (III-II and IV-III). The most promising characteristic bw_{el} for one-dimensional quality control is marked with the red box.

the piezoceramic fibers on either end. With respect to transducer design, these results are plausible since the purpose of the matching layer and the acoustic backing is to extend the functional ultrasound bandwidth (see Section 2.2).

The presented method enables the derivation of a classifier for the correct attachment of the matching disk as well as the acoustic backing. In order to limit the maximum acceptable $\mathrm{bw_{el}}$, an upper threshold is required. It can be derived from a more classical approach by setting a probability threshold. Here, a threshold of $p = 0.001$ was chosen for the upper end of the estimated PDF in the final state. This threshold accepts a very wide range of transducers, since a high bandwidth is in general desirable. However, a reliable filtering of defective transducers is still given. The three resulting classifiers with the respective probabilities for false negative and false positive decisions are listed in Tab. 4.2.

Table 4.2: Three classifiers for quality control of finalized TAS III with respect to their electrical input power bandwidth $\mathrm{bw_{el}}$.

Classifiers	**bw$_{el}$ value**	**False neg.**	**False pos.**	**OVL**
C1: One end connected	0.35 MHz	<0.001	<0.001	<0.002
C2: Both ends connected	0.61 MHz	0.006	0.019	0.025
C3: Upper threshold	1.09 MHz	0.001	n/a	n/a

Figure 4.7 summarizes the results of the quality control method. It shows the histograms of $\mathrm{bw_{el}}$ for the five manufacturing states with their estimated PDFs. The derived thresholds for quality control are marked with the dashed lines, which enables the classification of finalized transducers. To validate these results, qualitative ultrasound tests were conducted with the transducers from the dataset. All transducers emitted expected levels of ultrasound, confirming the validity of the presented method.

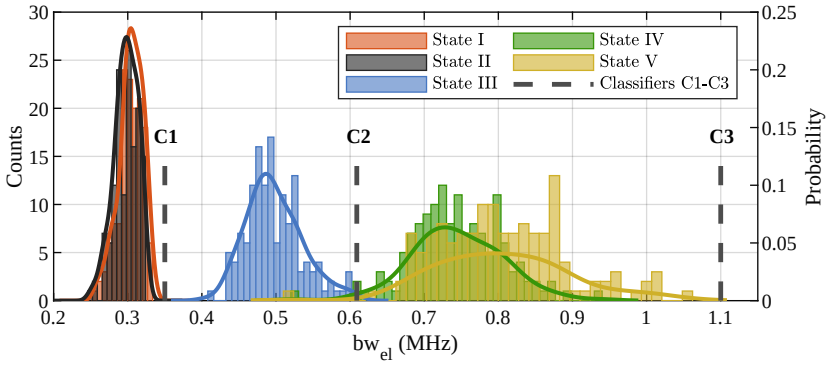

Figure 4.7: Histograms and estimated PDFs (solid lines) of $\mathrm{bw_{el}}$ from the five manufacturing states of 140 transducers. C1-C3 are the derived classifiers for quality control.

4.2.3 Results

The derived quality control metric was applied to categorize finalized transducers. Figure. 4.8 shows the histogram of $\mathrm{bw_{el}}$ from 2466 transducers, corresponding to 137 arrays. Out of all transducers, 96.4% fall between the classifier C2 and C3 and are therefore categorized as "pass". A total of 86 transducers are classified as "fail". Out of this group, 12 transducers exceed the upper threshold C3. These reflect most likely defective or partially defective transducers where the very high bandwidth results from measurement errors. The remaining 74 transducers fall beyond C2, indicating either manufacturing defects or substantial deviation from the expected performance due to unknown reasons (defects, high variations etc.).

A closer analysis of the 74 transducers that lie between C1 and C2 shows that a total of 51 different arrays are affected. Out of these arrays, 33 hold one transducer categorized as "fail", three arrays four, and two arrays five. The 3D USCT imaging approach is relatively insensitive to single transducers which deviate from the normal behavior. The reason for this is the high number of channels and possibility of multiple aperture positions. Therefore, it was decided that only the five arrays that had four or more defective transducers would not be used for integration into the system.

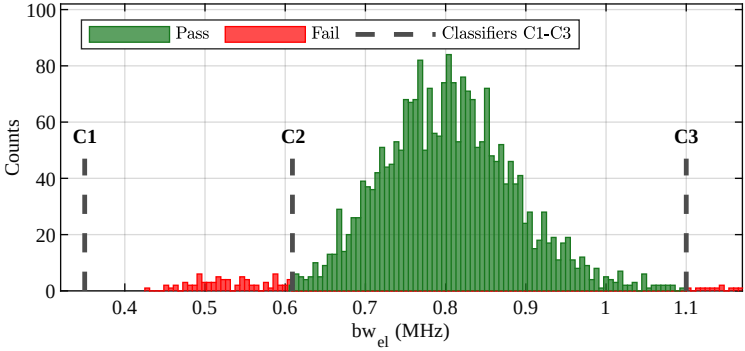

Figure 4.8: Histogram of $\mathrm{bw_{el}}$ from 2466 transducers (137 TAS-3) and three classifiers (C1-C3) derived from the presented quality control method. These allow categorization of the measured transducers into groups of "pass" (96.4%) and "fail" (3.6%).

The reason why a transducer is categorized as "fail" can be manifold. The quality control method suggests that at least one end of the piezoceramic fiber was not properly connected. However, since no exclusive incoming inspection for the composite disks was performed, some of the deviations may be due to the piezoceramic fiber itself. Therefore, a rigorous quality analysis of the composite disks is recommended for future productions to rule out this possibility. The five arrays with four or more failures experienced most likely a problem during manufacturing. Optical inspection did not show any signs of defects, suggesting that the defects are located in one of the components or in between the layers. Overall, with more than 95% of the transducers having passed the quality control test, the developed manufacturing process proved to be well-suited for producing functional TAS III.

4.3 Temperature Cycling

Extensive clinical testing is necessary to proof safety and effectiveness of the 3D USCT III system for the detection of breast cancer. The harmonized IEC 60601-1-2 standard [52] lists essential requirements and tests to ensure

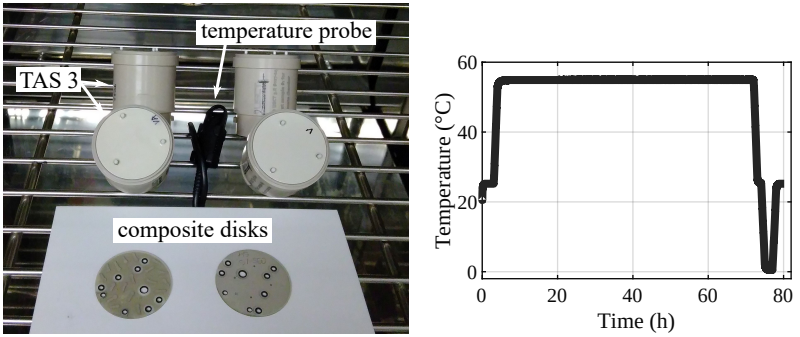

(a) Four TAS III placed in a climate chamber with temperature probe and reference disks.

(b) Measured temperature profile of one cycle.

Figure 4.9: Temperature cycling test setup for a first assessment of the reliability of finalized TAS III (a) and the applied temperature profile of a single cycle (b).

the safety of a medical device. An important test is listed in section 8.9.3.4 of the standard. It describes isolation resistance tests after temperature cycling. There, a device under test (DUT) is exposed to predefined temperatures and humidity, with a following measurement of leakage current at a specified DC voltage.

The isolation resistance test is aimed for ensuring patient safety, thus full functionality of the DUTs is not required afterwards. However, a first assessment of reliability of the transducers can be obtained by also performing functional tests. Four TAS were placed in a climate chamber (WK1-340, Weisstechnik, Reiskirchen, Germany) with a calibrated temperature probe (EL-GFX-D2, Lascar Electronics, Salisbury, England) in the center. Two unprocessed composite disks were placed next to them for reference. Figure 4.9a shows the utilized test setup. The temperature profile of one cycle measured with the probe is shown in Fig. 4.9b. It starts from room temperature at 24°C, rises over 2 h to 55°C where it remains for 68 h. Then, the temperature is regulated down to 24°C, remains constant for 1 h before it reaches the minimum of 0°C. At the lowest point it stays for 1 h, before rising back to room temperature. The temperature values and dwell times are defined by the standard, the gradients were chosen arbitrarily.

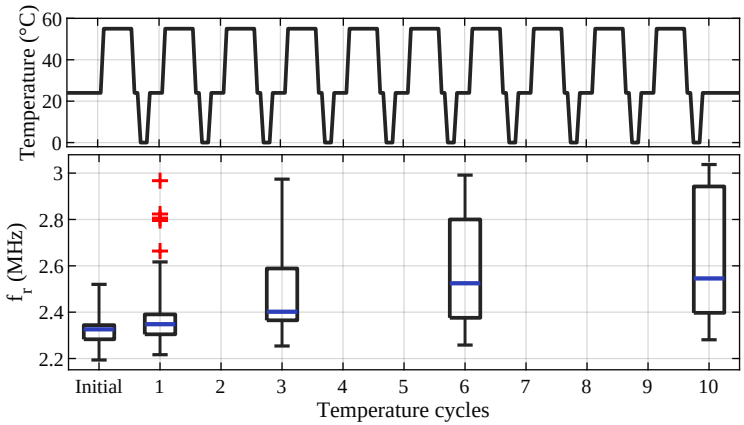

Figure 4.10: Results of temperature cycling test according to IEC 60601. The applied temperature profile is schematically shown in the upper graph, and the distribution of f_r measured after some of the cycles is given as boxplots below. The length of the total range (length of whiskers) is set to three times the interquartile range to include a wide range of measured values. The median is shown in thick blue, the standard deviation is within the black box and outliers are marked with red crosses.

In compliance with IEC 60601-1-2, ten temperature cycles were run. In order to evaluate the functionality, EMI measurements were conducted at the beginning, and after the first, third, sixth, and tenth cycle. The resonance frequency f_r was chosen as evaluation criterion because it reflected best the condition of the piezoceramic fiber [91]. Figure 4.10 shows the results of this test series. All ten temperature cycles are shown schematically in the upper graph and the distribution of f_r is given as boxplots below.

After the first temperature cycle, four transducers were classified as outliers, and a slight rise in mean was found. This indicates that the applied thermal stress already affected the performance significantly. After the third cycle, the interquartile range of f_r becomes much broader, with an increase in mean of 0.19 MHz from the initial condition. This trend continues after the sixth cycle, with a further rise in f_r. The distribution after the tenth cycle is similar to that after the sixth cycle, suggesting that most of the effects have already occurred after the first few cycles.

Further analysis showed that a rise in f_c corresponds to a drop in the electrical input power P_{in}, leading effectively to a lower ultrasound output. The data also showed that not all transducers were affected equally but the average increase occurred due to individual transducers whose behavior changed significantly. This means that damages had most likely occurred either in the piezoceramic or in the assembly. Analysis of the unprocessed composite disks used for reference showed no significant changes in performance. This indicates that the damage occurred either in the assembly or in one of the other components.

A second temperature cycling test was conducted to narrow down the temperature range where changes in the assembly occurred. Two TAS III were exposed to static and dynamic thermal loads as described in Tab. 4.3. For the static loads, the final temperature was kept constant for 48 h with relatively long rise and fall times. These tests were meant to simulate possible temperature variations in a clinical environment. The shorter rise and fall times of the dynamic or cycling tests resulted in a higher thermal load. Hence, these were aimed to accelerate possible damages induced by thermal expansion.

Table 4.3: Temperatures and profiles used in the second cycling test.

Cycle	Profile	Final temperature	Dwell time	Rise/fall time
initial	-	-	-	-
1	static	35°C	48 h	2 h
2	7 cycles	35°C	2 h	2 h
3	24 cycles	35°C	2 h	1 h
4	12 cycles	55°C	2 h	2 h
5	16 cycles	10°C	2 h	2 h
6	static	4°C	48 h	4 h
7	16 cycles	4°C	2 h	2 h
8	static	0°C	48 h	4 h
9	16 cycles	0°C	2 h	2 h

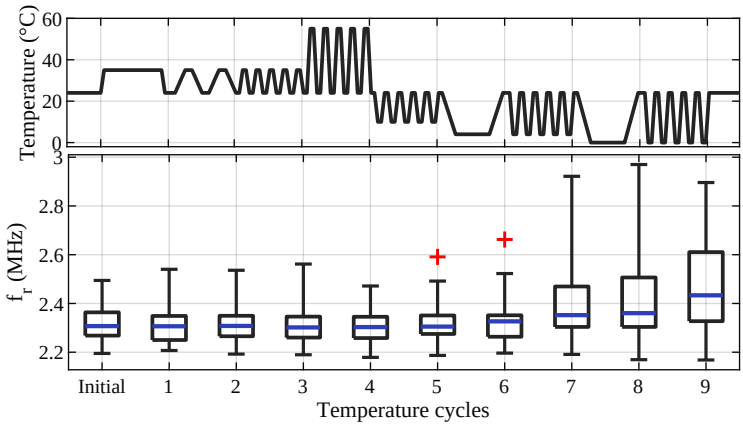

Figure 4.11: Results of second temperature cycling test. The upper graph illustrates schematically the applied temperature cycles and profiles listed in Tab. 4.3. Below, the distributions of f_r displayed as boxplots after the respective cycles are shown.

The results of the second temperature cycling test are shown in Fig. 4.11. For better illustration, the applied thermal loads are depicted schematically in the upper graph. The distribution of f_r after the respective cycle is shown below. Up to the fourth cycles, the mean remains relatively constant, with some minor changes in variability. This suggests that elevated temperatures, both static and dynamic, seem not to affect the transducers.

After the fifth cycle, a first outlier was classified, while the mean and variability exhibited minor changes. The same transducer was also classified as outlier after the sixth cycle with a slight increase in mean. Significant changes in variability are present after the seventh cycle, while only a small rise in mean was found. The distribution remained relatively constant after the eight cycle, where the temperature was lowered to 0°C. After the final or ninth cycle, a further increase in mean and variability was measured.

Based on the measured distributions of f_r, temperatures lower than room temperature seem to cause the damage. Static and dynamic loads down to 10°C have only minor effects. In addition, slow gradients down to 4°C might also be

feasible. Most damage occurs when repeated cooling down to 4°C and 0°C is present. This should therefore be avoided. The findings allow for the definition of a preliminary operation range of $10°C < T < 55°C$. This must be taken into account not only during operation, but also for shipping and storage.

The conducted temperature cycling tests are by no means sufficient to make a statement about the reliability of the TAS III design. To be able to draw reliable conclusions, accelerated aging tests with larger sample sizes are required. However, the conducted temperature cycling tests show that the transducer arrays are sensitive to changes in temperature. First damages seem to occur when the temperature drops dynamically below 10°C, especially when the freezing point is reached. The root cause of these damages will be investigated in more detail in the following section.

4.4 Tomographic Inspection

X-ray computed tomography (micro-CT) inspections were performed to investigate the damages caused by the temperature cycling tests. The scans were conducted at the Institute for Applied Materials at KIT, using a minimum slice thickness of 10 µm. Figure 4.12a shows a 3D reconstruction of one scanned array. The bright structures in the image are the layers and materials with high X-ray absorption. These include the piezoceramic fibers, the acoustic backing, the ceramic pins and the electrically conductive structures. A magnified side view of a single transducer is shown in Fig. 4.12b. It depicts the layered structure of the array design with the piezoceramic fiber on the top center. Several small air bubbles can be spotted in the backing, which potentially cause unwanted reflections.

The longitudinal sound speed of the acoustic backing was measured at 1467 m/s [86]. This results in a minimum wavelength of 0.29 mm at 5 MHz, according to Eq 2.14. Air bubbles smaller than this value should interact only slightly with the sound wave and therefore result in minor reflections. The analysis of the four scans showed that the diameter of most bubbles are below this threshold.

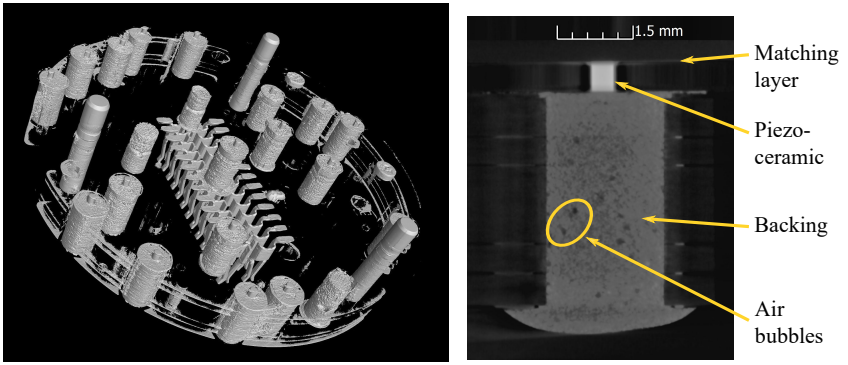

(a) 3D reconstruction of micro-CT scan.

(b) Single transducer with indicated components and smaller air bubbles found in the acoustic backing.

Figure 4.12: 3D micro-CT scan of a finalized TAS III array (a), with magnified side view of a single transducer (b).

However, for further improvements, longer degassing and lower air pressures used for dispensing the acoustic backing should be applied.

Four arrays were scanned, three of which underwent the temperature cycling tests and one of which was undamaged to serve as reference. After optimization of contrast and magnification, gaps were found in vicinity of the V_{in} electrode in some of the transducers which underwent temperature cycling. Figure 4.13 shows one of these gaps in three different views. In the top view, a ring segment which appears to be a delamination off the material is visible. This effect is also visible in the front and side view. The ring segment likely corresponds to displaced acoustic backing. Thermal expansion of this material causes shear forces on the V_{in} electrode, which could result in cracks. In terms of electric impedance, a crack in the power supply line would be equivalent to adding a small capacitor in series. The resulting total capacitance of the transducer is then dominated by the smaller capacitor, leading to a higher overall impedance. This higher resistance limits the driving current, leading in effect to a reduction in the input power which corresponds well with the measured effects.

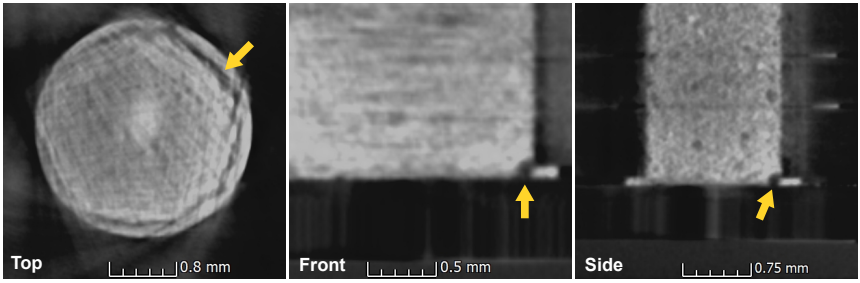

Figure 4.13: Detected gaps visible in the top, front and side view (yellow arrow) of one TAS III array after temperature cycling. These gaps could correspond to cracks in the power supply line.

It is difficult to determine from the images with certainty, whether the discovered gaps were the cause of the transducer damage. However, since they occurred after temperature cycling, breakages due to thermal expansion are likely. In particular, the metal-polymer composite of the acoustic backing differs in its thermal expansion from the surrounding polymers, resulting in mechanical stress. The relatively low adhesion of the electrode on the composite found for some of the composite disks (see Section 3.4.2) might promote this effect, highlighting the need for further improvements.

Another possibility that can cause damages is absorbed water or inclusions of humid air. Most damages occurred after dynamic cycling down to 4°, where water is at its highest density. Shrinkage of absorbed or stored water causes mechanical stress in the assembly, especially if diffusion times are short. Longer drying of the components before the assembly might aid in this regard to reduce water absorption.

To summarize, the conducted micro-CT scans allow for a general evaluation of the assembly and give hints in finding damages induced by thermal stress. Further investigations are required to rule out or confirm the possibilities stated above and ultimately find the root cause of the damages. However, with the identified operational temperature range clinical tests are feasible.

4.5 Summary and Discussion

Quality control measures were applied to test the functionality and safety of the manufactured arrays. A method for classifying transducers in groups of "pass" and "fail" was developed based on easy-to-perform electrical impedance measurements. The basic idea of the method is to find characteristics which exhibit a small overlapping area of estimated probability density functions from distinct manufacturing states. An analysis showed that the bandwidth of the electric input power is the most specific property, with a probability of 0.6% for false negative decisions. When classifying the produced arrays, 96.4% of the transducers passed evaluation. This proves the developed production process well-suited to realize functional TAS III. The method is also applicable to other sensors and systems as long as measurable properties change during production.

Temperature cycling tests were performed to get a first estimation of reliability. Two test series showed that there is a possibility of damage in case the temperature falls below 4°C with high gradients. Micro-CT inspections did not lead to conclusive findings, but suggest a weakness in the electric connection of the transducers. A safe operational temperature range from 10°C to 55°C was identified to prevent damages. For future designs, a higher adhesion of the printed electrodes was realized by changing the electrode material and careful surface preparation. Additional features such as larger recesses or electrical connection from the top should be foreseen to mitigate the effects of temperature gradients on the TAS III design.

5 Performance Characteristics

In this chapter, the ultrasound performance of the TAS III is characterized. Several different measurements were performed to determine the functional ultrasound characteristics from Tab 3.1. A measurement setup and signal processing chain is presented to measure the frequency response and directivity in 3D and 2D with high signal-to-noise ratio (SNR). In addition, a method is proposed to reconstruct the frequency- and angle-dependent phase behavior of a transducer.

5.1 Measurement Setup

The TAS III transducers have to be characterized over a large range of emission angles and frequencies in water. The utilized setup to measure the 3D ultrasound performance is shown in Fig. 5.1a. It consists of a water tank, a holder for mounting the arrays, a needle hydrophone and several measurement instruments (see below). The hydrophone (HNC-0400, Onda Corp, Sunnyvale, USA) is positioned on a motor-driven XYZ axis. A variety of different transducers can be mounted on an immersible holder, enabling the exchange of the DUT without sinking the water. The system is controlled via a graphical user interface (GUI). There, automated routines can be defined to measure the generated acoustic field at arbitrary positions. To measure the directivity and frequency response, the hydrophone was positioned with suitable resolution on a circular segment with radius r and segment angle Γ, shown in Fig. 5.1b.

Different measurement procedures can be selected in the GUI by adjusting the trajectory of the hydrophone, the excitation signal and preprocessing algorithms.

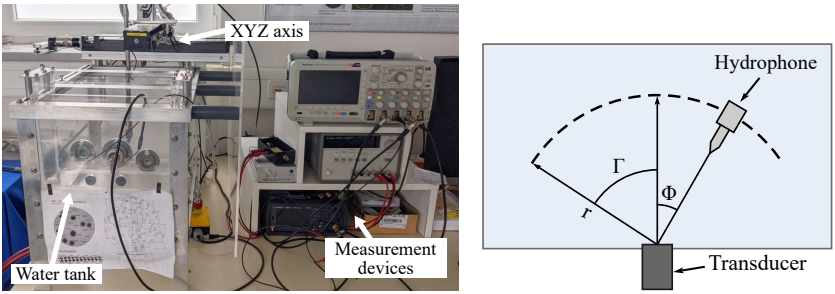

(a) Ultrasound test setup for characterization.

(b) Schema of a circular segment measurement with radius r_c, maximum angle Γ and current hydrophone angle position Φ.

Figure 5.1: Setup for transducer characterization in 3D (a) to measure the frequency response and the directivity over a circular segment (b).

A block diagram of the setup and the utilized devices is shown in Fig. 5.2. To generate excitation signals up to 20 V peak-to-peak, an arbitrary waveform generator (AWG) (33500B, Keysight, Santa Rosa, USA) is used. The signal received by the hydrophone is amplified in two stages. At first, a 20 dB preamplifier (AG-2010, Onda Corp, Sunnyvale, USA) is utilized. The resulting signal is further amplified using a custom-made setup. This setup is based on the LT6233-10 operational amplifier and exhibits 30 dB voltage amplification up to a designed cutoff frequency of 6.4 MHz at a noise voltage of 1.9 nV/$\sqrt{\text{Hz}}$ [103]. The two-stage amplification ensures high signal levels for transducers which emit low sound pressures (e.g. below 1 kPa). The signal is digitized with a scope card (PicoScope 2205A, Pico Technology, Cambridgeshire, UK) and exported as data file for further processing [104].

5.1.1 Signal Processing

Signals generated by ultrasound transducers for medical imaging are often challenging to analyze. These challenges arise from a limited sound pressure output, signal interference and complex sound propagation. For instance, when measuring the impulse response of a single transducer at larger distances, very low SNRs

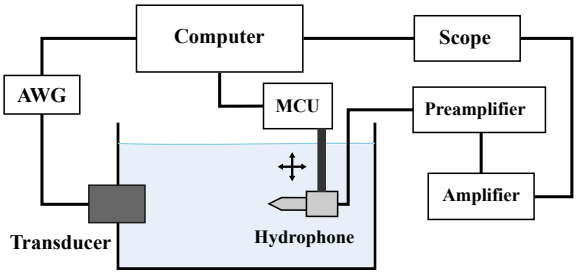

Figure 5.2: Block diagram of the ultrasound measurement setup.

can be observed. This is caused by the limited energy conveyed in the emitted pulse and the angular distribution of the sound pressure.

Coded excitation techniques can be applied to significantly increase the useful signal [105]. For decoding the signal, a matched filter is often used since this type of filter maximizes the achievable SNR [106]. In essence, a matched filter can be seen as an autocorrelation with subsequent normalization, assuming stationary white noise in the signal [107, ch. 6.2]. The more frequency components the signal contains, the higher the compression of the filtered signal. This leads to an approximated impulse response.

Chirps are a suitable option for the encoding signal since they distribute high signal energy over a wide frequency range [108]. However, the envelope of a pulse has to be smoothed to reduce ringing artifacts (Gibbs phenomenon [107, ch. 3.2]). These artifacts arise from the limited bandwidth of the transducer, the hydrophone and the measurement setup. Gaussian windows are often used due to their reciprocity in the time and frequency domain. An excitation signal which implements these considerations is given in Eq. 5.1. This signal represents a weighted linear chirp pulse, where w_n is the window function, T the length of the pulse, A the amplitude, φ_0 the phase shift and f_0 and f_1 the start and stop frequencies. An example of a Gaussian-weighted excitation chirp with $f_0 = 0.5$ MHz and $f_1 = 3.5$ MHz is shown in Fig. 5.3a.

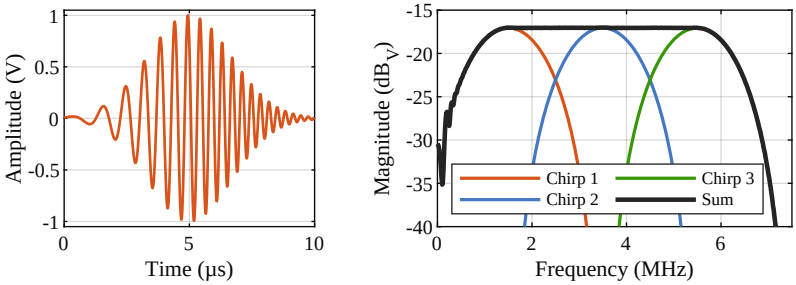

(a) Example of a Gaussian-weighted excitation chirp.

(b) Three Gaussian-weighted chirp pulses and the resulting total excitation.

Figure 5.3: Excitation signal for transducer characterization: Multiple Gaussian-weighted chirps (a) can be combined to obtain an approximately uniform excitation over a large frequency range (b).

$$y(t) = w_n(t) \cdot A \sin(2\pi(\frac{c}{2}t^2 + f_0 t) + \varphi_0) \quad \text{with} \quad c = \frac{f_1 - f_0}{T} \tag{5.1}$$

In order to cover a wide range of frequencies, long pulses are beneficial to convey sufficient energy in each frequency bin. However, long pulses might lead to challenges in separating transmission and reflection signals, even when pulse compression techniques are applied. As countermeasure, multiple shorter pulses with varying frequency ranges can be used. The respective responses are then superimposed to obtain the response over a large frequency range. Three Gaussian-weighted chirp pulses with a bandwidth of 2 MHz and a frequency shift of 2 MHz were used to cover the frequency range of 3D USCT ($0.5\ \text{MHz} < f < 5\ \text{MHz}$). The superposition of these pulses results in an approximately linear excitation over this frequency range, emphasized in Fig. 5.3b. The signal fluctuations below 0.5 MHz result from limitations of the measurement setup to generate low frequency chirps. Since these occur below the frequency range of interest, they do not interfere with transducer characterization.

Time windowing of the measured ultrasound signal is another crucial signal processing step to obtain accurate results. This is necessary for separating the

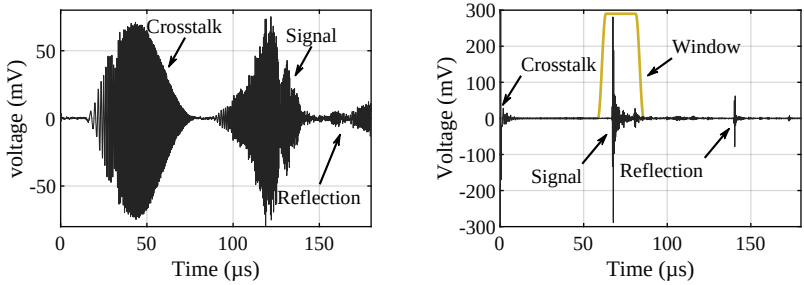

(a) Measurement of an emitted Gaussian-weighted chirp including crosstalk, transmission signal (showing transducer properties) and reflections.

(b) Signal after matched filtering and a Tukey-window to cut out the data.

Figure 5.4: Illustration of matched filtering and time windowing on an exemplary measurement signal.

useful signal from interference. An exemplary measurement of a single Gaussian-weighted chirp signal is shown in Fig. 5.4a. Prominent crosstalk and reflections are present besides the useful signal. The signal shape reflects the transducer characteristics and therefore differs from the original pulse shape. Matched filtering causes a significant compression of the signal and simplifies separation. This allows for the application of short time windows to calculate the (complex) frequency response of the transducer. The compressed signal and an exemplary Tukey window function [107, ch. 4.2] to cut out the useful signal are displayed in Fig. 5.4b.

High SNRs can be achieved by the superposition of multiple excitation pulses and matched filtering. Further improvements are possible by averaging and bandpass filtering. In Fig. 5.5 the applied signal processing chain is shown. It is used to determine the transducer sensitivity $S(\Phi, f)$ (emitted sound pressure per 1 V excitation voltage) at the measured position in the water tank. At first, each measured pulse is averaged and bandpass filtered. Then, the signals are matched filtered and cut with a time window. The fast Fourier transform (FFT) is calculated from the applied time windows and subsequently summed. This synthesizes the broadband frequency response of the tested transducer. After the synthesis, the complex frequency response is separated into amplitude and phase angle for further processing.

In order to obtain the sensitivity in the unit Pa/V, further normalization is required. This comprises the compensation of the hydrophone's sensitivity and directivity, the frequency response of the used amplifiers, the behavior of the synthesized broadband excitation signal and a phase filter. The phase filter compensates for the time of flight of the acoustic wave and enables the estimation of transducer-specific phase angles. A detailed discussion on this topic is given in the following section. In the final signal processing step, a bandpass filter is applied to suppress all signals outside the frequency range of interest. An ideal impulse response of the transducer can finally be derived when applying the inverse FFT on $S(\Phi, f)$.

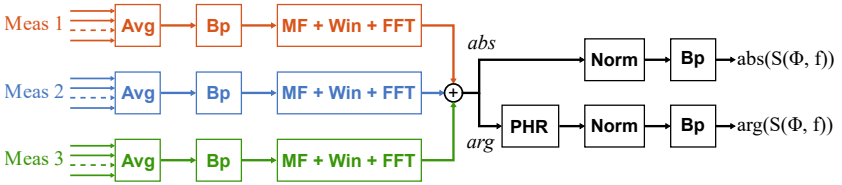

Figure 5.5: Signal processing chain to obtain the complex frequency response of a transducer with high SNR. In the presented case, three measurements (Meas 1-3) are superimposed to synthesize the broadband response. The abbreviations are: time signal averaging (Avg), bandpass filtering (Bp), matched filtering (MF), time windowing (Win), fast Fourier transform (FFT), phase angle reconstruction (PHR), and frequency response normalization (Norm).

5.1.2 Phase Angle Reconstruction

Knowing the frequency-dependent phase angle of a transducer offers several advantages when it comes to image reconstruction. First and foremost, it significantly improves pulse compression using a matched filter. This enhances the contrast in SAFT-based imaging [109]. Another advantage is the facilitation of advanced image reconstruction techniques such as waveform inversion or the paraxial approximation. Both of these require accurate performance estimations of the utilized transducers [110].

Similar to the amplitude, the phase angle of a measured ultrasound signal is the sum of the transducer characteristics, the excitation signal, the used amplifiers

and the hydrophone. Furthermore, the distance between the transducer and the hydrophone is encoded in the phase angle, which in itself depends on the respective frequency. Isolating the transducer characteristics from these effects requires several corrections and assumptions. The phase angle characteristics of the excitation signal is already compensated when using the matched filter. The phase response of the hydrophone and the applied amplifiers, if known, can be easily removed by simple phase subtraction. However, compensating phase shifts induced by the distance between the transducer and the hydrophone is more challenging, since manufacturing tolerances, positioning tolerances of the hydrophone and positioning errors between the transducer and the hydrophone are reflected in the measurement.

An example of a measured phase shifts is visualized in Fig. 5.6. It shows the impulse response magnitude of an exemplary TAS III transducer measured over a circular segment of -60° to 60° at 10 cm distance. In an ideal measurement setup, the displayed wave would be perfectly horizontal, with an uniform time of flight t_r for all angles. However, the measurement shows an additional angle-dependent delay $t_d(\Phi)$. This delay arises primarily from positioning errors between the center of the emitting transducer and the hydrophone. Analysis on multiple measurements showed that the delay varies up to several microseconds. Thus, an adaptive compensation procedure is required.

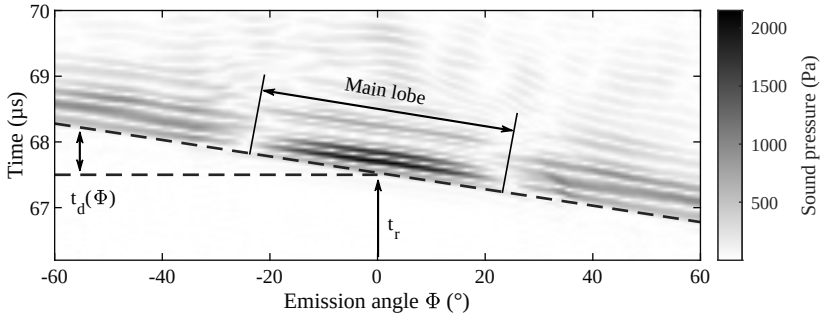

Figure 5.6: Impulse response magnitude of an exemplary transducer measured over a 120° circular segment at 10 cm distance with characteristic time delays caused by the measurement setup.

The basic idea of compensating for t_r and $t_d(\Phi)$ is to apply a phase filter which tilts the wave towards uniform propagation. However, the inherent transducer behavior such as the phase shift between the main and the side lobes must be preserved. A suitable phase filter can be obtained by generating an artificial, idealized wave mimicking the propagation of the measured wave. The phase angle of this idealized wave is then conjugated to obtain an angle-dependent filter for compensation.

A sum of discrete delta pulses is used to generate the artificial wave $\delta(\Phi, t)$. In the frequency domain, a delta pulse exhibits an uniform amplitude while the phase angle depends on the time of flight between the emitter and the receiver. This effect is illustrated in Fig. 5.7, where three delta pulses at different time of flights and the corresponding phase responses are shown. After unwrapping (suppressing 2π phase jumps), the phase angle exhibits a linear behavior where the slope of the line reflects the respective time of flight.

Matching the time of flight of $\delta(\Phi, t)$ to the measured ultrasound wave gives the desired angle-dependent phase filter. By subtracting the filter from the measured wave in the frequency domain, $t_r + t_d(\Phi)$ is shifted to zero. In mathematical terms, the phase filter acts according to Eq. 5.2. There, $S_m(\Phi, f)$ is the Fourier transform of the measured ultrasound wave, $\Delta(\Phi, f)$ is the Fourier transform of $\delta(\Phi, t)$ and $s_t(\Phi, t)$ the corrected ultrasound wave in the time domain.

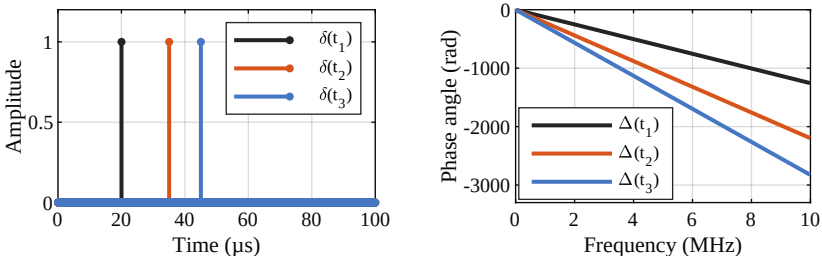

(a) Three time-discrete delta pulses in the time domain with padded zeros.

(b) Phase angle of the three delta pulses in the frequency domain.

Figure 5.7: Three delta functions at distinct times of flight in the time domain (a) and the corresponding phase angle in the frequency domain (b).

$$s_t(\Phi, t) = \mathrm{iFFT}\Big(\sum_{\Phi=-\Gamma}^{\Gamma} \sum_{f=1}^{n} |S_m(\Phi, f)| \cdot e^{-j(\arg(S_m(\Phi,f)) - \arg(\Delta(\Phi,f)))} \Big) \quad (5.2)$$

For practical implementation, t_r and $t_d(\Phi)$ have to be derived from the measured wave. This is achieved by a simple maximum search, provided that a suitable pulse response is present. In Fig. 5.8, the results of the maximum search for the measured wave from Fig. 5.6 are shown. The two steps at Φ_1 and Φ_2 mark the transition from the main lobe to the first side lobes and must not be compensated.

A third-order polynomial function is fitted to the detected maxima to obtain a wave without discontinuities. This makes the derivation of $\delta(\Phi, t)$ more robust against detection errors introduced by the maximum search. The third-order polynomial allows for accurate compensation of phase shifts from all encountered position errors. However, polynomials of third order tend to diverge with increasing distance from the region of fit. Hence, for the angles laterally exceeding Φ_1 and Φ_2, a first-order polynomial was used. This leads to a linear prolongation of the main lobe curve in both directions. The resulting idealized wave for the given example is shown in Fig. 5.8.

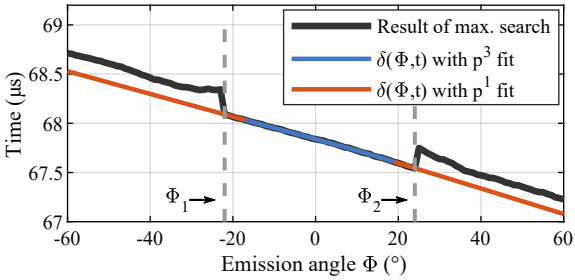

Figure 5.8: Detected maximum amplitude of a measured ultrasound wave and a fitted idealized wave $\delta(\Phi, t)$ used for phase filtering. The fit is divided into a third-order polynomial for the main lobe (between Φ_1 and Φ_2) and a first-order polynomial for the side lobes, emphasized with different colors.

Linear prolongation of $\delta(\Phi, t)$ leads to an underestimation of the respective angular ranges and thus, to errors in phase reconstruction. However, analysis of different measurements when varying the order of the polynomials proved the presented approach well suited for deriving the phase filter. Further improvements might be achievable by fitting $\delta(\Phi, t)$ to each side lobe individually. There, special caution is necessary to avoid overfitting and discontinuities in vicinity of Φ_1 and Φ_2. For 3D USCT transducers, the characteristics of the main lobe are of most interest. Therefore, additional optimization for the side lobes is not required.

Applying the phase filter to the measurement from Fig. 5.6 results in the corrected wave shown in Fig. 5.9. As intended, the phase filter leads to a horizontal alignment of the wave and a shift of the main lobe to $t = 0s$. Applying the FFT on this wave gives the angle-dependent frequency response of a transducer with its characteristic phase-angles at the origin. The presented phase correction method can also be used in reverse to generate a projection of the wave at arbitrary distances.

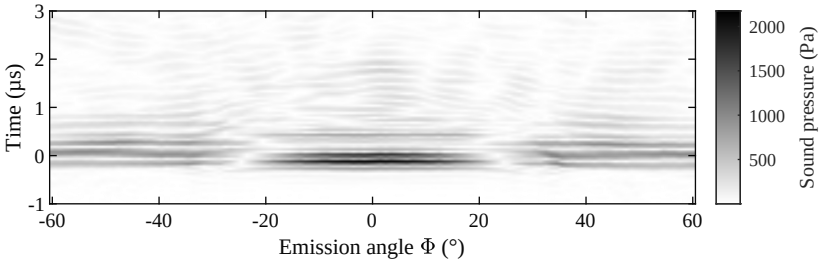

Figure 5.9: Measured ultrasound wave from Fig. 5.6 after applying the phase angle correction method.

5.2 3D Ultrasound Performance

For comprehensive analysis of the acoustic field generated by single TAS III transducers, several 3D measurements were conducted. A spherical segment of 120° x 120° at a radius of 5 cm and an angular resolution of 1° was sampled. This resulted in 14641 distinct hydrophone positions and measurement times exceeding 24 hours. Analysis of the test results showed a sound pressure field which approximates the diffraction pattern of a circular aperture. The main lobe ranged from approx. -25° to 25°, with a defined maximum at the center. All performed measurements yielded similar results, suggesting that the design meets the requirement of isotropic ultrasound emission in all spatial dimensions. However, the uniformity of the measured sound pressure varied with frequency, shown by the two examples in Fig. 5.10. Low to intermediate frequencies (0.5 to 3 MHz) exhibited prominent sensitivity fluctuations and pronounced side lobes. For higher frequencies (>3 MHz), the pressure fields became more uniform and showed multiple smaller side lobes.

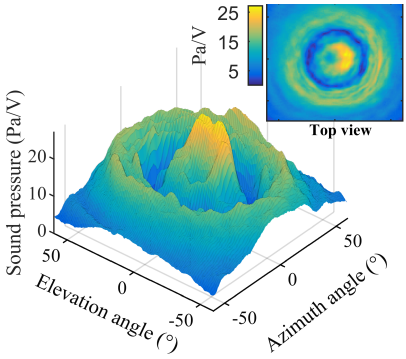

(a) Emitted sound pressure field over angles at 2.5 MHz.

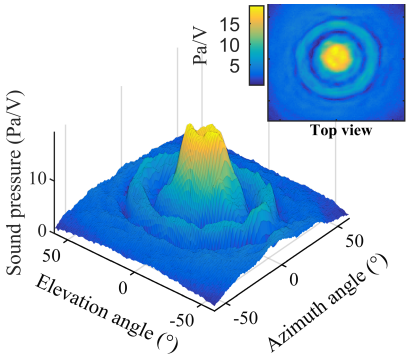

(b) Emitted sound pressure field over angles at 4.3 MHz.

Figure 5.10: 3D ultrasound performance of a single TAS III transducer at two distinct frequencies, sampled over a spherical segment of 120° x 120° at 5 cm distance with 1° resolution.

The 3D measurements enable accurate characterization of the generated acoustic field, but are too time-consuming for statistical analysis of larger numbers of transducers. By significantly reducing the measurement points, a substantial reduction in measurement time can be achieved. Hence, a circular segment at zero elevation was chosen to analyze the transducer characteristics statistically. Since the sound pressure field is approximately isotropic, these results are also valid in the azimuth direction.

5.3 Functional Ultrasound Characteristics

This section gives a quantitative analysis on the ultrasound performance of the TAS III. In order to obtain the functional characteristics listed in Tab. 3.1, three TAS III were tested. This corresponds to a total number of 54 transducers. The emitted sound pressure was sampled over a circular segment of 120° in azimuth direction at 0° elevation angle with a resolution of 1°. A measurement distance of 10 cm was chosen to obtain the performance in the far field. An exemplary measurement result is given in Fig. 5.11. There, the two images show the frequency- and angle-dependent ultrasound pressure (FASP) amplitude and phase angle generated by a transducer at 10 cm distance. All required functional ultrasound characteristics can be derived from these measurements, making FASP measurements the basis for future comparisons.

The FASP amplitude in Fig. 5.11a shows prominently the main lobe around the center angle and the first side lobes on the left and right. The highest measured pressure is in the range of 2 to 3 MHz. In addition, considerable sound emission occurs from 0.7 MHz up to 5.5 MHz, though mostly within the main lobe. The sound pressure emitted in the side lobes decreases strongly for frequencies exceeding 3 MHz. Sensitivity fluctuations, already seen in the 3D measurements (see Fig 5.10), were found in most measurements, most prominently in the region of maximal sound pressure and lower frequencies. These effects will be further discussed in Section 5.4, and studied in detail in Chapter 7.

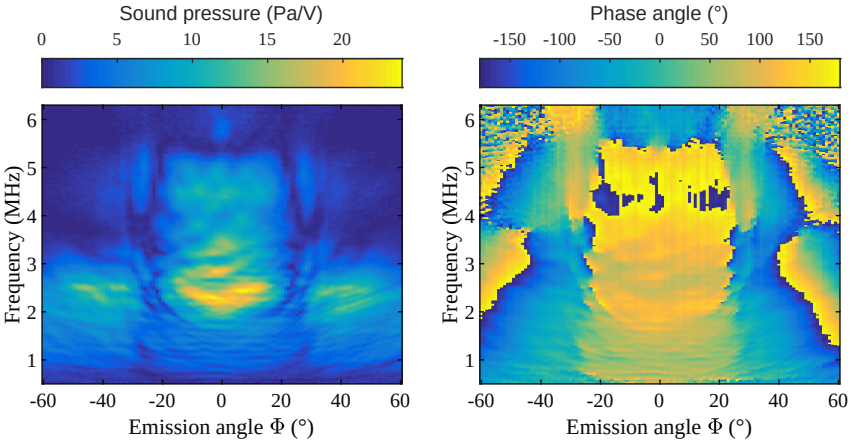

(a) FASP amplitude $|S_t(\Phi, f)|$ at 10 cm distance.

(b) FASP phase angle $\arg(S_t(\Phi, f))$ at the origin ($t_r = 0$).

Figure 5.11: Ultrasound amplitude (a) and phase angle (b) of a single TAS III transducer sampled over a circular segment of 120°.

The reconstructed FASP phase angle in Fig. 5.11b corresponds to the phase angle of the emitted ultrasound at its origin (or zero distance). It reflects the transducer's emission behavior and can be extrapolated to arbitrary distances as described in Section 5.1.2. Similar to the FASP amplitude, the main lobe is prominently present, with a gradual rise over frequency. For emission angles exceeding 40° on both ends, prominent phase shifts are present. These do not reflect the actual transducer behavior but are likely caused by the limitations and inaccuracies of the phase angle reconstruction. The speckles in the upper left and right corner are phase noise and arise from the limited SNR in this frequency and angle range.

As can be seen from the FASP amplitude in Fig. 5.11a, the usable frequency range or bandwidth bw_{us} depends on the measurement angle and the width of the main lobe (or opening angle) Φ_t varies with frequency. For easier comparison and evaluation, scalars of the transducer's functional characteristics are needed (ref. to Fig. 2.3). A common approach is to calculate the characteristics at a single frequency and angle, e.g. at the center frequency and zero degree. However, this

does not reflect the TAS III performance well since the sensitivity fluctuations would introduce a large variability. To get a representative transducer response, the FASP amplitude can be summed over a defined angle and frequency range. For instance, a sensitivity $S_{avg}(f)$ can be calculated according to Eq. 5.3, giving the average frequency behavior of the main lobe. From $S_{avg}(f)$, the center frequency f_c, the lower and upper frequency limits f_l and f_u and the fractional bandwidth bw_{us} can then be obtained.

$$S_{avg}(f) = \frac{1}{\max(|S_t(\Phi, f)|)} \sum_{\Phi=\Phi_l}^{\Phi_u} |S_t(\Phi, f)| \tag{5.3}$$

Similar to the sensitivity, a representative directivity can be calculated according to Eq. 5.4. This gives the normalized broadband response of the respective transducer and allows for the derivation of Φ_t.

$$D(\Phi) = \frac{1}{\max(|S_t(\Phi, f)|)} \sum_{f=f_{min}}^{f_{max}} |S_t(\Phi, f)| \tag{5.4}$$

$S_{avg}(f)$ from the tested 54 transducers is displayed in Fig. 5.12a. The mean sensitivity of the TAS III transducers is given in the bold curve, the darker gray areas depict the standard deviation and the brighter gray area reflects the total variability. All measurements were normalized by the maximum of the mean. The peak pressure can be found between 2 and 3 MHz, which corresponds to the thickness resonance of the piezoceramic fibers. An additional local maximum occurs in the 4 to 5 MHz range, reflecting the planar resonance. A more detailed analysis of the vibration behavior and the respective resonances is given in Chapter 7.

For frequencies lower than 0.5 MHz and above 5.5 MHz the pressure falls below -20 dB, thus defining the limits of operation. Noticeable is the increase in standard deviation for frequencies below 3 MHz. This effect was already observed in the 2D and 3D measurements (see Fig. 5.10a and Fig. 5.11a). Hence, it is systematic

for the design. The increase in variability at lower frequencies also leads to a higher variability in the derived ultrasound properties f_{min}, f_c, bw_{us} and S_c.

In Fig. 5.12b, $D(\Phi)$ of all tested transducers is shown. Similar to the depiction of the sensitivity, the mean directivity is displayed in bold, the standard deviation represents the darker grey area and the brighter grey area gives the total variability. The first minimum is at approx. $\pm 22°$, which corresponds to the angular range of the main lobe. The high variability in amplitude reflects the sensitivity fluctuations. However, the symmetric behavior of the mean, standard deviation and total variability allows for the derivation of a concise opening angle Φ_t.

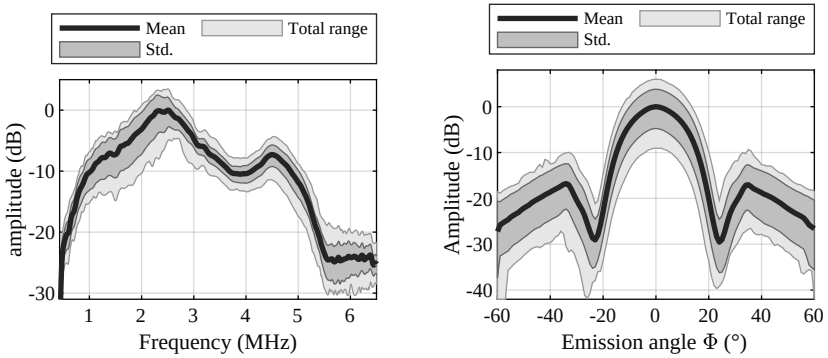

(a) Average transducer sensitivity $|S_{avg}|(f)$.

(b) Directivity $|D(\Phi)|$.

Figure 5.12: Mean, standard deviation and total variability of the transducer sensitivity (a) and directivity (b) derived from measuring 54 TAS III transducers.

The functional ultrasound characteristics from Tab. 3.1 can be derived from the average sensitivity and directivity. Figure 5.13 shows the resulting statistics. The distributions are displayed with histograms in addition to the mean and standard deviation of the sample. When testing the distributions for normality, only Φ_t exhibits an acceptable p-value. Therefore, a PDF was fitted to the data using a normal kernel function to estimate the distributions.

The arithmetic mean of the center frequency f_c is 2.55 MHz, with a mean functional -10 dB bandwidth ranging from 1.7 MHz up to 5.1 MHz. This corresponds

to a fractional bandwidth of 134.3%. The mean opening angle Φ_t is 42.8°, which sets the limits of the main lobe to ±21.4°. The center sensitivity S_c was found 18.6 Pa/V at 10 cm distance to be used for future comparisons.

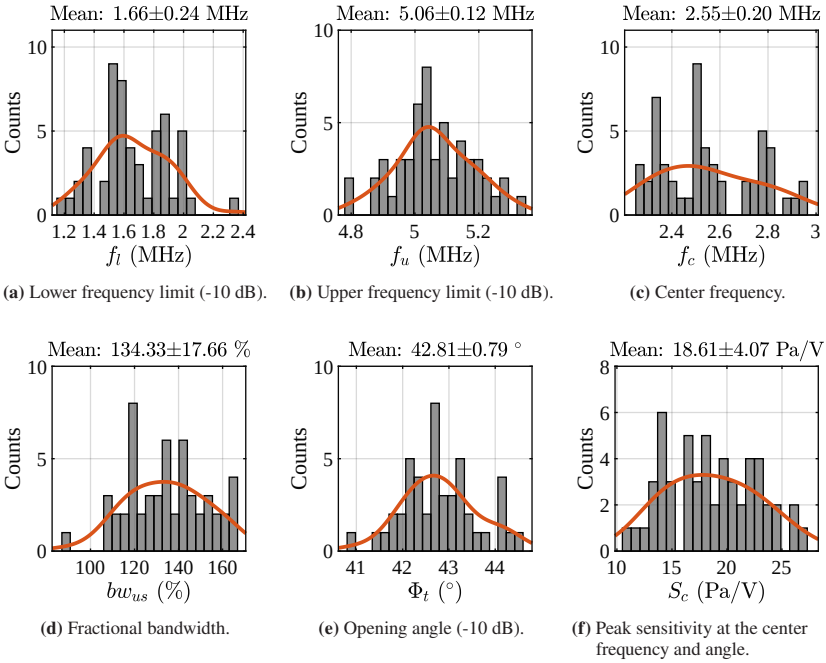

(a) Lower frequency limit (-10 dB). **(b)** Upper frequency limit (-10 dB). **(c)** Center frequency.

(d) Fractional bandwidth. **(e)** Opening angle (-10 dB). **(f)** Peak sensitivity at the center frequency and angle.

Figure 5.13: Statistics of the functional ultrasound characteristics obtained from the characterization of 54 TAS III transducers.

As presumed from the detected sensitivity fluctuations, relatively high standard deviations for f_l, f_c, bw_{us} and S_c are present. Moreover, several subgroups in the obtained distributions can be found. This limits the significance of the arithmetic mean for representing the distribution and has to be considered when comparing the results with the requirements. The origin of these subgroups are neither fabrication or dimension tolerances nor caused by the assembly since these would have a much smaller impact. A thorough time-domain analysis showed that reverberations and echoes occur after the main pulse. These were found to

be the root cause of the measured variability. This effect, the likely cause and possible improvements are investigated in more detail in Section 7.3.

5.4 Summary and Discussion

Before integrating the produced TAS III in the 3D USCT III devices, the acoustic performance of single transducers was characterized. An automated ultrasound test setup, with a hydrophone mounted on a XYZ axis in a water tank, was used to measure the acoustic field in 2D and 3D. With a developed signal processing chain, very low sound pressures (less than 10 Pa) can be measured with high SNR. A proposed post-processing algorithm allows for reconstruction of the transducer-specific phase angle. This information improves current image reconstruction techniques and is crucial for more advanced approaches in the future (e.g. the paraxial approximation).

Measuring the acoustic field of several TAS III transducer in 3D showed isotropic emission characteristics. Higher fluctuations of the emitted sound pressure for frequencies below 3 MHz were found. Statistical analysis of 54 tested transducers enabled the derivation of average characteristics. These characteristics, in comparison with the defined requirements, are listed in Tab. 5.1. Some comply well with the requirements, while others deviate considerably from the design goals. In the following, each characteristic is discussed in terms of the expected effects on the 3D USCT imaging concept. Profound design analyses and possible improvements are presented in Chapter 7.

Starting from the top of the table, f_l is more than 1 MHz higher than desired. This is surprising when looking at the average frequency response amplitude in Fig. 5.12a. There, the -10 dB limit is approx. at 1 MHz which should result in a lower f_l. This discrepancy arises from the aforementioned sensitivity fluctuations and causes multiple intersections of the -10 dB margin. Since f_l is derived from the intersection closest to f_c, sensitivities at lower frequencies still exceeding the limit are not taken into account. An example of this effect

Table 5.1: Design requirements of functional ultrasound characteristics vs. measured performance.

Functional characteristics	**Requirement**	**TAS III Transducers**
Lower frequency limit f_l	0.5 MHz	1.66 $\pm$ 0.24 MHz
Upper frequency limit f_u	5 MHz	5.06 $\pm$ 0.12 MHz
Center frequency f_c	2.5 MHz	2.55 $\pm$ 0.20 MHz
Fractional bandwidth bw_{us}	180%	134.33 $\pm$ 17.66 %
Opening angle Φ_t	60°	42.81 $\pm$ 0.79 °
Sensitivity S_c		*18.61 $\pm$ 4.07 Pa/V

*At 10 cm axial distance.

is shown in Fig. 5.14a, where the red arrow indicates two peaks that exceed the -10 dB margin below f_l. However, even when including additional peaks, a significant difference between the anticipated and required f_l remains. The impact of this deviation on algorithms for advanced transmission tomography needs to be evaluated. Adjusting the excitation pulse to boost lower frequencies could compensate the effect to some extent. But to fully comply with the specified lower frequency limit, a redesign of the transducer geometry is required. Detailed analyses of these effects and suitable countermeasures are presented in Chapter 7.

The upper frequency limit f_u matches the requirements very well. Here, the defining factor is the second resonance peak between 4 and 5 MHz. The resulting fractional bandwidth does not reach the requirement, but significantly exceeds 100%. This enables the emission of short pulses to achieve high image contrast. The mean bw_{us} exceeds most values reported in literature (see e.g. [82] and [111]) for two reasons. First, the -10 dB threshold definition in this work is very inclusive, leading to a larger range. Second, two distinct vibration modes of the piezoceramic fiber are present within the frequency range of interest. This also causes unwanted effects, discussed in more detail in Section 7.3.

The mean center frequency f_c corresponds well with the requirements, while the high variability reflects the measured sensitivity fluctuations. Nevertheless, when looking at the mean response, the maximum is well centered between 2-3 MHz.

In addition, a smaller variability can be obtained when deriving f_c from EMI measurements, supporting the validity of the measured value.

With 17.2° below the requirement, the opening angle Φ_t of the TAS III transducers does not meet expectations. Previously performed simulations and measurements of similar designs showed significantly larger Φ_t [85], making this result unexpected. The root cause of this effect and possible improvements are discussed in Section 6.1.3 and Section 7.2. A simplified representation of the impact on the 3D USCT III system is shown in Fig. 5.14b. When projecting the size of the main lobe to the center of the hemispherical measurement vessel, the radius of the ROI is limited to 6.88 cm. Thus, a single transducer can fully illuminate breasts up to 13.75 cm in diameter. The radius r_{cont} of the measurement vessel is 18 cm.

The irregular distribution of the transducers in the measurement vessel and the large number of transducers counteract the limited ROI. In addition, since not all transducer normals meet in one intersection point, larger areas are illuminated than defined by a single transducer [31].

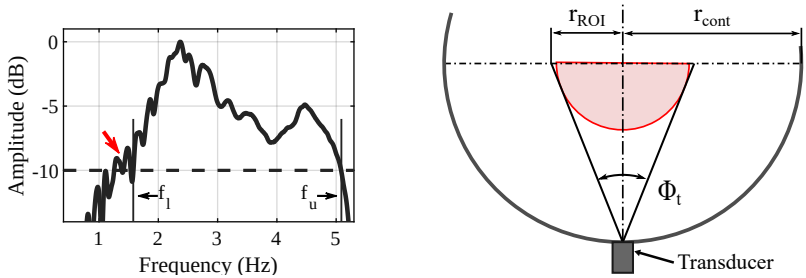

(a) Effects of sensitivity fluctuations on the derivation of f_u.

(b) ROI estimation based on the measured Φ_t.

Figure 5.14: TAS III characteristics: challenges when obtaining the bandwidth (a) and implications of Φ_t on the ROI in the 3D USCT III device (b).

No clear requirements were defined for the maximum center sensitivity S_c, since the contrast of the image results from a variety of system characteristics (see Section 2.3). Whether the achieved sensitivity is sufficient has to be evaluated in

comprehensive system tests and clinical imaging. However, the determined value enables comparison of future concepts and technologies with the current design.

6 Transducer Models for Analysis and Optimization

This chapter presents two modeling approaches used for the analysis of the TAS III design and to derive possible improvements. The first modeling approach is based on an equivalent circuit model (ECM) and used for the analysis of characteristic resonances, the influence of damping and parasitic circuit elements. In extension to that, an analytical expression is presented which enables a first estimation of the acoustic field generated by a single transducer. The second modeling approach encompasses a finite element (FE) analysis. It allows for comprehensive analyses of the vibration behavior and the generated acoustic field.

Several measured effects are investigated in later chapters using the developed models. Hence, careful validation with measurements is required since model predictions often deviate from measurements due to limitations of the chosen modeling approach, availability of material properties or inaccurate model assumptions [112]. In order to improve the prediction accuracy of both presented models, parameters were adjusted to better match the measured average characteristics. Therefore, modeling was performed after fabrication to be able to draw on extensive measurement results.

6.1 Equivalent Circuit Model

ECMs are used to approximate the performance of a transducer in a very simplified way. The mechanical properties such as stiffness or inertia are modeled using equivalent (lumped) electrical components. This enables the calculation of the

electric impedance, the transfer function, state variables (e.g. voltage and current) and the output behavior. Usually, ECMs exhibit much lower complexity than numerical methods. This enables rapid analysis and multidimensional parameter sweeps [45, 112].

A simple ECM to predict a transducer's resonance behavior is the Butterworth-van-Dyke (BVD) circuit, shown in Fig. 6.1. There, the transducer is modeled with a series RCL circuit describing the mechanical behavior, and an additional capacitor in parallel [113, 114]. The parameters of the lumped elements are either obtained from measurement [91] or by considering the dimensions and respective vibration modes [115].

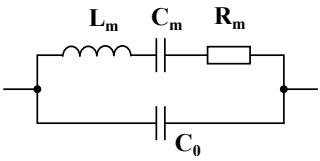

Figure 6.1: Butterworth-van-Dyke ECM to model one-dimensional resonators. The upper path (L_m, C_m and R_m) describes the mechanical behavior, C_0 is the (electrical) blocking capacitance.

The BVD model does not account for additional layers and multiple vibration modes. Since the surrounding materials have a strong impact on the vibration behavior, more accurate modeling approaches are commonly utilized. The KLM model, named after Krimholtz, Leedom and Matthaei who first published it in 1970 [116], allows for the consideration of additional layers connected to the front and rear of a piezoceramic material. The layers are added to the secondary side of a transformer circuit via transmission lines. By using transmission lines, wave propagation effects in the connected layers can be modeled. Hence, it enables a better representation of a transducer while still having the benefit of low complexity.

For this work, an extended version of the KLM model was developed. The general modeling approach is published in [2], where it was applied to analyze the performance of the TAS IIb. In [3], the model was enhanced to cover a

second vibration mode for better representation of the TAS III design. The following sections present a slightly adjusted version of the enhanced model, henceforth referred to as 2D KLM model, to be used for design analysis and future improvements.

6.1.1 2D KLM Model

In the KLM model, the EM conversion is realized with a transformer coupled to the center of a transmission line. Additional layers on the front and rear can be considered by adding transmission lines with acoustic impedance Z, thickness h and complex propagation constant $\gamma = \beta(\alpha + j)$. In the original model, only one spatial dimension and the respective vibration resonance was considered.

As observed in the sensitivity characterization of the TAS III in Section 5.3, a second prominent resonance peak is present in the examined frequency band. This second peak corresponds to the planar resonance of the piezoceramic fiber. By adding a transformer circuit in series, the KLM circuit is able to cover a second dimension [117]. This results in an equivalent circuit model which represents two distinct vibration modes. The resulting circuit diagram is shown in Fig. 6.2. It is important to emphasize that each spatial dimension is implemented as coupled 1D transmission line. Hence, geometries which deviate from a rectangular cross section can not be modeled adequately. Therefore, the model corresponds to a 2D shell structure rather than an actual 2D resonator.

A detailed description of the calculation scheme and the governing equations to set the 2D KLM model is given in Appendix A.1. Below, only a brief explanation is provided. The EM conversion for each vibration mode is realized with a transformer with turns ratio Ψ. The secondary sides are coupled to the centers of transmission lines with either the radius r or half the thickness $h_0/2$ of the piezoceramic fiber.

The blocking capacitance is given by C_0, while C'_{31} and C'_{33} are frequency-dependent reactances. The transmission line of the planar mode is terminated

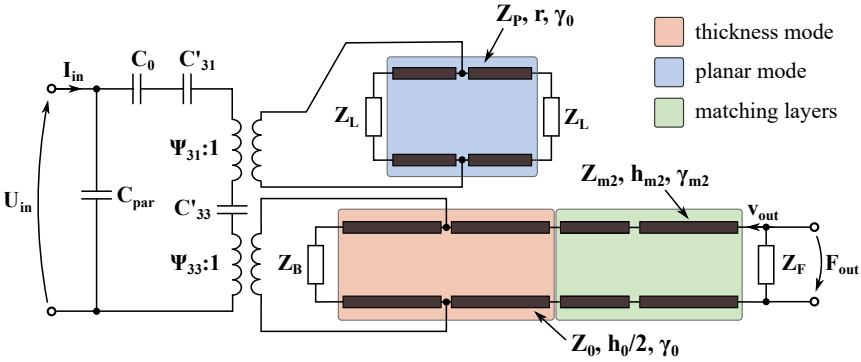

Figure 6.2: ECM of a transducer which considers two spatial dimensions and two matching layers on the front. The model is based on the KLM equivalent circuit.

with the acoustic impedance of the filler material Z_L. The impedance of the acoustic backing Z_B terminates one end of the thickness mode transmission line. On the front side of the transducer, the two additional transmission lines correspond to two matching layers.

In order to describe the vibration behavior better, losses are taken into account. Two different loss mechanisms of the piezoceramic material are considered. First, dielectric losses are added with the loss tangent $\tan(\delta)$ to C_0 [118]. Second, mechanical losses enter the circuit by defining the attenuation factor α for the propagation constant γ_p [119]. The same approach is used to include acoustic attenuation of the matching layers and lateral damping.

The 2-port scheme presented in [120] is applied to simplify calculations. It represents the circuit with a series of 2x2 transmission matrices. These matrices enable direct concatenation to retrieve a single 2-port, given in Eq. 6.1. This 2-port directly relates the input with the output variables.

$$\begin{bmatrix} U_{in} \\ I_{in} \end{bmatrix} = \begin{bmatrix} A(\omega) & B(\omega) \\ C(\omega) & D(\omega) \end{bmatrix} \begin{bmatrix} F_{out} \\ -v_{out} \end{bmatrix} \tag{6.1}$$

For ultrasound emission and reception, the 2-port model is terminated on both ends as shown in Fig. 6.3. At the input, a voltage source U_S with series impedance Z_S is connected. The output is terminated by the impedance Z_F which corresponds to the acoustic impedance of the front medium. With these boundary conditions, the input impedance and transfer function can be derived.

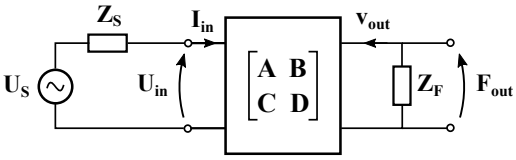

Figure 6.3: 2D KLM model reduced to a 2-port and terminated on both ends.

With the boundary condition stated in Eq. 6.2, the 2-port is collapsed to the expression given in Eq. 6.3. The resulting response simulates the transducer's EMI and enables direct comparison with measurements.

$$F_{out} = -Z_F A_0 v_{out} \tag{6.2}$$

$$Z_{in}(\omega) = \frac{U_{in}}{I_{in}} = \frac{A(\omega) Z_F A_0 + B(\omega)}{C(\omega) Z_F A_0 + D(\omega)} \tag{6.3}$$

The circuit's transfer function gives the frequency-dependent conversion of the source voltage into a radiated acoustic force. In order to derive it from the 2-port model, the boundary condition in Eq. 6.2 is substituted into Eq. 6.1. The supply voltage U_S is related to the input voltage of the 2-port according to Eq. 6.4 using Kirchhoff's second law [121, ch. 7].

$$U_S = U_{in} - I_{in} Z_S \tag{6.4}$$

Equation 6.4 can then be substituted into Eq. 6.1, yielding after some simplifications the transfer function stated in Eq. 6.5.

$$H(\omega) = \frac{F_{out}}{U_S} = \frac{Z_F A_0}{A(\omega) Z_F A_0 + B(\omega) + C(\omega) Z_S Z_F A_0 + D(\omega) Z_S} \tag{6.5}$$

The 2D KLM model allows for analysis of the thickness and planar resonance of the TAS III transducers. As it is the case for any model, accurate predictions require valid parameters. Furthermore, the physical limits of the chosen modeling approach leads to deviations between model and measurement. In order to achieve reliable predictions, model validation and a critical analysis of the results is essential.

6.1.2 Model Fit

A previously conducted study showed that the 2D KLM model does not predict the effect of the matching layers in the TAS design [2]. Further analysis revealed that the large difference in diameter between the fiber and the matching disk causes this deviation. With the KLM modeling approach, the difference in lateral extension cannot be considered due to the 1D representation of layers via transmission lines. Hence, the 2D KLM model is best suited to predict the performance in the initial production state before attaching additional layers.

EMI measurements are used for model validation (see Section 4.2). In Fig. 6.4, the total range of 140 transducers is displayed with the gray area and a single representative measurement in the center. The dashed curve shows the model response when using the parameters of the piezoceramic fiber from the material's data sheet [122]. The parameters Z, α and v of the transmission lines are taken, where possible, from literature [123, 124]. Missing parameters are estimated. The dimensions of the piezoceramic and the matching layers are measured with a micrometer gauge.

In general, the model covers the impedance behavior with two resonances in the respective frequency range. However, a significantly higher thickness and planar

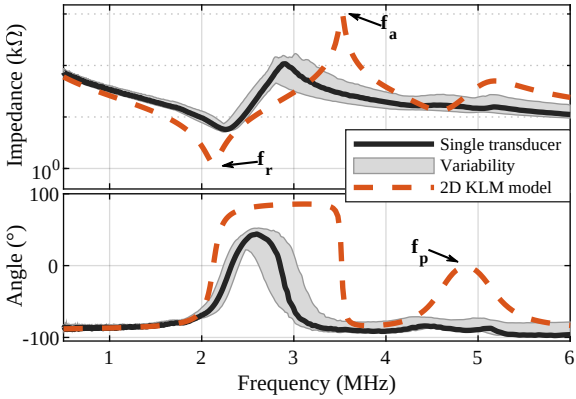

Figure 6.4: Model-to-measurement comparison of a transducer before the assembly (initial state) when using parameters from literature.

coupling is predicted. In addition, characteristic frequencies such as the resonance and anti-resonance frequencies f_r and f_a exhibit frequency shifts. In order to improve the prediction accuracy, a parameter fit was conducted. The general approach was already presented in [3], with focus on minimizing the difference in overall impedance between the model and a single measurement. A more generalized approach is to minimize the difference between the model and mean measured EMI characteristics. By this, a parameter set which reflects an average transducer can be obtained.

The three characteristic frequencies indicated in Fig. 6.4 were chosen for the fit. This limits the complexity while covering the essential behavior. These frequencies reflect the thickness mode resonator via f_r and f_a and the planar mode via f_p. The mean value of f_p was not taken from the impedance measurements, since the resonance peak is not well pronounced there. Better suited for this case are the results of the sensitivity measurements in Fig. 5.12a, since the planar resonance is prominently present there.

Four parameters have a dominant impact on the model response with respect to the characteristic frequencies. These are the mechanical compliances in thickness and planar direction s_{33}^E and s_{11}^E and the respective coupling factors k_{33} and k_{31}.

A brute force search was performed over the first three of the stated parameters. These were varied up to a maximum of ±20% from the literature values. In order to calculate the material's speed of sound via Eq. 2.12, the compliances had to be converted into a mechanical stiffness according to Eq. 2.10.

The planar coupling k_{31} was set constant since insufficient data is available for accurate comparison. The model fit was quantified according to Eq. 6.6, where f_{mod} are the characteristic frequencies derived from the model and f_{meas} are the measured counterparts. For example, for $n = 1$, f_{mod} and f_{meas} are replaced with f_r.

$$\delta_{fit} = \sqrt{\sum_{n=1}^{3} \left(1 - \frac{f_{mod}(n)}{f_{meas}(n)}\right)^2} \tag{6.6}$$

The best fit parameter set was obtained by minimizing δ_{fit} over all parameter combinations. As a safety measure, a factor of 1 was added in case δ_{fit} exceeds 10% deviation for a single characteristic frequency. This ensures that all characteristics remain within ±10% deviation from the target value. In Fig. 6.5a, δ_{fit} is shown after varying the two mechanical compliances, while k_{31} was constant. Within the investigated ranges, the blue area represents parameter combinations that lead to low differences. The minimum is indicated by the red dot, where δ_{fit} takes a value of 0.002. With this parameter set, the model predicts the transducer impedance shown in Fig. 6.5b. The corresponding parameters are listed in Tab. 6.1.

Using the best fit parameters, the modeled impedance matches the measured EMI well. The thickness mode resonance between 2-3 MHz is accurately covered, with almost no deviations in the characteristic frequencies. Furthermore, f_p agrees well with the measurements but is more pronounced in the model to enable a better analysis of the planar mode. The required parameter adjustments are listed in Tab. 6.1. These suggest that the transducers exhibit a higher compliance in thickness direction by 4.6%. In planar direction, the compliance needed reduction, suggesting a higher stiffness in the composite. For both vibration

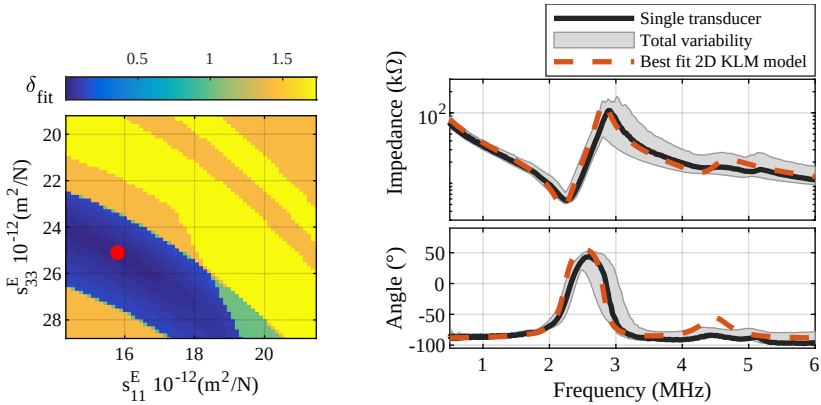

(a) Model-to-measurement fit when sweeping over the mechanical compliances. The best fit is indicated by the red dot.

(b) Model response when using the best fit parameters compared to a single measurement and the total variability of 140 transducers.

Figure 6.5: Brute-force parameter sweep (a) to obtain the model response with the best fit to measurements (b).

modes, the EM coupling is lower than stated in the data sheet. This is reasonable since these values are obtained under idealistic conditions with high separation of the vibration modes [41].

Table 6.1: Model parameters and sweep range for the brute-force search to find the best-fit parameter set of the 2D KLM model. The planar coupling k_{31} was set constant.

Model parameter	Data sheet	Range	Best fit	Adjustments
s_{33}^E $10^{-12}[m^2/N]$	24.0	19.2 - 28.8	25.1	+4.6%
s_{11}^E $10^{-12}[m^2/N]$	17.9	14.3 - 21.5	15.8	-11.7%
k_{33}	0.73	0.58 - 0.73	0.65	-11.0%
k_{31}	0.33	0.20	0.20	-39.4%

The EMI of a transducer reflects the vibration behavior resulting from the entire geometry and the surrounding structures. However, only two spatial dimensions are approximated by the 2D KLM model. In the brute force approach, this misrepresentation of the geometry is likely to cause overfitting. Still, the 2D KLM

model is a useful tool to quickly analyze the impact of changes in dimensions and materials. Multidimensional effects are better covered with FE analysis. The complete parameter set for the best fit and the (basic) literature parameters are listed in Tab. A.1.

6.1.3 Estimation of Directivity

A simple analytic expression is often helpful in getting a first impression of the directivity of a transducer [125, ch. 4]. Assuming a circular piston in free space, Eq. 6.7 gives an expression of the frequency dependent directivity in the far field [36, ch. 10]. The expression is derived from a solution of the wave equation in polar form, where the second multiplier $(1+\cos(\theta))$ leads to an improved accuracy at larger angles [126]. The frequency response of a transducer is considered by the transfer function $H(\omega)$, J_1 is the Bessel function of first order, $k = \omega/v$ the wave number and r the radius of the transducer.

$$S(\theta, \omega) = H(\omega) \cdot (1 + \cos(\theta)) \left(\frac{J_1(k \cdot r \cdot \sin(\theta)}{k \cdot r \cdot \sin(\theta)} \right) \tag{6.7}$$

Before calculating the frequency dependent directivity, some adjustments in the 2D KLM model are required. Since the transducer is in its final state and operating in water, the acoustic impedances Z_F and Z_B were increased to 1.5 MRayl and 7.3 MRayl, respectively. When substituting the resulting transfer function into Eq. 6.7, the model predicts a FASP amplitude and phase angle as shown in Fig. 6.6.

Comparing the predicted FASP with the exemplary transducer measurement in Fig. 5.11 provides several interesting insights. First, the simulated opening angle Φ_t is approximately two times larger than the measured equivalent. Within the investigated angular range, the predicted pressure field exhibits a prominent main lobe and no side lobes. Second, the simulation covers the basic behavior of the planar-mode resonance above 4 MHz, although less pronounced. This encourages the use of the 2D KLM model to predict two-dimensional effects. Third, the

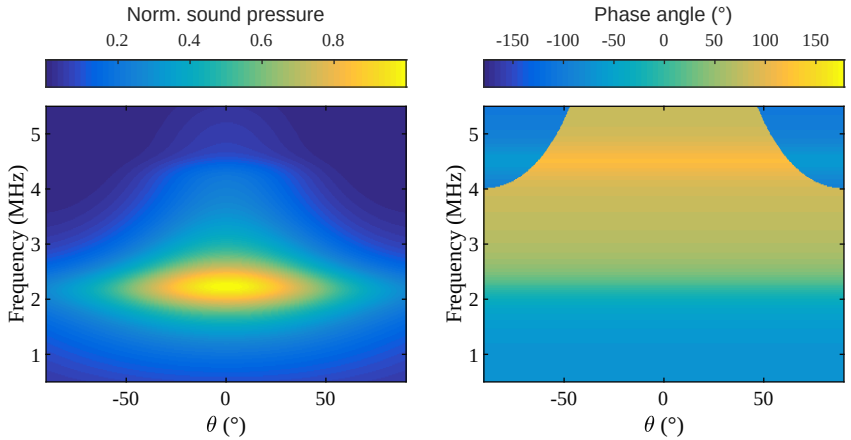

(a) Predicted FASP amplitude.

(b) Predicted FASP phase angle.

Figure 6.6: Prediction of the FASP amplitude (a) and phase angle (b) from the analytical expression in Eq. 6.7.

predicted phase angle shows a similar frequency behavior as the measurement. In both, it gradually rises until it reaches a maximum at f_p.

The reasons for the large difference in the prediction of Φ_t are manifold. Embedding the piezoceramic fiber on all sides increases the effective diameter of the emission surface. A larger surface leads to a reduction in Φ_t. Furthermore, the difference in diameter between the surface of the piezoceramic fiber and the matching layer affects the directivity. Contraction of the piezoceramic leads to an area of deformation of the matching layer larger than the fiber diameter. This, increases once more the effective emission area. Another important factor is the dimension of the transducer. The small thickness-to-diameter ratio causes mixed vibration modes, which strongly affects the emitted acoustic field. A more detailed analysis on this effect can be found in Section 7.2.

In summary, predicting the directivity of a transducer using Eq. 6.7 allows for a first estimation of the acoustic field generated by a transducer. However, if the transducer geometry deviates from the modeled assumptions (in this case piston in

free space), the prediction differs significantly from measurements. This leads to the conclusion that the stated approach is not well-suited to predict the directivity of the TAS III transducers.

6.2 Finite Element Analysis

The complex vibration behavior generated by a piezoceramic material embedded in various layers can be studied with the aid of FE analysis. This enables the prediction of the acoustic field and direct comparison with measurements. In this work, COMSOL Multiphysics (version 5.6) was used as simulation environment. This commercially available software package allows for direct coupling of the required physics. Details on the background of FE analysis for ultrasound transducers can be found in [127] and [128]. The model was set in two stages: At first, an initial model with parameters from literature was built. Next, this initial FE model was fitted to measured characteristics to improve the prediction accuracy.

6.2.1 Initial FE Model

The piezoelectric material was modeled using structural mechanic and electrostatic physics. The acoustic field was calculated in water using pressure acoustic physics. In order to obtain the functional transducer characteristics from Tab. 3.1, a frequency domain study was conducted. Since the design of a single TAS III transducer is rotationally symmetric, it can be modeled as 2D axisymmetric shell. By revolving the results of the shell simulation, the full 3D acoustic field can be obtained. This decreases the complexity of the model, leading to a significant reduction in calculation time [129].

The implemented model geometry including additional information and the defined boundary conditions is shown in Fig. 6.7. For easier reference, the colors match those in the schematic cross section in Fig. 3.6. A free-triangular mesh with a maximum side length of $\lambda_{min}/6$ was used for the water domain [130]. An

additional boundary layer with $\lambda_{min}/20$ was foreseen for accurate estimation of the far field. A perfectly matched layer (PML) was added to the water domain to avoid interference caused by reflections. The PML layer consisted of eleven regular mapped elements in radial direction. All other domains were meshed with free-triangles while adjusting the size to the respective dimensions. A low reflection boundary was set to the edges of the transducer to avoid reflections and to improve numerical stability [131].

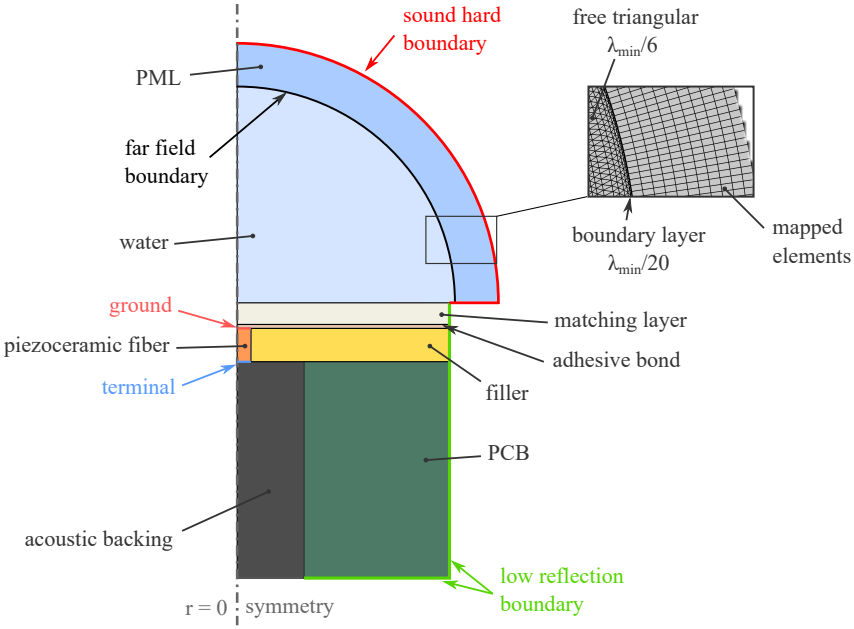

Figure 6.7: FE model implemented as 2D shell including layer definitions and boundary conditions. A magnified view of the PML domain illustrates the applied mesh. Results in 3D were obtained by revolving the design.

The piezoelectric material was defined in strain-charge form, with the constants taken from the data sheet of the basic piezoelectric material [122]. Missing constants were calculated according to the schema in Section 2.1. To ensure the correct implementation of the piezoelectric behavior, benchmark tests were

conducted. Idealized geometries as defined in [39] were used to test the anisotropic behavior in axial and shear direction. The strain after applying a voltage and the charge after applying a force were compared with the given constants to ensure correct implementation.

Linear elastic behavior was assumed for the passive materials which surround the piezoceramic (filler, matching layer etc.). This required the definition of the elastic modulus E, the density ρ and the Poisson's ratio ν of the respective material. The parameters were taken from literature, measured, determined by experiments or estimated (see Tab. A.3). Material damping and losses play a crucial role in the correct prediction of vibration amplitudes, especially at resonances. However, appropriate parameters and expressions were not found in literature. Thus, they were first estimated and refined in later stages. The material parameters as well as the piezoelectric constants are listed in Tab. A.3 and Tab. A.2, respectively.

A frequency study for $0.4 < \mathrm{f} < 6.0$ MHz with 512 linear spaced frequencies was conducted. In Fig. 6.8a, the results of this study are presented. It shows the simulated FASP amplitude evaluated over a circular segment at 10 cm axial distance. Hence, these results are directly comparable with the measurement presented in Section 5.3. The comparison shows that the overall behavior is well covered by the model. The main lobe and side lobes are prominently present, while the modeled sensitivity is slightly lower than the measured one. However, the model predicts the transducer's thickness mode to be at lower frequencies and the planar mode at higher frequencies than measured.

A quantitative comparison of the modeling results with the mean transducer characteristics is given in Tab. 6.2. The calculated difference shows that all characteristics deviate by more than 10%. The center frequency f_c is lower than measured, while the planar resonance f_p exceeds the reference. This results in a significant differences for f_l, f_u and bw_{us} (see Section 2.3 for the parameter introduction). The opening angle Φ_t, though closer than analytically obtained, is still 9.9° larger than the measured mean. The center sensitivity S_c is smaller than measured but in the same order of magnitude. These deviations indicate that the mechanical properties used for the simulation do not fully match the actual

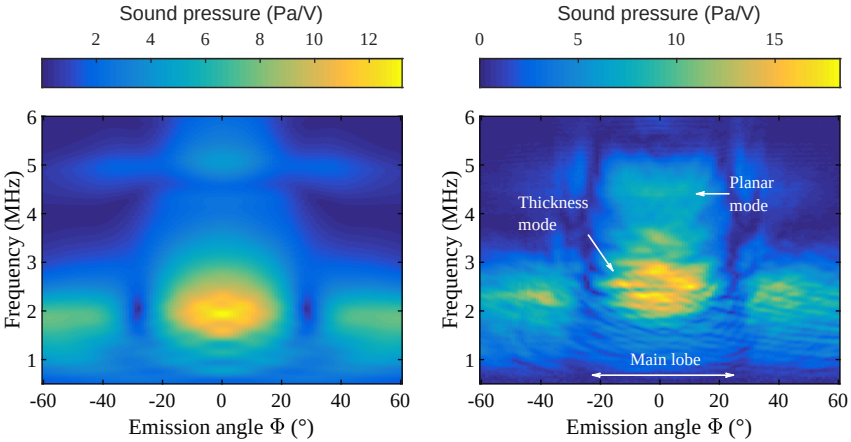

(a) Modeled FASP amplitude with the FE model

(b) Measured FASP amplitude of an exemplary transducer with additional explanations.

Figure 6.8: FE model (a) to measurement (b) comparison of the FASP amplitude over a circular segment of 120° at 10 cm axial distance.

conditions. One reason for this mismatch is the manufacturing process of the piezoceramic fiber. The developed polysulphone spinning process [78] differs from conventional PZT fabrication techniques, hence a deviation in mechanical properties can be expected. In order to achieve a better prediction accuracy, a parameter fit was conducted. Before discussing this fit in detail, a closer look on mechanical loss properties of passive materials is presented.

Table 6.2: Measured mean TAS III characteristics compared with the results from the FE model. The model parameters and piezoelectric constants were taken from literature.

	$\mathbf{f_l}$ [MHz]	$\mathbf{f_u}$ [MHz]	$\mathbf{f_c}$ [MHz]	$\mathbf{bw_{us}}$ %	$\mathbf{\Phi_t}$ [°]	$\mathbf{S_c}$ [Pa/V]	$\mathbf{f_p}$ [MHz]
Measurement	1.66	5.06	2.55	134.33	42.81	18.61	4.5
Initial FE model	0.66	3.60	1.97	150.42	52.74	13.20	5.07
Difference	-60.2%	-28.9%	-22.7%	+12.0%	+23.2%	-29.1%	+12.6%

6.2.2 Modeling of Losses in the Passive Materials

Losses can be defined as a dissipation of energy which reduces the effective power. One form of losses in transducer design is vibration damping. High damping is intended to limit the maximum strain and increase the effective bandwidth. It is usually achieved by embedding the piezoceramic in elastic materials. Another form of losses is sound attenuation. It reduces the amplitude of ultrasound waves traveling through a material. For example, the acoustic backing must exhibit high sound attenuation properties to dissipates the energy emitted to the rear.

In the presented FE model, vibration damping is controlled by the elastic properties of the materials. Accounting for sound attenuation requires the definition of additional loss properties for each material. A common approach in frequency domain analyses is the structural loss factor η_s. It introduces hysteretic losses in solids by adding a complex factor to the stiffness matrix of the material [132]. The effect of different loss factors on a transducer's performance is illustrated with the example in Fig. 6.9. There, the upper curve represents the axial frequency response amplitude of a TAS III transducer at a distance of 10 cm when η_s of the filler and the acoustic backing was set to 0.1. The lower curve results for $\eta_s = 2$.

Comparing the two curves shows that damping properties have a strong impact on the performance. A drop by almost 10 dB and shifts in the resonances are caused by the different structural loss factors. Furthermore, prominent sensitivity fluctuations are present, especially for frequencies lower than 2 MHz. In the example, the chosen values of η_s are the expected upper and lower bounds for polymers in the respective frequency range [133, ch. 4]. The actual material parameters were derived from measurement and fitted to an expression to be used in the FE analysis. The measurement setup and fitting procedure was already published in [4], hence only a summary is presented below.

In polymers, the effective losses depend strongly on the excitation frequency [134]. Dynamic Mechanic Analysis is a common procedure to directly measure η_s for different frequencies. However, this analysis requires special machinery and is usually conducted in the range of Hz to kHz [135]. An alternative way

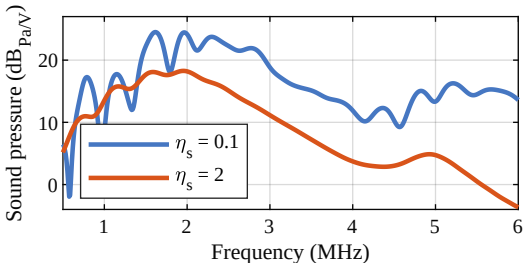

Figure 6.9: Impact of high and low structural loss factors on the modeled frequency response amplitude of a TAS III transducer.

of deriving material loss properties is an ultrasound transmission setup. There, the frequency and size dependent attenuation coefficient $\alpha(f, h)$ can be obtained by measuring the change in ultrasound transmission caused by a material. The attenuation coefficient can then be converted into an equivalent loss factor.

A measurement series was conducted to obtain $\alpha(f, h)$ for the filler and acoustic backing. Material samples with varying thicknesses were placed in between two transducers and scanned. A detailed description of the sample preparation and the measurement setup is given in [86]. After deriving $\alpha(f, h)$ from measurement, the data was fitted to an analytic expression. The resulting function allows for the prediction of attenuation at arbitrary frequencies and thicknesses.

Sound attenuation in polymers can be approximated by a frequency-power law as described in Eq. 6.8 [136, 137]. There, β models the change in loss behavior over frequency, a_0 is the attenuation at frequency f_0 and a_1 and a_2 define a linear relation between attenuation and material thickness in dB. Using this expression, an attenuation model can be tailored to match the frequency range in vicinity of f_0 best.

$$\alpha(f, h) = a_0(f/f_0)^{\beta} \quad \text{with} \quad a_0 = a_1 h + a_2 \tag{6.8}$$

Fitting a frequency-power law to the measured attenuation results in the graphs shown in Fig. 6.10. The dashed curves are the measured attenuation for three

material samples with their respective thicknesses. The bold curves give the predictions of the best-fit frequency power law model. Least-square minimization was used for the model fit. As a result, the absolute values and frequency dependence of the attenuation are well covered by frequency-power law. For the filler material, it accurately predicts the behavior of all three samples over the entire frequency range. For the acoustic backing, the two thinner samples are well predicted, while the behavior of the thickest sample deviates at higher frequencies. This deviation is caused by the limited SNR of the measurement setup and does not reflect material properties.

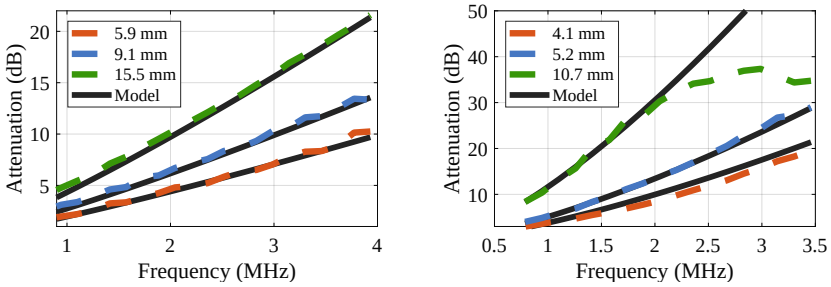

(a) Attenuation behavior of the filler material.

(b) Attenuation behavior of the acoustic backing material.

Figure 6.10: Measured and modeled acoustic attenuation for two of the passive materials used for manufacturing the TAS III.

The conversion of $\alpha(f)$ in dB/m to an equivalent loss factor $\eta_s(f)$ is based on the comparison of exponents using the analytic description of acoustic attenuation [125] and viscous losses [138]. By this, the expression in Eq. 6.9 can be derived, where v is the speed of sound of the material, L is the effective length of an approximated viscous damper [132], ρ the density and E the elastic modulus. The factor 8.7 results from the conversion from dB to Neper, a dimensionless unit describing acoustic attenuation [125, ch. 8.3]. When controlling the physical units of the conversion expression, η_s is dimensionless. This is required when modeling hysteretic losses with structural loss factors and supports the validity of the presented approach.

$$\eta_s(f) = 2vL/8.7 \cdot \alpha(f) \cdot \sqrt{\rho/E} \tag{6.9}$$

The best-fit coefficients and parameters to obtain an expression of $\eta_s(f)$ for both materials are listed in Tab. 6.3. The lengths L of the effective dampers were chosen based on the design and the resulting η_s values. These assumptions introduce a source of error in the loss conversion which must be taken into account when analyzing the results. However, the derived values are better approximations than the original estimates. Furthermore, they are within typical ranges reported in literature [139]. The final expressions used for the FE model are given in Tab. A.3.

Table 6.3: Coefficients of loss factor models based on the frequency-power law for two materials utilized for the TAS III.

	β	$\mathbf{a_0}$ [dB/m]	$\mathbf{f_0}$ [MHz]	$\mathbf{L}$ [mm]
Filler	1.17	752	2.52	1
Acoustic backing	1.39	1256	1.10	2

6.2.3 FE Model Fit

A variety of parameters can be adjusted to improve the prediction accuracy of the FE model. A brute force fit similar to the ECM fit (see Section 6.1.2) is not feasible since the larger number of model parameters would lead to excessive computation times. In order to identify parameters which minimize the differences between model and measurement, the following strategy was applied: The elastic properties of the passive materials, e.g. the acoustic backing, were derived from literature and experiments. Hence, most of these properties were kept constant. Only the modulus of the filler material E_{adh} was increased since it exhibits a strong impact on Φ_t. The fabrication process of the piezoceramic fiber causes a change in the piezoelectric constants [78]. Constants having a strong impact

on the respective behavior were identified and altered. Subsequently, the calculation scheme described in Section 2.1 was applied to obtain consistent parameter matrices. Overfitting was avoided by the following approach:

- The coupling coefficients k_p and k_{15} were reduced by 5% to account for a lower EM coupling of the material in comparison with the values from the data sheet.
- The piezoelectric charge constant d_{33} was reduced by 6% to realize a slightly lower thickness-mode conversion. In contrast, d_{15} was increased by 6% to pronounce the planar resonance.
- The density ρ_0 of the piezoceramic was reduced by 10% to match conducted measurements. This leads to an increase in f_c.
- In order to increase the stiffness of the composite disk and thereby decreasing Φ_t, E_{adh} was increased by 20%.
- The elastic compliance s_{33}^E and s_{11}^E were both reduced until a match in center frequency f_c and planar resonance f_p of 5% was achieved.

For achieving the intended accuracy for both resonance frequencies, s_{33}^E and s_{11}^E had to be reduced by 28.7% and 5.0% respectively. These reductions as well as the increase of E_{adh} suggest that the actual stiffness of the embedded piezocomposite disk is higher than expected. These findings do not match the best-fit constants of the ECM (ref. to Tab. A.1). A possible explanation of this inconsistency is the limited representation of the transducer geometry in the 2D KLM model. The reduced compliances are well within standard ranges of typical piezoceramics (e.g. s_{33}^E of PZT-4 is $15.5{\cdot}10^{-12}\mathrm{m}^2/\mathrm{N}$). Hence, the risk of excessive overfitting is low.

The final set of parameters and constants resulting from the described fit are listed in Tab. A.2 and Tab. A.3. The modeled FASP amplitude is shown in Fig 6.11a next to an exemplary measurement. Comparing these results with the initial model in Fig. 6.8a yields that the thickness mode matches the measurement well. The behavior at frequencies above 4 MHz is closer to the measurement,

with a good prediction of the planar resonance. Furthermore, higher sensitivity fluctuations, especially below 2 MHz, are predicted. These resemble the measured example to some extent, suggesting that the model is able to cover the root cause of this effect. The prominence of the fluctuations correlates with the height of the defined structural loss factors. Hence, the in the previous section derived expressions enable realistic predictions.

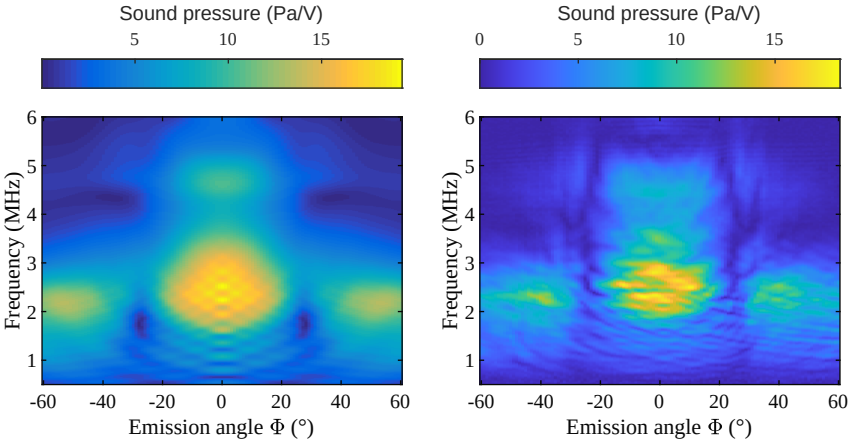

(a) FASP amplitude of FE model after the fit.

(b) Measured FASP amplitude of an exemplary transducer.

Figure 6.11: FE model (a) to measurement (b) comparison of the FASP amplitude over a circular segment of 120° at 10 cm axial distance after the parameter fit.

The quantitative comparison in Tab. 6.4 shows that the model fits the measurements significantly better than with the initially used parameters (ref. to Tab. 6.2). Now, most characteristics deviate by less than 15%. Only the lower bandwidth threshold f_l is still 0.42 MHz below the measurement, leading to the difference in bw_{us}. A better fit would require to lower s_{33}^E even further, which probably causes overfitting and unrealistic material properties.

Even though all parameter adjustments are within reasonable ranges, it is likely that the real parameters differ from the assumptions. By introducing more sophisticated material models, for example anisotropic damping or non-linear material stiffness, the model predictions could be improved further. Still, the fitted FE model predicts the performance well enough to study the impact of material parameters and dimensions. Furthermore, it allows for a comprehensive analysis and evaluation of the design. These topics will be studied in the following chapter.

Table 6.4: Mean transducer characteristics from measurement in comparison with the fitted FE model.

	f_l [MHz]	f_u [MHz]	f_c [MHz]	bw_{us} %	Φ_t [°]	S_c [Pa/V]	f_p [MHz]
Measurement	1.66	5.06	2.55	134.33	42.81	18.61	4.50
Fitted FE model	1.22	5.10	2.43	164.27	48.98	19.31	4.63
Difference	-26.5%	+0.8%	-4.9%	+22.2%	+14.4%	+3.8%	+2.9%

6.3 Summary and Discussion

For accurate analysis and optimization of the TAS III design, two modeling approaches were developed. The first encompasses an advanced equivalent circuit model. This model is an extension of the original KLM model, enabling the consideration of two vibration modes. Brute-force parameter optimization was conducted to obtain a very good fit (deviations below 1%) with respect to characteristic resonant frequencies. An initial estimate of transducer directivity using a simple analytical expression yielded low prediction accuracy. Hence, the equivalent circuit model is best suited for analyzing the resonance and impedance behavior of the TAS III design.

The second modeling approach encompasses a FE analysis with full coupling of electrostatic, structural mechanic and pressure acoustic physics. A procedure was developed to fit the model to the average TAS III performance. This procedure

consists of manual adjustments, parameter sweeps and a routine to preserve a consistent set of piezoelectric constants. Considering frequency-dependent mechanical damping properties of several utilized materials were found to significantly improve model predictions. Damping parameters were obtained by converting the measured acoustic attenuation of a material to a structural loss factor. After the fitting procedure, a good fit (deviations below 15% for most characteristics) over a wide range of emission angles and frequencies was achieved. Hence, the developed models are well-suited to study measured effects and identify improvements.

7 Design Analysis and Optimization

In this chapter, the TAS III design is analyzed and discussed with respect to the measured functional ultrasound characteristics. As stated in Section 5.4, several of these characteristics comply well with the requirements, while others deviate from the design goals. In the following, the measured differences of the lower frequency limit f_l, the opening angle Φ_t and detected sensitivity fluctuations are studied in detail.

7.1 Lower Frequency Limit

With more than 1 MHz higher than the intended value, the measured mean of f_l deviates significantly from the design goals. As a countermeasure, either the center frequency f_c of the transducer can be reduced, or the bandwidth bw_{us} increased. When assuming a constant bw_{us}, reducing f_c would also lower f_u. However, this would limit the maximum achievable image resolution, as explained in Section 2.3.

In order to increase the bandwidth of a piezoceramic transducer, different techniques have been developed. Three common methods are the improvement of the piezoelectric material, modifying the matching and acoustic backing as well as optimizing the structure of the composite [82]. In this design, the piezoelectric material cannot be easily improved since performance and production is already optimized for the intended use [84]. Requirements from manufacturing and medical device regulation also limit adjustments for the matching, the filler

and the acoustic backing. Furthermore, the achieved fractional bandwidth of 134.33% is already very high. Hence, it is not feasible to reach the desired limit of $f_l = 0.5$ MHz by only increasing the bandwidth. Reaching the design goal requires therefore a reduction of f_c.

A parameter study was conducted to evaluate the effects on the performance when reducing f_c. This reduction is achievable by varying the outer dimensions of the piezoceramic fiber. The 2D KLM model was used for the study since it enables brute-force, multi-parameter sweeps within reasonable computation time. Promising parameter sets were then fed into the FE model to derive the resulting functional ultrasound characteristics.

Increasing the thickness h_0 of the piezoceramic fiber corresponds directly with a reduction in f_c. However, it also reduces the effective electric field and according to Eq. 2.1 the resulting strain. This, in turn, leads to a reduction in ultrasound output. A countermeasure is to increase the radius r_0 of the fiber. The total ultrasound output can be estimated with the 2D KLM model by integrating the transfer function over frequency (see Eq. 6.5). As study goal, a reduction of f_c by 0.5 MHz was set. The thickness and radius were swept between $0.7\ h_0, r < h_0, r < 1.7\ h_0, r_0$ in 256 equally spaced increments. For each parameter combination, the ultrasound output was calculated.

The results of the study are shown in Fig. 7.1. At first, the required increase in h_0 to reduce f_c by 0.5 MHz was derived from Fig. 7.1a. There, a reduction of h_0 by 186 µm was found. Then, the necessary increase in r_0 was derived at the point where equal ultrasound output is present. This is illustrated in Fig. 7.1b, with the relative change in h_0 on the x-axis, the relative change of r_0 on the y-axis and the ultrasound output color-coded. In order to avoid losses in ultrasound emission, an increase of r_0 by 66 µm is required. This point in the graph is marked by the red dot.

In the next step, the found changes in dimensions were analyzed with the FE model. The resulting frequency response amplitude and directivity are shown in Fig. 7.2, in comparison to the current design. Important to state is that the intended reduction of f_c is also predicted by the FE model. Furthermore, even

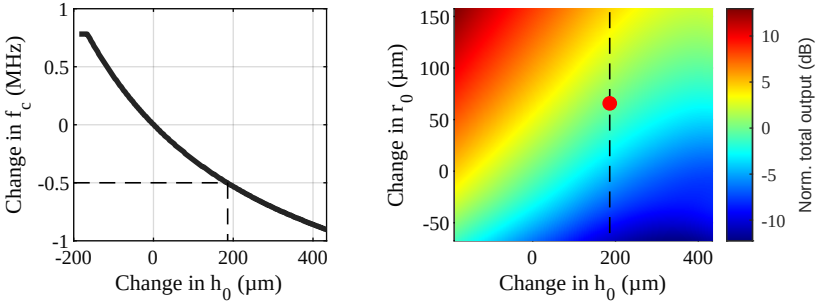

(a) Dependency of the center frequency on the thickness.

(b) Normalized integrated ultrasound output dependent on the thickness and radius of the piezoceramic fiber.

Figure 7.1: Results of a parametric sweep to obtain a reduction in center frequency by 0.5 MHz (a) and the corresponding increase in radius to level the ultrasound output (b) using the 2D KLM model.

though the peak sensitivity increases by 1.5 dB, the integrated ultrasound output remains nearly constant, with an overall change of less than 1%. This supports the validity of the 2D KLM model predictions.

An increase in r_0 of 66 µm lowers the planar resonance frequency, which would shifts f_u from 5.1 MHz down to 3.9 MHz. The impact of this shift on the achievable image resolution must be analyzed with respect to the entire imaging system and the reconstruction algorithms. Past experiences with the 3D USCT II system showed that the theoretical resolution limit defined by the highest frequency could not be reached. Reasons for that were limitations in position accuracy and a limited transducer bandwidth [140]. Hence, lowering the requirements with respect to f_u might be an acceptable trade-off for future designs.

The increase in r_0 also results in a decrease of Φ_t by 2.74°. This change seems minor at first glance, but since Φ_t is already a limiting factor in the current design, further reduction must be avoided. Several material properties and dimensions can be altered to counteract this effect. A detailed analysis on parameters which impact Φ_t is given in the following section.

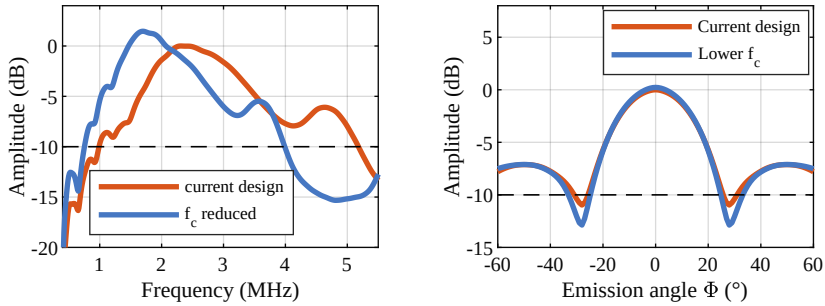

(a) Frequency response amplitude of the main lobe.

(b) Broadband directivity.

Figure 7.2: Predicted changes in the frequency response amplitude (a) and directivity (b) when increasing h_0 and r_0 in the FE model.

Since the vibration behavior of the transducer is determined not only by the properties and dimensions of the piezoceramics but also by the embedding materials, changes in their mechanical properties affect f_c as well. Therefore, when aiming for a specific center frequency, the use of different materials might be a suitable option. However, this has a big impact on the manufacturing processes used and must be weighed against the expected benefits.

7.2 Opening Angle

The second functional ultrasound characteristic which deviates significantly from the design goals is Φ_t. This limits the illumination of larger breasts when scanned with a single transducer. Estimating the directivity with the analytic expression presented in Section 6.1.3 showed that the transducer cannot be modeled as a circular piston. When analyzing the vibration behavior with the FE model, it was found that the piezoceramic fiber deforms larger areas of the matching layer. This increases the effective size of the radiation surface and leads to a decrease in Φ_t.

The effective radiation surface depends mostly on the thickness h_{ml} of the matching layer, the elastic modulus E_{adh} of the filler material and r_0. Decreasing r_0

directly enlarges Φ_t, but also causes lower ultrasound output. Furthermore, the achievable decrease is limited by the manufacturing processes of the piezoceramic fibers, where production gets more complicated the thinner the strands are.

In order to quantify the impact of h_{ml} and E_{adh} on the directivity, a FE simulation study was conducted. Initial tests showed that both parameters have to be reduced to increase Φ_t. For quantitative analysis, both were individually varied between $0.5 \cdot E_{adh}, h_{ml} < E_{adh}, h_{ml} < 1.2 \cdot E_{adh}, h_{ml}$ in 64 equally spaced increments. This range makes it possible to identify trends in the change of characteristics, while the resulting material parameters are still within feasible ranges.

The results of the FE study when varying E_{adh} in the given range are shown in Fig. 7.3a. There, a direct relation between lowering E_{adh} and an increase in Φ_t can be observed. A more detailed depiction of the resulting changes in directivity is shown in Fig. 7.3b. In this graph, the colors give the relative emission amplitude dependent on changes in E_{adh}. The amplitude is normalized to the maximum of the current design. When analyzing the changes, a gradual reduction in peak amplitude can be observed with falling E_{adh}. This reduction leads to a wider range above the -10 dB threshold definition, resulting in a larger Φ_t.

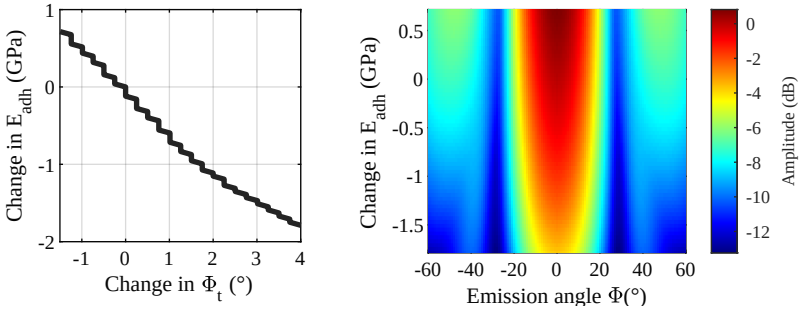

(a) Changes in Φ_t when varying E_{adh}.

(b) Normalized broadband directivity when varying E_{adh}.

Figure 7.3: Impact on the opening angle Φ_t (a) and the directivity (b) when varying the elastic modulus E_{adh} of the filler material in the FE model. The variation is given as relative change with respect to the current design.

Lowering E_{adh} also causes a lower emission in the side lobes, which might be interesting when it comes to the optimization of the main lobe response. Reducing E_{adh} is strongly limited by available materials and their usability for the applied processes. Since the overall gain is relatively low, changing the filler material alone does not lead to the desired increase in Φ_t.

Varying h_{ml} leads to changes in Φ_t, directivity and emission amplitude, shown in Fig. 7.4a. There, it is interesting to notice that the thickness has to be decreased by more than 100 µm to see effects on Φ_t. Further decrease leads to a steady increase of Φ_t up to a maximum of 4° within the examined range. This effect is also reflected in the directivity plot in Fig. 7.4b, where not only wider angles but also higher amplitudes are predicted with decreasing h_{ml}. In practice, thinning the matching layer has its limits since the material is only available up to a certain thickness. Furthermore, processing becomes more difficult the thinner the material is. Similar to the previous study on the effects of E_{adh}, a relatively small increase in Φ_t can be expected when h_{ml} is decreased. Hence, different measures need to be considered to reach the design goal with the current technology.

In ultrasound probes, a common way to alter the directivity is the use of acoustic lenses. Usually, these lenses are applied on top of the entire array to obtain better focusing [53]. However, in case of the TAS III a more defocused emission is

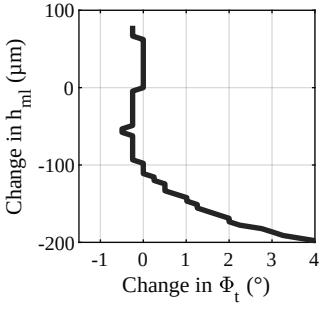

(a) Changes in Φ_t when varying h_{ml}.

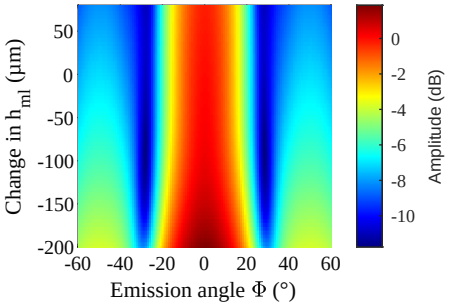

(b) Normalized broadband directivity when varying h_{ml}.

Figure 7.4: Impact on the opening angle Φ_t (a) and the overall directivity (b) when varying the thickness h_{ml} of the matching layer in the FE model.

desired. Moreover, the random positioning of the transducers on the composite disk would require the use of individual lenses. This limits the diameter of a single lens to approximately 3 mm. In the next step, a FE simulation study was conducted to estimate the expectable gain in Φ_t and to find suitable sizes of a convex lens. Spherical segments with a diameter of 3 mm and a thickness up to 2 mm were investigated to comply with the size constraints. As lens material, ADH-2 was chosen since it can be easily molded and exhibits suitable elastic properties (see properties in Tab. A.3).

Two general trends were found when studying suitable acoustic lenses. First, the thicker the spherical segment, the larger the resulting Φ_t. This corresponds to a stronger curvature of the lens and an increase in refraction angle. Second, larger sensitivity fluctuations are predicted when increasing the thickness of the lens. If the thickness exceeds 0.5 mm, fluctuations of up to 20 dB are predicted. Therefore, a suitable compromise was found for a spherical segment with 3 mm diameter and a segment thickness of 0.3 mm. Figure 7.5 shows the resulting directivity and FASP amplitude after including the lens in the FE model. As a result, Φ_t increases by 14° to 63°, with a slightly higher peak pressure of the main lobe (comp. to Fig. 6.11). The side lobes are less prominent in the investigated angular range. Moreover, for frequencies below 2 MHz, the defocusing of the lens introduces distinct sensitivity minima leading to higher sensitivity fluctuations.

The dimensions of the investigated lens requires high manufacturing and positioning tolerances. A more feasible approach might be the use of larger transducers specially optimized for emission. Multiple piezoceramic fibers could be bundled to form a single transducer with a larger surface. Another interesting approach is published in [141], where a flexible piezocomposite array is spherically curved to obtain almost omnidirectional emission. However, both of the discussed approaches would require a profound redesign of the current 3D USCT imaging concept.

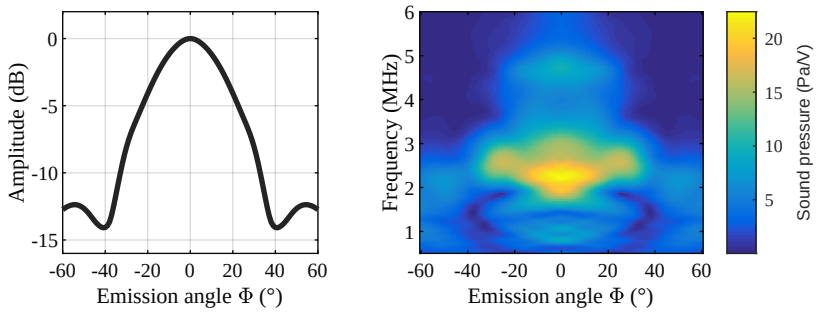

(a) Normalized directivity.

(b) FASP amplitude.

Figure 7.5: Resulting directivity (a) and FASP amplitude (b) when adding a convex lens with 3 mm diameter and 0.3 mm thickness of the spherical segment on the front of a transducer in the FE model.

7.3 Sensitivity Fluctuations

The sensitivity fluctuations found in Section 5.3 are best explained by analyzing the response of a transducer in the time domain. There, it can be seen that the main pulse is followed by smaller echoes. An exemplary measurement is shown in Fig. 7.6a. It displays the normalized impulse response of a TAS III transducer measured at 10 cm distance with the hydrophone. In order to emphasize the effect of the echoes, a short and a long time segment were cut from the data using Tukey-windows. The corresponding frequency response amplitude is shown in Fig. 7.6b. The data from the long window exhibits the typical fluctuations, while the short window shows a much smoother response. Hence, the sensitivity fluctuations can be attributed to echoes after the main pulse since these introduce additional frequency components with different phase angles. The larger these echoes, the stronger the fluctuations in the spectrum.

The origin of echoes are manifold. Internal reflections on the front and rear leading to sound emissions with delays are a likely cause [142]. Extensive lateral damping and accurate acoustic matching usually suppresses these internal reflections. Moreover, when using a backing material that exhibits a similar acoustic

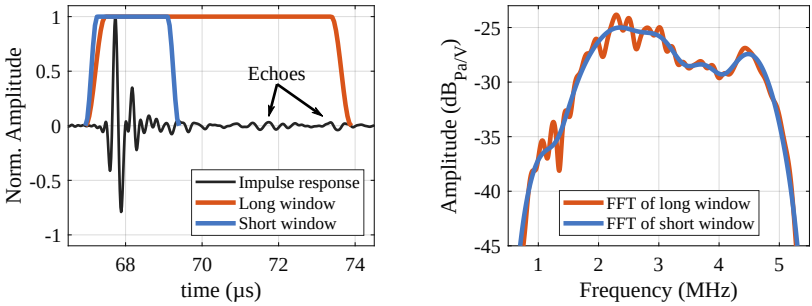

(a) Impulse response measured at 10 cm axial distance and a short and long time window to cut the data.

(b) Frequency spectra of the respective time windows.

Figure 7.6: Analysis of sensitivity fluctuations by applying different time windows to a measured impulse response (a) with the corresponding frequency spectra (b).

impedance to that of the piezoceramic, reflections from the rear are minimized [53]. In the TAS III design, these factors are well considered but not optimal due to material and design constraints.

Another factor affecting the echoes was found in the vibration behavior. Ideally, the piezoceramic should behave like a piston or disk to deform linearly in thickness or planar direction, depending on the frequency. However, a modal analysis revealed that the resonating behavior of the piezoceramic fiber exhibits coupled vibration modes that cause bending of the fibers in the composite. Figure 7.7 visualizes this effect at two distinct frequencies. The bending is more prominent at lower frequencies due to the higher displacement at thickness resonance. The energy stored in the bending is thus released at a later time causing echoes. Enlarging the diameter would better suppress this effect, leading to a more linear vibration behavior. However, the requirements on Φ_t limits the usable diameter of the piezoceramic fiber.

As was already discussed in Section 6.2.2, higher damping of the piezoceramic fiber reduces sensitivity fluctuations. It can be achieved by increasing the damping properties of the filler and acoustic backing. The PU composite used for acoustic

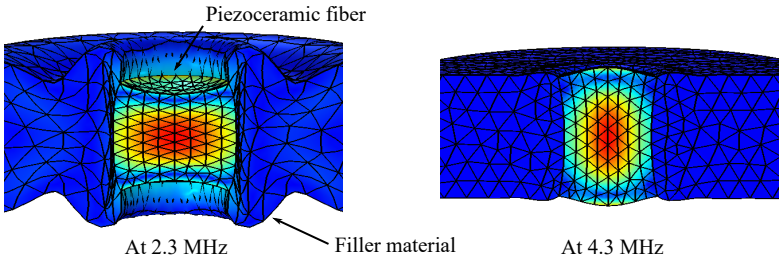

Figure 7.7: Vibration behavior of a single TAS III transducer at two distinct frequencies showing bending of the piezoceramic fiber.

backing already exhibits very high damping [86], leaving possible improvements mostly for the filler.

Different filler materials and the resulting echoes were studied with the FE model. The axial impulse response at 10 cm distance was obtained by applying the inverse FFT on the frequency response. PU was investigated since it exhibits higher damping than the currently utilized epoxy adhesive. A relatively stiff PU composition was chosen to ensure sufficient mechanical stability of the composite in perspective. The elastic properties were taken from [143], while an intermediate damping listed in Tab. A.3 was assumed.

In addition to the plain PU, the PU composite used for the acoustic backing was investigated. Besides high damping properties, it also exhibits an elevated acoustic impedance to better match the piezoceramic. The predicted impulse responses of the current design, the plain PU and the PU composite are shown in Fig. 7.8. An echo forms approx. 3 µs after the main pulse for all variants. This echo is most prominent in the current design, followed by the plain PU and best suppressed when using the PU composite. Moreover, the amplitude of the main peak is larger when plain PU is used, and increases even more for the PU composite. Both of these effects would be very beneficial in imaging.

Comparing the modeling results with the exemplary measurement in Fig. 7.6 shows that they match the measurement only to some extent. A shorter ringdown and a more pronounced single echo are predicted. Nevertheless, an analysis of

complex effects can be achieved with the FE model. Hence, it represents a suitable tool for deriving a strategy for improvement.

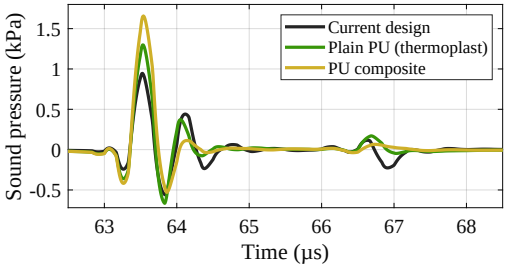

Figure 7.8: Changes in the predicted impulse response with the FE model when varying the material of the filler.

In summary, a reduction of sensitivity fluctuations can be achieved best by increasing the damping of the filler material. However, changing the filler material has to be evaluated with respect to the manufacturing processes of the composite disk and likely requires profound process adjustments. For optimization, accurate material parameters are required to reliably predict the gain in performance. The approach presented in [4] to derive the frequency dependent attenuation provides a useful tool for future redesigns.

7.4 Redesign and Discussion

This section presents a redesign proposal to further improve the performance of the TAS III. The adjustments incorporate the findings from the previous sections aiming at reducing f_c, increasing Φ_t, and damping sensitivity fluctuations. The implemented changes in the FE model are listed in Tab. 7.1. All other model parameters and dimensions were kept constant.

Comparing the adjusted design with the current design is best achieved by analyzing the FASP. Both, the predicted FASP amplitude and phase angle at 10 cm

Table 7.1: Recommended design adjustments to optimize the performance of the TAS III.

	$\mathbf{h_0}$	$\mathbf{r_0}$	$\mathbf{h_{ml}}$	Filler material
Current design	0.60 mm	0.225 mm	0.40	ADH-2 (see Tab. 3.2)
Adjusted	0.72 mm	0.275 mm	0.25	PU (see Tab. A.3)

distance over a circular segment of 120° are shown in Fig. 7.9. The phase angle was corrected according to the approach described in Section 5.1.2. As intended by the adjustments of h_0 and r_0, the thickness and planar resonances shift towards lower frequencies. The increase in h_0 was chosen a bit smaller than identified in Section 7.1, since the change in h_{ml} and the filler material also affect f_c. Compared to the current design, the FASP amplitude shows less sensitivity fluctuations due to the increase of damping of the filler (compare to Fig. 6.11 for current design). Interesting is the phase angle behavior of the transducer. At thickness resonance, the phase angle reaches 180°, which can be seen in the sudden color change in Fig. 7.9b. From there, the phase angle remains within the main lobe relatively constant. This behavior would be advantageous when applying advanced image reconstruction algorithms.

A quantitative comparison of the functional ultrasound characteristics is given in Tab. 7.2. It lists the initial design requirements, the average measurement results, the results from the fitted FE model and the predicted performance after adjusting the design. Direct comparison shows that the design adjustments cause changes in all characteristics. From left to right, f_l comes closer to the design goal of 0.5 MHz while f_u shifts down considerably. This results in a significant reduction of bw_{us}. Prolonging h_0 lowers f_c by 0.5 MHz. The reduction in t_{ml} and the changed filler material cause an increase in Φ_t by 4°. Moreover, a gain in peak sensitivity by 59% is predicted, resulting in a potentially higher SNR.

At first glance, the adjustments have a rather negative impact on the performance. Especially the decrease of bw_{us} would be a setback for future designs. However, more thorough analysis shows that the predicted decrease results from a rise in emitted sound pressure at f_c. This rise causes the frequency range around the planar resonance f_p to fall below the -10 dB threshold, even though the actual

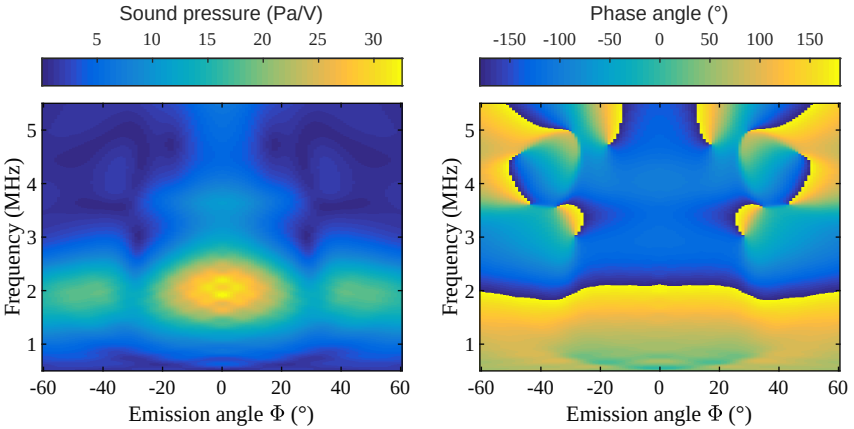

(a) FASP amplitude evaluated at 10 cm distance.

(b) FASP phase angle at the origin ($t_r = 0$).

Figure 7.9: Predicted FASP amplitude (a) and phase angle (b) of the proposed transducer redesign.

values are similar to the current design. Hence, higher frequencies would still be feasible if the utilized signal amplifiers exhibit sufficient dynamic range. From a practical point of view, another limiting factor of the proposed adjustments is the reduction of t_{ml}. This would result in a very thin matching layer, where the availability of suitable materials must be evaluated with possible suppliers. In any case, production and handling would be more challenging.

Table 7.2: Quantitative comparison of functional ultrasound characteristics for the redesign proposal.

	$\mathbf{f_l}$ [MHz]	$\mathbf{f_u}$ [MHz]	$\mathbf{f_c}$ [MHz]	$\mathbf{bw_{us}}$ %	$\mathbf{\Phi_t}$ [°]	$\mathbf{S_c}$ [Pa/V]	$\mathbf{f_p}$ [MHz]
Initial requirement	0.50	5.00	2.50	180	60	n.d.	n.d.
Current design	1.66	5.06	2.55	134.33	42.81	18.61	4.5
Fitted FE model	1.22	5.10	2.43	164.27	48.98	19.31	4.63
Adjusted FE model	1.08	2.90	1.97	92.5	52.98	32.54	3.64

In summary, the presented design adjustments show that each change comes with certain trade-offs. For example, reaching the desired f_l can only be achieved when changing the dimensions of the fiber. This results in a significant reduction in sensitivity and prevents the design goal for f_u from being met. The developed modeling approaches are essential tools in estimating the expectable gain, balancing the trade-offs and exploring the boundaries of the technology. Combining results from distinct modeling approaches may also serve as an example of thorough design analysis and optimization for other applications.

Only incremental improvements in opening angle and bandwidth can be achieved by feasible design adjustments. This suggests that the TAS III design is already close to the optimum which can be achieved with the utilized piezocomposite technology. Hence, for substantial improvements in transducer performance, different transducer technologies must be considered. This topic is explored in detail in the following chapter.

8 Alternative Transducer Technologies

A substantial increase in bandwidth and opening angle of TAS III transducers is limited by the currently used piezocomposite technology. Different technological approaches to generate and receive ultrasound could help to overcome these limitations. In this chapter, three technologies are explored in terms of their strengths, achievable improvements and limitations for future 3D USCT generations.

8.1 Overview of Explored Technologies

The first technology to be explored are single-crystal piezoelectric materials. Single-crystals are known to produce a very high strain, bandwidth and EM coupling, making the material in terms of emitting performance superior to the currently used polycrystalline ceramics [144, ch. 6]. A transducer based on single-crystals would still require acoustic backing and matching layers, making this approach closest to the TAS III design.

The second and third technologies comprise piezoelectric and capacitive micromachined ultrasound transducers (PMUTs and CMUTs). These transducers generate ultrasound by flexural vibrations of thin membranes. The deformation of the membrane is either caused by a piezoelectric material in case of PMUTs, or by electrostatic forces in CMUTs. Both technologies are based on micromachining processes (lithography, deposition etc.). This enables very small designs, high design freedom and the possibility of efficient, cost-effective mass production. In addition, the acoustic impedance of the membrane matches better with water or

human tissue, resulting in a theoretically higher efficiency and bandwidth than piezoceramic transducers [145, 146]. These properties, as well as the possibility of monolithic integration with electronics, makes PMUTs and CMUTs very interesting for 3D USCT.

The operation principles of PMUTs and CMUTs are shown in Fig. 8.1. In PMUTs, a piezoelectric film is deposited on a metalized layer foreseen on top of a thin silicon oxide. The oxide layer in turn covers a cavity provided on a rigid substrate (e.g., silicon), enabling bending motion. The membrane motion is caused either by d_{33} or d_{31} strain of the piezoelectric film [147, 148].

In CMUTs, a flexible laminate containing a metalized layer is bonded on top of the cavity. Below the cavity material, another metalized layer is provided. This enables the application of an electric field. The field causes static attraction and pulls the top plate towards the cavity. For achieving high performance, large electric fields are required in the cavity. Therefore, a DC bias voltage is usually added to an AC excitation signal [149].

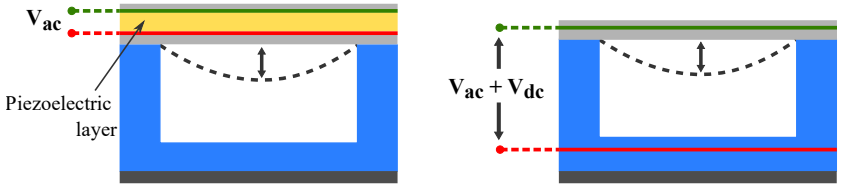

(a) Operation principle of PMUTs. **(b)** Operation principle of CMUTs

Figure 8.1: Ultrasound transducer technologies based on microfabrication techniques (schemes adopted from [147]).

8.2 Single-Crystal Test Transducer

The fundamental difference between single-crystals and PZT ceramics is the manufacturing method. The basis of PZT materials are usually powders mixed from granules of the respective raw materials, e.g. Zr and Pb. The powder is

further processed and brought into the desired shape before sintering. In order to finalize the ceramics, several post processing steps such as grinding, electrode deposition and polarization are required. This results in a polycrystalline structure, where the polarization corresponds to a superposition of local dipole alignments, also called domains [91].

Single-crystals contain only one domain, leading to significantly better piezoelectric properties. They are grown by soldification from a melt in a controlled environment. The growth velocity and size of the crystal is limited, making the material more expensive than conventional PZTs. Grown crystal boules are cut into the desired thickness, polished, foreseen with electrodes, diced and polarized [56, 150]. Single-crystal piezoelectric materials in different fabrication states are shown in Fig. 8.2

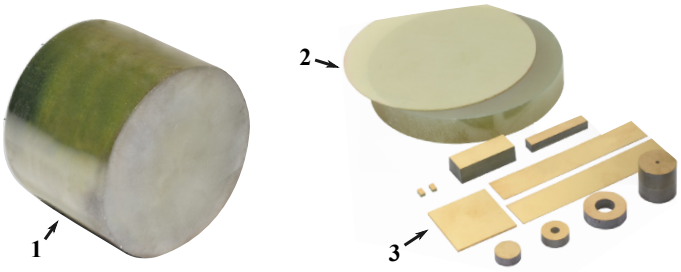

Figure 8.2: Single-crystal piezoelectric materials in different fabrication states, ranging from the raw boule (1), to a cut slice or waver (2) and finalized samples (3). The picture originates from [151].

The fundamental differences in manufacturing between polycristalline ceramics and single-crystals prevents the direct replacement of the utilized piezoceramic fibers (ref. to Section 3.3.1). Hence, a profound redesign of the array would be required if single-crystals were to be used. More data on the expected performance gain is therefore needed to outweigh advantages and disadvantages. For this purpose, several test transducers were manufactured. Compared to the TAS III, larger and simplified geometries were chosen to facilitate fabrication and testing. A model was developed and validated with the results from characterizing the test

transducers. This model was subsequently adjusted to match the TAS III design in order to derive comparable conclusions.

Plates of single-crystal composites (PMN-PT, Ibule, South Korea) with a fill factor of 0.6 and a center frequency of 2.5 MHz were the base material for the test transducers. With a thickness h_0 of 440 µm, these are thinner than the current composite disks due to the lower stiffness of the material. Octagons with an inner diameter of 6 mm were cut from these plates to obtain an approximately uniform acoustic field. These dimensions ensure frequency separation between the thickness and planar modes, with a small but still resolvable opening angle. On one side of the octagon, an unetched matching disk was bonded. On the other side, a wire was foreseen using conductive adhesive (Adh. 1, see Section 3.4). This configuration is shown in Fig. 8.3a before integration into a plastic housing and molding of acoustic backing.

The 2D KLM model introduced in Section 6.1 was used to obtain a virtual representation of these test transducers. Since the thickness and planar resonance are well separated, the lateral coupling was set to zero. Unfortunately, only a very sparse set of piezoelectric constants is available for the utilized single-crystals [152]. Hence, several conversions were necessary to obtain the required model parameters. The mechanical stiffness to calculate the longitudinal speed of sound (ref. to Eq. 2.12) was calculated by $c_{33}^D = 1/s_{33}^D$. The open permittivity was converted to the clamped counterpart using Eq. 8.1, as suggested in [41].

$$\epsilon_{33}^S = \epsilon_{33}^T \cdot (1 - k_{33}^2) \cdot (1 - k_{31}^2) \tag{8.1}$$

The effective piezoelectric area of the octagon composite was calculated according to Eq. 8.2 to obtain the blocking capacitance C_0 (see Eq. A.1 in the appendix). There, r_0 is the inner radius of the octagon and a_f the fill factor of the composite.

$$A_0 = 8 \cdot (r_0 \cdot a_f)^2 \cdot \tan(22.5°) \tag{8.2}$$

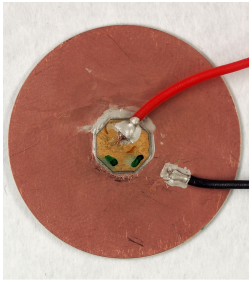

(a) Octagon of single-crystal composite with an inner diameter of 6 mm bonded on a matching disk.

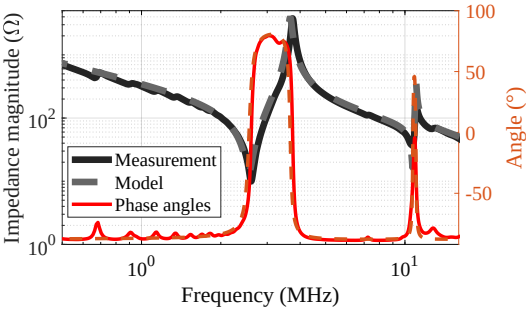

(b) EMI measurement of octagon composite compared to predictions from a KLM model.

Figure 8.3: Prototype transducers with single-crystal composites during manufacturing (a) and EMI measurements compared to modeling results (b).

The measured and modeled EMI of the initial octagon composite is shown in Fig. 8.3b. The model covers the resonance behavior of the octagon very well, not only in terms of the impedance value, but also the phase angle. Furthermore, the measured harmonic resonance at 10.9 MHz is also predicted accurately. These results, and the lack of a complete set of piezoelectric constants, prompted the use of the KLM model instead of a FE model for further predictions and analyses.

In order to characterize the FASP generated by the test transducers, a circular segment of 30° at a radius of 60 mm and a resolution of 0.25° was examined with the setup described in Section 5.1. In parallel, the FASP was modeled using the approach described in Section 6.1.3. A direct comparison of the measurement and the modeling results is given in Fig. 8.4. As shown there, a good agreement of the general behavior can be achieved, especially in the range of maximum sensitivity. The dependence of the emission angle on the frequency follows the predicted pattern to most extent. However, sensitivities below 2 MHz and side lobes of higher order are less prominent in the measurement.

Both, the measurement and the model predictions show a broadband behavior of the test transducer. With a measured center frequency of 2.72 MHz and a -10 dB

bandwidth of 4.6 MHz, the transducer demonstrates a fractional bandwidth of 169%. This exceeds the TAS III design by 35%. This is remarkable since the octagonal transducer exhibits only the thickness and no planar resonance in the examined frequency range. In addition to the enhancement in bandwidth, single-crystals show high output pressures due to larger strains. Since the dimensions of the test transducer are different from the TAS III design, a direct comparison is not meaningful. However, a first estimation of the expectable gain can be obtained with the model. After adjusting the dimensions to those of the TAS III design, the total emitted sound pressure is predicted to increase by 86%.

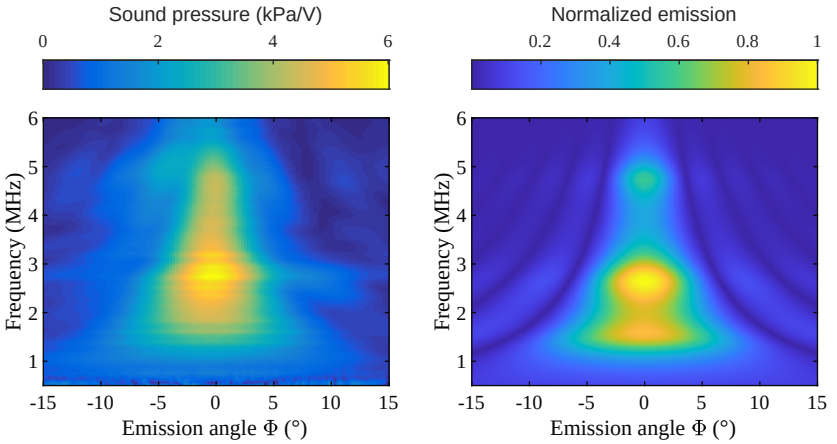

(a) Measured FASP amplitude over a circular segment of 30°.

(b) Modeled FASP amplitude obtained via Eq. 6.7.

Figure 8.4: Measured (a) and modeled (b) FASP amplitude of single-crystal octagon test transducer.

In summary, using single-crystals instead of PZT ceramics could increase the fractional bandwidth by at least 35%, and almost double the emitted sound pressure. The limiting factor is the manufacturing process, which is not compatible with the currently used composite technology. However, the expectable gain in performance would justify further investigations in this alternative transducer technology.

8.3 PMUT Test Transducer

Piezoelectric micromachined ultrasound transducers (PMUTs) are manufactured from various piezoelectric materials, where one possible option is Aluminium nitride (AlN). Although it exhibits relatively poor piezoelectric properties, it is fully compatible with CMOS processes. Therefore, very compact transducer designs can be achieved by integrating the front-end electronics and the transducers monolithically. This enables high fill factors of the active chip area, making the technology very attractive for mass production [153].

One of the leading research groups on AlN PMUTs is located at the Autonomous University of Barcelona (UAB), led by Prof. Barniol. For ultrasound testing and evaluation of the technology, the UAB group provided several samples. These samples were previously designed prototypes that, to some degree, met the characteristics required [154, 155]. A magnified image of one prototype is shown in Fig. 8.5. The prototypes exhibit a rectangular design, where the top electrode is divided into an inner part (IT) and an outer part (OT). Both are individually connected to pads. This structurization increases the vibration amplitude compared to a single, full-surface electrode. Moreover, it enables differential operation [156]. The bottom electrode acts as GND and is connected to four pads. The cavity underneath the top electrode exhibits a side length of 80 µm, which results in a center frequency of approx. 3 MHz in water.

To be able to conduct ultrasound measurements, the PMUT samples had to be electrically connected and integrated into a housing. The following section presents the assembly and quality control measures performed to obtain functional transducers.

8.3.1 Manufacturing of Prototypes

The PMUT samples were electrically connected with wire bonds. For that, a test PCB was designed and used as a substrate for further processing. The samples were placed in the center of the PCB using the die bonder from Section 3.4 after

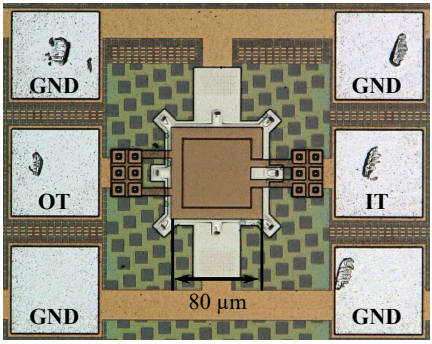

Figure 8.5: Prototype of AlN PMUT designed at UAB [154]. The bottom electrode is connected to four GND pads, OT is the outer part and IT the inner part of the top electrode.

dispensing two drops of ADH-2. Prior to application, the adhesive was pre-cured for 30 min at 50° to increase the viscosity for better shape retention. Figure 8.6a shows one PMUT sample after die bonding. The visible metalizations are a GND ring surrounding the sample, several test pads for connection and fiducials for automatic detection. The subsequent wire bonding was conducted with an automatic fine wire bonder (Bondjet BJ885, Hesse GmbH, Paderborn, Germany) in wedge-wedge mode. A 25 µm Al wire was utilized. Figure 8.6b shows one sample after successful wire bonding. For the purpose of redundancy, all four GND pads were connected.

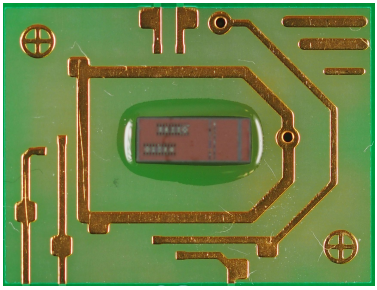

(a) PMUT samples on a designed test PCB after die bonding.

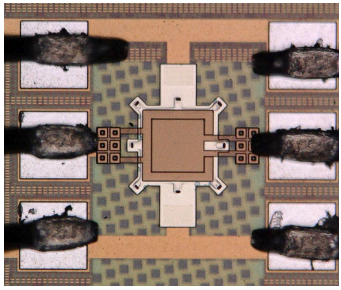

(b) PMUT sample after wire bonding.

Figure 8.6: Prototype transducers from PMUT samples after die (a) and wire bonding (b).

Initially and after the wire bonding, quality control measures were performed. This ensured that the samples were functional, both in the initial state and after processing. EMI measurements were conducted to assess the resonating conditions in air. The small size of the single PMUT cell and the low piezoelectric coupling of AlN makes these measurements challenging. Hence, a sensitive measurement setup for accurate compensation of parasitic circuit elements was required. Differential measurements with an impedance analyzer (4194A, Hewlett-Packard, Spring, USA) in four-terminal pair configuration was found suitable. With this setup, parasitic circuit elements are canceled and mutual couplings between the cables are suppressed. This enables measurements in a wide impedance range up to several MΩ [92, ch. 3]. For connecting the pads, a manual probe station with single-line microprobes (DCP-150R, Cascade Microtech, Beaverton, USA) was used. Figure 8.7a shows the described setup during measurement.

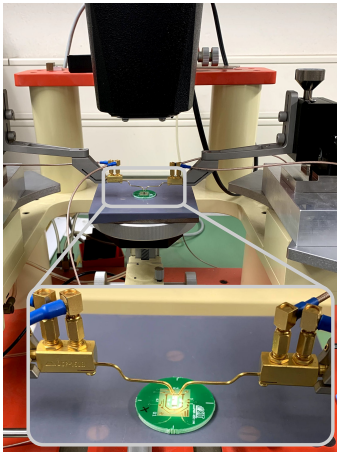

(a) Differential needle probe station for EMI measurements.

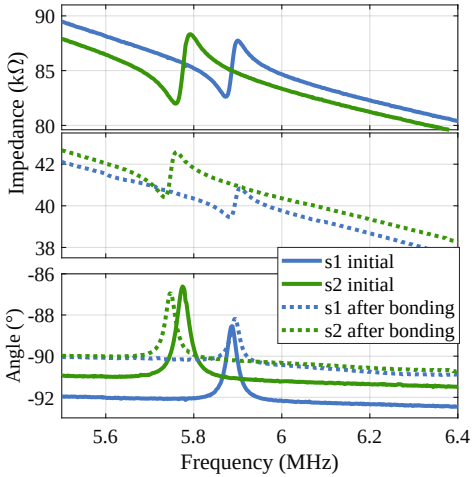

(b) Impedance amplitude (top and center axis) and angle (bottom axis) of two PMUT samples (IT to GND) before and after wire bonding.

Figure 8.7: EMI characterization of PMUT samples using a manual needle prober (a) and the measured change in impedance magnitude and phase angle caused by wire bonds (b).

The wire bonding had a prominent impact on the measured EMI. In Figure 8.7b, the amplitude and angle of two exemplary samples measured before and after wire bonding are shown. The flexural resonance was found at 5.80 MHz in air, which agrees well with previous measurements at UAB. The blocking capacitance of a the single PMUT cell was in average 328 fF, which results in an impedance range in the higher kΩ region. After wire bonding, the impedance halved, and slight frequency shifts were measured. These shifts are caused by additional parasitic capacitances induced by the wire bonds. The measurements after the bonding also showed that approximately 30% of the samples were damaged or not properly connected. Refinements in the bonding process are therefore required to optimize the yield.

For testing the PMUT samples in water, the wire bonds and GND pads needed electrical isolation. Furthermore, a protection layer was required to avoid damages on the fragile bonds. This is usually addressed with a glob top covering the entire die. In case of the PMUT samples, it is important to isolate only the wire bonds without covering the membrane to avoid blockage of vibrations. Therefore, a glob top was manually applied with ADH-3 using a fine needle. The adhesive was chosen for its high viscosity and quick curability with UV light. This process step was very challenging, since the adhesive had to be distributed on a µm scale without damaging the bonds or covering the membrane. Figure 8.8a shows a PMUT sample after successful application of a glob top. In the last step, the PCB was integrated into a housing and foreseen with suitable coaxial connectors. A PMUT test transducer is shown in Fig. 8.8b.

8.3.2 Characterization and Evaluation

Ultrasound measurements were conducted to assess the functional characteristics of the manufactured PMUT prototypes. Figure 8.9a shows the FASP amplitude of one exemplary sample over a circular segment of 90° at a distance of 20 mm. It exhibits a center frequency of 3.06 MHz and an opening angle of 66.7°. More characteristics can be found in Tab. 8.1 for later comparison. The speckles in the

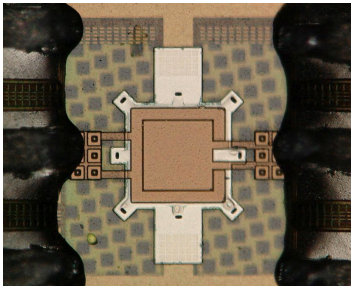

(a) Manually performed glob top to protect and isolate the wire bonds.

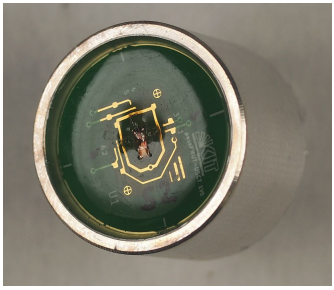

(b) Finalized PMUT test transducer.

Figure 8.8: Finalizing the PMUT test transducers by providing a glob top over the wire bonds (a) and integrating the PCB in a housing with 30 mm diameter (b).

image arise from low SNR even though an averaging factor of 2^{12} was applied. This results from the very low sound pressure emitted by the single PMUT sample.

For a better understanding of the technology, analytical and FE modeling was conducted. In case of analytical modeling, the approach described in [156] was followed. There, a PMUT is approximated as multilayer laminate which contains passive and piezoelectric layers. This allows for prediction of the membrane vibration modes considering one or two spatial dimensions. When applying the formula of a square plate resonator, the dominant resonance frequency was found at 6.37 MHz, which deviates by 10% from the impedance measurements in air [157]. Hence, the analytical modeling is well suited to analyze first design ideas with respect to a laminate composition.

An FE analysis was conducted in the next step to predict the acoustic field [157]. There, the PMUT was modeled in 3D according to the dimensions stated in [155] and [158]. Figure 8.9b shows the resulting FASP amplitude evaluated at a radius of 20 mm from the center of the membrane. In principle, the prediction shows a similar behavior as the measurement. The generated sound pressure amplitude fits the measurement very well, while f_c is slightly lower and Φ_t exceeds the measured value significantly. A quantitative comparison between measurement and model is given in Tab. 8.1.

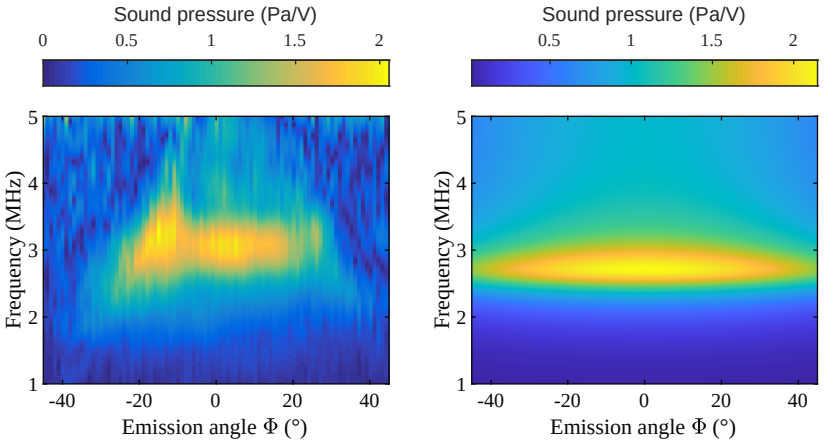

(a) Measured FASP amplitude over a circular segment of 90°.

(b) FASP amplitude from FE analysis.

Figure 8.9: Measured (a) and modeled (b) FASP amplitude of a PMUT test transducer at 20 mm distance.

After first successful measurements, several samples were found defective in subsequent tests. Microscopic inspection showed calcification on the surface of the PMUT samples, exemplarily shown in Fig. 8.10a. All attempts to remove the depositions did not restore functionality. Therefore, to be able to conduct repeated measurements, a protective encapsulation was required. As coating material, Polydimethylsiloxan (PDMS) is a suitable option. It is biocompatible and offers good sealing and isolation properties. Furthermore, efficient acoustic transmission can be achieved since the acoustic impedance is close to that of water [159].

Adding an additional layer on top of the laminate affects the dynamic behavior of the PMUTs. Two studies were found which investigated this effect. In the first study, a 0.9 µm thick layer of PDMS was applied on a CMUT array. This resulted in a reduction of emission sensitivity by 27%, and a 9% downward shift in f_c [160]. In the second study, a PMUT array was coated with different layers of PDMS up to a thickness of 120 µm. This resulted in a shift of f_c to higher

frequencies with increasing film thickness and a decrease of emission sensitivity by a maximum of 34% [161]. Furthermore, both studies reported an increase in bandwidth (+9% and +48% respectively), which would comply well with the 3D USCT requirements.

For the encapsulation of the PMUT transducer, a PDMS layer (Sylgard 184, Dow Chemical, Midland, USA) was cast with a thickness of approx. 1.5 mm. This thickness was chosen to reliably cover the previously applied glob top. Figure 8.10b shows the measured FASP amplitude generated by an encapsulated PMUT. When comparing these results with those before the encapsulation in Fig. 8.9a, a substantial change in the acoustic field is visible. The bandwidth bw_{us} increases by 30.2%, while the peak sensitivity S_c drops by 39%. However, the most prominent difference is the increase of Φ_t by more than 20°. The measured value now matches the simulation well. A possible reason for this improvement is the wider emission surface of the PDMS layer. This was not the case initially

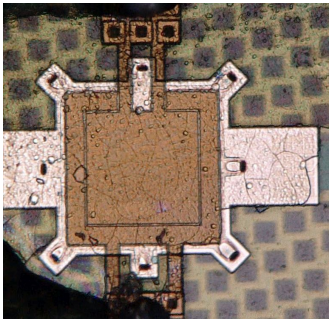

(a) Image from microscopic inspection showing calcifications on top of the PMUTs.

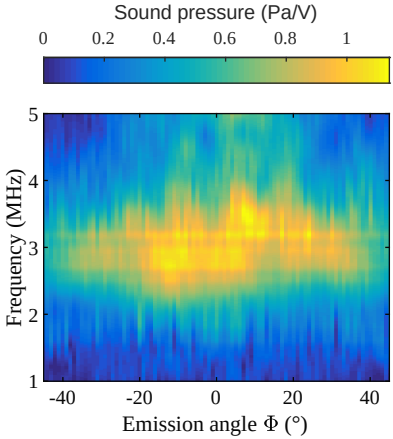

(b) Measured FASP amplitude after applying a 1.5 mm PDMS layer.

Figure 8.10: Depositions found after longer testing in water (a) and measured ultrasound characteristics after applying a protective PDMS layer on top (b).

since the glob top of the wire bonds limited the emission angle to some extent. A summary of the derived ultrasound characteristics is given in Tab. 8.1.

When evaluating the results with respect to the requirements of 3D USCT, several interesting aspects can be stated. The small size of a single PMUT leads to high opening angles, which considerably exceed the requirements. The downside of the small size is the limited sound pressure. For direct comparison with the TAS III characterization results, the PMUT sensitivity must first be extrapolated to a distance of 10 cm. When assuming the propagation of a spherical wave in the far field, the pressure amplitude decays by 1/r [125, cha. 5]. The estimation of S_c then yields a pressure of 0.41 Pa/V, which is in comparison 45.4 times lower than the current pressure. With respect to bw_{us}, the values of the TAS III are not reached. However, after applying a PDMS layers a bandwidth exceeding 100% could be achieved.

It is important to state that the tested PMUTs were not tailored to the specific needs of the 3D USCT device. Hence, a higher sensitivity can be expected for a customized design. In addition, the small number of the studied transducers limits the expressiveness of the presented results, but still gives a first indication of characteristics to be expected. In any case, replacing the PZT fibers with a single PMUT would be challenging in terms of the achievable sound pressure. An array configuration seems more reasonable, but this has to be evaluated with respect to the overall opening angle. Higher sensitivities can be achieved by using a

Table 8.1: Functional ultrasound characteristics of a single PMUT test transducer measured at 20 mm axial distance in comparison with the results from a FE model and the TAS III design.

	$\mathbf{f_l}$ [MHz]	$\mathbf{f_u}$ [MHz]	$\mathbf{f_c}$ [MHz]	$\mathbf{bw_{us}}$ %	$\mathbf{\Phi_t}$ [°]	$\mathbf{S_c}$ [Pa/V]	$\mathbf{S_c}$*
PMUT	2.09	4.35	3.06	74.2	66.7	2.06	0.41
FE model	2.21	n.d.	2.72	n.d.	>90	2.15	0.43
PMUT + PDMS	1.90	5.23	3.19	104.4	>90	1.26	0.25
TAS III design	1.66	5.06	2.55	134.3	42.8		18.61

*extrapolated to 10 cm axial distance

different piezoelectric material. For example, scandium doped AlN increases the sensitivity by a factor of three, while still fully compatible with CMOS production processes [162]. Furthermore, with the design freedom of the PMUT technology, multiple cells with different sizes and geometries could be integrated in the same array to enhance the bandwidth [163]. In summary, PMUTs are a very promising technology for future use in 3D USCT, but further investigations in addressing the gap in sensitivity, integration in an array and the development of frontend electronics are needed.

8.4 Polymer-based CMUTs

Capacitive micromachined ultrasound transducers (CMUTs) are another technological approach to realize micromachined transducers, but in contrast to PMUTs, the dynamic motion is caused by electrostatic attraction. Hence, no piezoelectric layer is required as part of the membrane laminate, leading to a lower mechanical impedance of the transducer [146]. By this, a high efficiency and bandwidth can be achieved. Fore example, prototypes with a -6 dB fractional bandwidth exceeding 130% were reported in various studies [164, 165].

Typically, CMUT designs are based on micromachining techniques where polysilicon, silicon nitride and metal layers are deposited on top of a doped silicon substrate and etched [166]. An alternative approach to manufacture CMUTs was first published in 2006, where the membrane was made of a polymer instead of silicon nitride [167]. There, the lower stiffness of the polymer resulted in a significant increase in the maximum achievable deflection, promising higher sensitivities compared to nitride-based membranes.

In 2018, a research group led by Prof. Cretu and Prof. Rohling at the University of British Colombia (UBC) published a novel technological approach to produce highly sensitive polymer-based CMUTs (polyCMUTs). These transducers are mostly made from SU-8, a widely used epoxy-based photoresist, deposited on a silicon wafer. The production requires only six distinct processes, realizable with

relatively simple machinery. A schematic cross-section of a single cell produced with the technology from UBC is shown in Fig. 8.11a. In contrast to other polyCMUT designs (see e.g. [168]), the top electrode is directly integrated in the membrane and the cavity is vacuum sealed [169].

The design and production of the polyCMUTs from UBC result in a low quality factor and conversely, in a large bandwidth. Short distances between the bottom and top electrode can be achieved, effectively lowering the required DC bias for operation. Furthermore, the resulting transducers are less expensive and faster to produce, compared to silicon-based CMUTs. Figure 8.11b shows an array prototype with six column elements. There, each column-element consists of hundreds of cells connected in series.

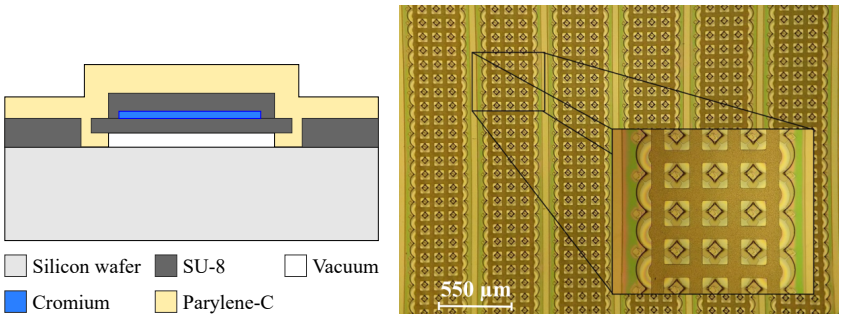

(a) Schematic cross section of a single cell.

(b) Picture of prototype with six column-elements consisting of hundreds of cells in series with a magnified view of 16 single cells.

Figure 8.11: PolyCMUT technology developed at UBC. Schematic cross section with the required layers and materials (a) and image of a produced prototype (b). Both, the schema and the picture were taken from [169].

Beyond the prospects of a higher opening angle, bandwidth and integration density, the polyCMUT technology might offers additional benefits to future 3D USCT designs. The manufacturing processes allows for fast and inexpensive prototyping and therefore, iterative refinements of the design. Supported by analytical and FE models, this leads to a time- and cost-efficient design optimization process to reach the respective requirements. In addition, the technology is capable of producing

fully flexible arrays, giving the possibility to directly form a semi-ellipsoidal aperture [170].

Future work will aim for more detailed analysis of the polyCMUTs technology. Quantitative measurements, similar to the PMUT characterization in Section 8.3, are planned to assess the suitability of the technology for its use in next generation 3D USCT devices.

8.5 Summary and Discussion

In this chapter, various transducer technologies are explored for their potential use in future 3D USCT devices. These technologies might overcome the fundamental limitations of the single-fiber piezocomposite technology in terms of bandwidth and opening angle. Three technologies were investigated in more detail. For two of them, first measurement results are presented.

Replacing PZT with a single-crystal piezoelectric material leads to an increase in fractional bandwidth and sensitivity by 35% and 86%, respectively. However, the PZT fibers cannot be replaced directly with single-crystals since the fabrication process is fundamentally different. The use of single-crystals would therefore require substantial changes in the manufacturing process and the general array design, but the expected gain justifies further work in this direction.

Prototypes were manufactured from AlN-based PMUT cells for acoustic characterization. Measuring the generated sound pressure was only possible when using the advanced measurement setup and the developed signal processing chain from Section 5.1. This enabled the characterization of the 3D acoustic field from single MUT cells for the first time, to the best knowledge of the author. The measurements showed that the opening angle of single PMUT cells exceeds 90°, with a peak sensitivity 45-times lower compared to the current design. Hence, multiple in series connected cells would be required to achieve acceptable sound pressures.

The accurate characterization of single cells allows for improving future FE models. The cells can then be integrated into larger simulations to predict the performance of an array. With these simulations, the resulting acoustic field of multiple cells can be investigated. One possible application is the study of spatially distributed and temporally controlled cells to generate arbitrary sound fields in 3D.

First evaluations on polymer-based CMUTs finalize this chapter. In this novel transducer fabrication technology, silicon-based layers are replaced with polymers. This promises a large bandwidth, fast prototyping, lower costs and more environmentally-friendly production. Quantitative evaluations will be conducted in the future to further explore the suitability for 3D USCT.

9 Conclusion

The central aim of this thesis was the production of ultrasound transducer arrays (TAS III) to enable clinical tests with two 3D USCT III devices. These devices are prototypes of a new and promising medical imaging method for breast cancer detection, facilitating ultrasound scanning in full 3D. The 3D USCT concept allows for simultaneous transmission and reflection imaging, leading to a high specificity in detecting cancerous tissue [16]. However, extensive testing is required to prove the applicability in clinical practice. The transducer arrays are among the most critical and technologically challenging components of the device. They have to enable pseudo-random positioning of single transducers, exhibit high bandwidths, large opening angles, isotropic sound emissions and comply with medical device regulations. These requirements deviate significantly from existing ultrasound applications, leading to the necessity of a custom design. Since each 3D USCT III devices holds 128 arrays, reliable and repeatable manufacturing processes are required.

Production of the TAS III

The central aim of this thesis was achieved. Transducer arrays were produced for integration in two 3D USCT III devices. The core element of the new design are piezocomposite disks, where 18 single PZT fibers are pseudo-randomly positioned in polymer. The arrays are finalized by attaching an acoustic matching disk to the front and a PCB to the rear. The PCB provides space for adding acoustic backing material which dampens the vibrations and thus increases the bandwidth. A semi-automated manufacturing process was developed using automated printing and pick-and-place processes. To speed up manufacturing, batch production

techniques were applied for simultaneous processing of 16 arrays. These techniques enable easy scaling for possible future industrialization of the 3D USCT technology.

The produced arrays showed high quality. This was evaluated using a developed statistical quality control method based on electrical impedance measurements. More than 96% of the produced transducers passed the quantitative evaluation, proving the manufacturing process well-suited. Even higher yields are achievable with minor design adjustments and stricter incoming inspections. Reliability tests identified a temperature range for safe operation from 10°C to 55°C. These tests also showed that high temperature gradients can cause damage when the temperature drops below 4°C. CT scans suggest a weakness in connecting the PZT fibers. This weakness can be addressed by design adjustments for future batches.

Characterization and design analysis
Before integrating the transducer arrays in the 3D USCT system, the performance was characterized. Most of the defined requirements were met. Ultrasound measurements in 3D showed that single transducers generate isotropic acoustic fields. The statistical analysis of 54 measured transducer showed a very high fractional bandwidth of 134%, with a center frequency of 2.6 MHz. Deviations from the requirements were found in the lower frequency limit f_l, with 1.7 MHz instead of the aimed 0.5 MHz, and the opening angle Φ_t, with 42.8° instead of 60°. The effects of these deviations are mitigated in the 3D USCT system due to the high parallelization of the imaging channels and the pseudo-random transducer positioning.

The transducer behavior was modeled in order to analyze measured effects in detail and to identify possible design improvements. The modeling concept is based on equivalent circuit methods and finite element analyses. Initial differences between the measured characteristics and model predictions were addressed by applying complex parameter fitting techniques and considering realistic material damping derived from measurement. This resulted in a high prediction accuracy (15% for most characteristics) over a wide range of emission angles and frequencies.

Performance improvements were found when increasing the thickness and radius of the PZT fiber by 120 µm and 50 µm, respectively. Moreover, the thickness of the matching layer should be reduced by 150 µm, and the mechanical damping of the piezocomposite material increased. This shifts the lower frequency limit f_l down by 0.5 MHz, enlarges the opening angle Φ_t by 4°, increases the peak sensitivity by 59%, but reduces the bandwidth by 31%. Thus, the extent of the achievable improvements is limited, since enhancing one characteristic entails trade-offs that largely negate the achievable gain. This leads to the conclusion that the TAS III design is already close to the achievable optimum. Substantial performance improvements would therefore require a change in the utilized transducer technology.

Alternative transducer technologies
Investigations in transducer technologies other than PZT fiber composites were conducted. These were aimed to explore the achievable performance improvements and limitations of future transducer array designs. Measurements on prototypes made of single-crystal piezoelectric materials showed a substantial increase in bandwidth (+35%) and sensitivity (+86%). However, single-crystals cannot directly replace the PZT fibers due to differences in fabrication of the material. Hence, a profound redesign would be required to realize suitable arrays.

Micromachined ultrasound transducers (MUTs) are an emerging technology, differing from bulk piezos in the manufacturing process, dimensions and vibration mode. Prototypes were manufactured from single piezoelectric MUT cells for characterization. Measuring the very low sound pressure (less than 10 Pa) generated by these transducers was only possible after developing an advanced signal processing chain. The measurements showed opening angles exceeding 90°, but a 45 times lower sensitivity. Hence, larger arrays are required to achieve adequate sound pressures. Nevertheless, the general transducer properties, novel fabrication techniques (e.g. polymer-based transducers) and the design freedom of microfabrication make MUTs very promising for future 3D USCT devices.

Application and outlook
Two 3D USCT III devices were equipped with the produced TAS III. Currently,

extensive system and imaging tests are being performed on phantoms and volunteers. Preliminary analyses show promising results with better image quality and significantly less artifacts compared to the previous 3D USCT generation. This is directly related to the increased frequency bandwidth and the pseudo-random positioning of the transducers in the arrays. A larger clinical study will be conducted in the near future to evaluate the sensitivity and specificity of the 3D USCT medical imaging technology. If proven save and effective, the developed transducer arrays contribute significantly to the realization of a novel, harmless and cost-effective method for breast cancer screening.

Transducer requirements for ultrasound imaging applications are subject to ongoing adjustments and changes. These arise from new scientific findings, novel image reconstruction techniques and design changes. The modeling, production, characterization and optimization methods developed in this work can greatly assist in the design of ultrasound transducer arrays for future imaging applications.

A Appendix

A.1 Calculation Scheme of Analytical Model

This addendum explains the developed analytical transducer model in detail. The equations and parameters needed to set up the model are given in the this section and the tables in Section A.2. More details on how the KLM model is derived can be found in [116, 117, 120, 171].

The equivalent circuit depicted in Fig. 6.2 can be reduced to a 2-port transmission (or ABCD) matrix with U_{in} and I_{in} as input variables, and F_{out} and $-v_{out}$ as output variables. The EM coupling is based on voltage-to-force conversion [115]. The 2-port formalism of transmission matrices enables the division of the model into arbitrary 2x2 matrices, with the possibility of direct concatenation in series or in parallel. Applying this to the analytical model results in the block diagram shown in Fig. A.1.

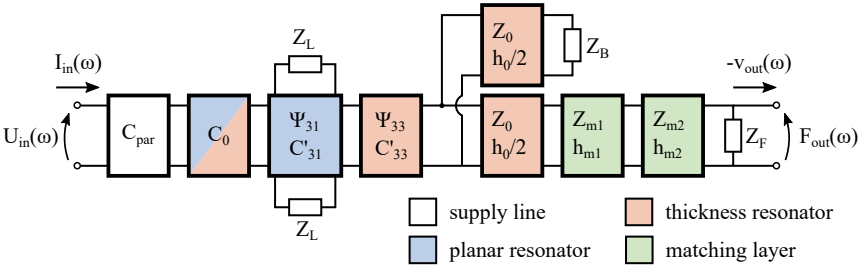

Figure A.1: Block diagram of analytical transducer model covering parasitic elements in the supply line, two spatial dimensions (planar and thickness resonator) and two matching layers.

The block diagram reflects the individual 2x2 transfer matrices based on the components in the equivalent circuit. With the first block, a parasitic capacitance C_{par}, likely present in the supply line, is considered. The next block is the blocking capacitance C_0, calculated according to Eq. A.1. There, ϵ_{33}^S is the absolute permittivity at constant strain, $A_0 = r_0^2\pi$ the electrode surface area and h_0 the thickness of the piezoceramic. Dielectric losses are considered by adding the imaginary part $j\tan(\delta)$ [118].

$$C_0 = \epsilon_{33}^S(1 - j\tan(\delta)) \cdot \frac{A_0}{h_0} \tag{A.1}$$

The next block covers the planar or lateral resonator and is modeled with a transformer coupled to the center of a transmission line. This transmission line is terminated at both ends with Z_L. The transformer ratio of the planar conversion Ψ_{31} is given by Eq. A.2, where k_{31} is the EM coupling in shear direction, r is the radius of the piezoceramic, v_p the planar or shear speed of sound and Z_0 the acoustic impedance of the piezoceramic. The shear speed of sound is calculated analog to Eq. 2.12 by $v_p = \sqrt{c_{11}^D/\rho_0}$, where c_{11}^D is the planar compliance at constant dielectric displacement and ρ_0 the piezoceramic's density.

$$\Psi_{31}(\omega) = k_{31} \cdot \sqrt{\frac{2r}{v_p C_0 Z_0}} \cdot \mathrm{sinc}(\omega/2\omega_p) \quad \text{with} \quad \omega_p = \pi v_p/r \tag{A.2}$$

When modeling the EM conversion with a transformer, an additional reactance must be added to address the capacitive behavior of the piezoceramic at the output. In the KLM model, this reactance is transformed to the primary side, resulting in the negative capacitance C'_{31} in series [120]. This capacitance is calculated according to Eq. A.3.

$$C'_{31}(\omega) = \frac{-C_0}{k_{31}^2 \cdot \mathrm{sinc}(\omega/\omega_p)} \tag{A.3}$$

In order to finalize the planar resonator, the acoustic impedance of the lateral material (for the TAS III the filler material) is transferred to the center of a transmission line modeling lateral vibrations. According to transmission line theory, this is possible via Eq. A.4 [172, chp. 2]. There, $Z_p = v_p \rho_0$ is the planar acoustic impedance of the piezoceramic, $A_p = \pi r_0 h_0$ the planar surface in contact with the filler material and Z_L it's acoustic impedance. Mechanical losses in the piezoceramic are considered by the complex propagation constant γ_p, where α_0 is the attenuation coefficient (in 1/m) and $\beta_p = \omega / v_p$ is the wavenumber of the planar transmission line [119].

$$Z_{PB}(\omega) = Z_p A_p \cdot \frac{Z_L + Z_p \tanh(\gamma_p r_0)}{Z_p + Z_L \tanh(\gamma_p r_0)} \quad \text{with} \quad \gamma_p = \beta_p(\alpha_0 r_0 + j) \tag{A.4}$$

The next block in Fig. A.1 models the thickness or axial resonator. Analog to the planar mode, a transformer with the frequency dependent turns ratio Ψ_{33} is coupled to the center of a transmission line. This transmission line exhibits a length equal to the thickness h_0 of the piezoceramic. The reactance C'_{33} is given by Eq. A.6, while v_t is the speed of sound in thickness or longitudinal direction.

$$\Psi_{33}(\omega) = k_{33} \cdot \sqrt{\frac{h_0}{v_t C_0 Z_0}} \cdot \operatorname{sinc}(\omega / 2\omega_t) \quad \text{with} \quad \omega_t = \pi v_t / h_0 \tag{A.5}$$

$$C'_{33}(\omega) = \frac{-C_0}{k_{33}^2 \cdot \operatorname{sinc}(\omega / \omega_t)} \tag{A.6}$$

The acoustic impedance Z_B of the backing material is transferred to the center of the thickness transmission line according to Eq. A.7. This now allows for propagation of the state variables U_{in} and I_{in}, or more specifically F_{out} and $-v_{out}$, towards the output at the front end of the transducer.

$$Z_{TB}(\omega) = Z_0 A_0 \cdot \frac{Z_B + Z_0 \tanh(\gamma_0 h_0/2)}{Z_0 + Z_B \tanh(\gamma_0 h_0/2)} \quad \text{with} \quad \gamma_0 = \beta_0(\alpha_0 h_0 + j) \tag{A.7}$$

With the presented formulas, a 2x2 transmission matrix can be defined for each block as a series or parallel impedance [173]. Mathematically, they are concatenated by matrix multiplication. Equation A.8 shows the 2x2 matrices for the equivalent circuit components to obtain the frequency dependent ABCD or transmission parameters of the entire model.

In Eq. A.8, he latter three 2x2 matrices in Eq. A.8 are the transmission lines of the piezoceramic's front-half and two matching layers. For the matching layers, denoted by the indices $_{m1}$ and $_{m2}$, the acoustic properties and the complex propagation constant γ are calculated analog to those of the piezoceramic.

$$\begin{aligned} T(\omega) = \begin{bmatrix} A(\omega) & B(\omega) \\ C(\omega) & D(\omega) \end{bmatrix} &= \begin{bmatrix} 1 & 0 \\ j\omega C_{par} & 1 \end{bmatrix} \cdot \begin{bmatrix} 1 & 1/j\omega C_0 + 1/j\omega C'_{31}(\omega) \\ 0 & 1 \end{bmatrix} \\ &\cdot \begin{bmatrix} 1 & \Psi_{31}(\omega)^2 \cdot Z_{PB}(\omega)/2 \\ 0 & 1 \end{bmatrix} \cdot \begin{bmatrix} 1 & 1/j\omega C'_{33}(\omega) \\ 0 & 1 \end{bmatrix} \\ &\cdot \begin{bmatrix} \Psi_{33}(\omega) & 0 \\ 1/(Z_{TB}(\omega) \cdot \Psi_{33}(\omega)) & 1/\Psi_{33}(\omega) \end{bmatrix} \\ &\cdot \begin{bmatrix} \cosh(\gamma_0 h_0/2) & Z_0 A_0 \cdot \sinh(\gamma_0 h_0/2) \\ 1/(Z_0 A_0) \cdot \sinh(\gamma_0 h_0/2) & \cosh(\gamma_0 h_0/2) \end{bmatrix} \\ &\cdot \begin{bmatrix} \cosh(\gamma_{m1} h_{m1}) & Z_{m1} A_0 \cdot \sinh(\gamma_{m1} h_{m1}) \\ 1/(Z_{m1} A_0) \cdot \sinh(\gamma_{m1} h_{m1}) & \cosh(\gamma_{m1} h_{m1}) \end{bmatrix} \\ &\cdot \begin{bmatrix} \cosh(\gamma_{m2} h_{m2}) & h_{m2} A_0 \cdot \sinh(\gamma_{m2} h_{m2}) \\ 1/(h_{m2} A_0) \cdot \sinh(\gamma_{m2} h_{m2}) & \sinh(\gamma_{m2} h_{m2}) \end{bmatrix} \end{aligned} \tag{A.8}$$

A.2 Tables with Material Parameters

Table A.1: Full parameter set of 2D KLM model for the TAS III design. The basic literature parameters as well as those for the best fit are given separately. For each parameter a rational is added.

Parameter	Unit	Literature	Best fit	Rational
s_{33}^E	10^{-12} m^2/N	24	25.1	from [122]
s_{11}^E	10^{-12} m^2/N	17.9	15.8	from [122]
c_{33}^D	10^{10} N/m^2	14.7	10.2	Eq. 2.10
c_{11}^D	10^{10} N/m^2	16.3	13.3	Eq. 2.10
ϵ_{11}^T		1850	1850	from [122]
ϵ_{33}^T		1880	1880	from [122]
ϵ_{11}^S		917	917	Eq. 2.9
ϵ_{33}^S		783	783	Eq. 2.9
k_{33}		0.73	0.65	from [122]
k_{31}		0.33	0.20	from [122]
$\tan(\delta)$		0.02	0.02	from [122]
h_0	mm	0.62	0.62	measurement
r_0	mm	0.225	0.225	measurement
ρ_0	kg/m^3	7700	7700	from [122]
v_t	m/s	4366	3629	Eq. 2.12
v_p	m/s	4599	4152	Eq. 2.12
α_0	1/m	6.28	6.28	from [119]
Z_0	MPa · s/m	33.6	27.9	Eq. 2.13
Z_P	MPa · s/m	35.4	32.0	Eq. 2.13
Z_B	MPa · s/m	0.0004	2.35	from [3]
Z_L	MPa · s/m	2.95	2.95	from [86]
Z_F	MPa · s/m	0.0004	0.0004	from [125]
Z_S	Ω	50	50	chosen
C_{par}	pF	0.0	0.3	from [3]

Table A.2: Piezoelectric constants of FE model for TAS III composite from literature and after fitting.

Parameter	Unit	Literature	Fitted	Rational
k_p		0.65	0.61	from [122]
k_{51}		0.71	0.67	from [122]
s_{11}^E	10^{-12} m^2/N	17.9	17.0	from [122]
s_{12}^E	10^{-12} m^2/N	-8.69	-5.28	Eq. 2.7
s_{13}^E	10^{10} N/m^2	-8.26	-7.85	Eq. 2.8
s_{33}^E	10^{10} N/m^2	24.0	17.1	[122]
s_{55}^E	10^{10} N/m^2	54.4	61.5	Eq. 2.6
s_{66}^E	10^{10} N/m^2	53.2	44.6	Eq. 2.3
ϵ_{11}^T		1850	1850	from [122]
ϵ_{33}^T		1880	1880	from [122]
d_{31}	10^{-12} C/N	-180	-191	from [122]
d_{33}	10^{-12} C/N	475	447	from [122]
d_{15}	10^{-12} C/N	670	670	from [122]
ρ_0	kg/m^3	7700	6930	from [122]
η_0		0.012	0.012	from [122]

Table A.3: FE model parameters of passive materials for TAS III design with values from literature and adjusted for improving the prediction accuracy.

Parameter	Unit	Literature	Adjusted	Rational
Filler/ADH-2 (EpoTek 301-2, Epoxy Technologies)				
E_{adh}	GPa	2.98	3.58	data sheet
ρ_{adh}	kg/m^3	1158		from [86]
ν_{adh}		0.32		from [174]
η_{adh}		0.3	*$0.25/2.5\text{E}6 \cdot f^{1.17}$	[4]
Matching layer (TMM4, Rogers Corp)				
E_{ml}	GPa	12.13		data sheet
ρ_{ml}	kg/m^3	2036		measured
ν_{ml}		0.4		model fit**
η_{ml}		0.3	0.2	estimated
Acoustic backing (see Sec. 3.3.4)				
E_b	GPa	4.34		from [86]
ρ_b	kg/m^3	3735		from [86]
ν_b		0.41		from [175]
η_b		1.2	$0.84/1.1\text{E}6 \cdot f^{1.39}$	[4]
PCB (FR4)				
E_{pcb}	GPa	22		COMSOL library
ρ_{pcb}	kg/m^3	1900		COMSOL library
ν_{pcb}		0.15		COMSOL library
PU (Thermoplast, glass filled)				
E_{pu}	GPa	2.58		from [143]
ρ_{pu}	kg/m^3	1450		from [143]
ν_{pu}		0.41		from [143]
η_{pu}		n.d.	$0.4/1.1\text{E}6 \cdot f^{1.39}$	assumed

*Expression for frequency dependent evaluation

**KLM model fit on test transducers

Table A.4: Parameter set of the 1D KLM model used for the performance prediction of the single-crystal test transducer.

Parameter	Unit	Value	Rational
s_{33}^E	10^{-12} m^2/N	11.9	from [152]
c_{33}^D	10^{10} N/m^2	8.40	Eq. 2.10
ϵ_{33}^T		5507	from [152]
ϵ_{33}^S		858	Eq. 8.1
r_0	mm	3	measurement
h_0	mm	0.44	measurement
a_f		0.6	from supplier
k_t		0.75	from supplier
k_{33}		0.89	from [152]
k_{31}		0.50	from [152]
ρ_0	kg/m^3	8000	from [152]
v_t	m/s	3241	Eq. 2.12
α_0	1/m	6.28	from [119]
Z_0	MPa · s/m	25.9	Eq. 2.13
Z_B	MPa · s/m	8.00	assumed
Z_F	MPa · s/m	1.5	from [125]
Z_S	Ω	50	chosen
Matching layer 1 (EpoTek EJ2189-LV, Epoxy Technologies)			
h_{m1}	µm	50	measurement
v_{m1}	m/s	1900	from [123]
Z_{m1}	MPa · s/m	5.14	from [123]
α_{m1}	1/m	1600	from [123]
Matching layer 2 (TMM4, Rogers Corp)			
h_{m2}	µm	422	measurement
v_{m2}	m/s	3280	measurement
Z_{m2}	MPa · s/m	6.40	from [76]
α_{m2}	1/m	20	assumed

A.3 Student Supervision

Supervision of Julia Koppenhöfer, who studied Physics at KIT. She finished her Master thesis with the title: “Measurement Environment for Acoustic Material Properties for Ultrasound Computed Tomography” in September 2020.

Supervision of Aritra Das, who studied Sensor Technologies at the University of Applied Sciences, Coburg. He finished his Master thesis in October 2021 with the title: “Characterization and finite element modeling of piezoelectric micromachined transducers.”

Supervision of Felix Schuderer, who studied Electrical Engineering at the KIT. From April 2021, he worked as research assistant in the 3D USCT group on the “Evaluation of single crystal piezoceramics used for ultrasound transducers.”

Acronyms and Symbols

Acronyms

ADH-1	EJ2189-LV, Epoxy Technology, Billerica, USA
ADH-2	E301-2, Epoxy Technology, Billerica, USA
ADH-3	OG116, Epoxy Technology, Billerica, USA
ADH-4	BondIt B-45, Reltec LLC., Santa Rosa, USA
AWG	Arbitrary Waveform Generator
CAD	Computer-Aided Design
CMUT	Capacitive Micromachined Ultrasound Transducer
CNC	Computerized Numerical Control
DUT	Device Under Test
ECM	Equivalent Circuit Model
EM	Electromechanical
EMI	Electromechanical Impedance
FASP	Frequency- and Angle-dependent Sound Pressure
GUI	Graphical User Interface

KIT	Karlsruhe Institute of Technology
MUT	Micromachined Ultrasound Transducer
OVL	Overlapping Coefficient
PDF	Probability Density Function
PDMS	Polydimethylsiloxan
PMUT	Piezoelectric Micromachined Ultrasound Transducer
PU	Polyurethane
ROI	Region of Interest
RPM	Revolutions Per Minute
SNR	Signal to Noise Ratio
TAS	Transducer Array System
TAS-3	Third generation Transducer Array System
USCT	Ultrasound Computed Tomography
USCT-3	Third generation of the 3D USCT device
UAB	Autonomous University of Barcelona
UBC	University of British Columbia

Variables

A	[m^2]	Area of piezoelectric material
bw_{el}	[Hz]	Bandwidth of electrical input power

bw_{us}	[%]	Fractional bandwidth of ultrasound emission
c^D	[N/m^2]	Mechanical stiffness at constant dielectric displacement
C	[F]	Capacitance
d	[C/N]	Piezoelectric charge constant
E	[Pa]	Elastic modulus
f	[Hz]	Frequency
f_c	[Hz]	Center frequency of a transducer
f_l	[Hz]	Lower functional frequency limit of a transducer
f_u	[Hz]	Upper functional frequency limit of a transducer
f_c	[Hz]	Center frequency
h	[m]	Heigth or thickness
k		Electromechanical coupling factor
r	[m]	Radius
s^E	[m^2/N]	Mechanical compliance at constant E-field
S	[Pa/V]	Ultrasound emission sensitivity
S_c	[Pa/V]	Sensitivity of ultrasound transducer at the center frequency
t	[s]	Time
$\tan(\delta)$		Dissipation factor
T	[°C]	Temperature
v	[m/s]	Velocity of sound wave

Z	[MPa · s/m]	Acoustic impedance (also in MRayl)
α	[1/m]	Attenuation coefficient
β	[1/m]	Phase propagation constant
γ	[1/m]	Complex propagation constant
Γ	[°]	Angular range of measurement
ϵ^T		Absolute permittivity at constant stress
η		Loss factor
λ	[m]	Wavelength
ν		Poisson's ratio
ρ	[kg/m^3]	Density
φ	[°]	Phase angle of electromechanical impedance
Φ	[°]	Angle of ultrasound emission
Φ_t	[°]	Opening angle of transducer
Ψ		Turns ratio of transformer
ω	[rad]	Angular frequency

List of Figures

1.1 Third generation 3D USCT device at KIT 3
1.2 Simplified measurement principle of the 3D USCT imaging approach 4

2.1 Typical structure of a ultrasound transducer and common vibration modes 14
2.2 Example of dice-and-fill approach 14
2.3 Functional ultrasound characteristics 20
2.4 Three groups of USCT imaging concepts 21

3.1 First USCT prototype systems at KIT 26
3.2 Transducer design of TAS II 27
3.3 Investigated transducer technologies after study results with 3D USCT II 28
3.4 Intermediate transducer design TAS IIb to evaluate the single-fiber piezocomposite technology 29
3.5 Explosion view of the TAS III design 32
3.6 Schematic cross section of a single TAS III transducer 33
3.7 Single-fiber piezocomposite disk of TAS III 34
3.8 PCB disk of TAS III design 35
3.9 Matching disk of TAS III design 36
3.10 Recipe for mixing acoustic backing material 37
3.11 Process flowchart of TAS III 39
3.12 Fixtures used for the batch production of TAS III 42
3.13 Peeling tests of a composite disk to evaluate electrode adhesion 43
3.14 Conductive connection of PCBs and composite disks 45
3.15 GND connection of piezocomposite disks 46
3.16 Connection of matching disks with the composite disks 46

3.17 Stack finalization by dispensing the acoustic backing 47
3.18 Integration of the TAS III stack in the housing 48
3.19 Sealing of the TAS III stack in the housing 49
3.20 Finalized TAS III 50

4.1 Exemplary EMI measurement of one TAS III transducer 55
4.2 Schematic depiction of possible fabrication defects 56
4.3 Five manufacturing states where EMI measurements were conducted . 57
4.4 Histograms of two EMI characteristics obtained from the TAS III . . 60
4.5 Graphical example of how to derive the OVL 60
4.6 Results of quality control measure to find the best suited EMI characteristic 61
4.7 Histograms and estimated PDFs of $\mathrm{bw}_{\mathrm{el}}$ 63
4.8 Applied quality control measure on one full set of TAS III 64
4.9 Conducted temperature cycling tests 65
4.10 Results of temperature cycling test according to IEC 60601 66
4.11 Results of second temperature cycling test 68
4.12 3D micro-CT scan of a finalized TAS III array 70
4.13 Detected gaps from micro-CT scans of TAS III 71

5.1 Ultrasound test setup for transducer characterization 74
5.2 Block diagram of the ultrasound measurement setup 75
5.3 Excitation signal for transducer characterization 76
5.4 Illustration of time windowing on an exemplary measurement 77
5.5 Signal processing chain to obtain the complex frequency response of a transducer with high SNR 78
5.6 Impulse response magnitude of an exemplary transducer measured over a 120° circular segment at 10 cm distance with characteristic time delays caused by the measurement setup. 79
5.7 Exemplary delta functions at distinct times of flight in the time and frequency domain 80
5.8 Detected maximum amplitude of a measured ultrasound wave and a fitted idealized wave $\delta(\Phi, t)$ used for phase filtering 81
5.9 Measured ultrasound wave from Fig. 5.6 after applying the phase angle correction method. 82

5.10 3D ultrasound performance of a single TAS III transducer at two distinct frequencies 83
5.11 Ultrasound performance of a single TAS III transducer over a circular segment of 120° 85
5.12 Statistics on the transducer sensitivity and directivity of 54 TAS III transducers 87
5.13 Statistics of the functional ultrasound characteristics obtained from the characterization of 54 TAS III transducers. 88
5.14 Impact of TAS III characteristics on the ROI 91

6.1 Butterworth-van-Dyke ECM to model one-dimensional resonator . . 94
6.2 ECM of a transducer which considers two spatial dimensions and two matching layers on the front 96
6.3 2D KLM model reduced to a 2-port and terminated on both ends. . . 97
6.4 Model-to-measurement comparison of a transducer before the assembly (initial state) when using parameters from literature. 99
6.5 Results of a brute-force parameter sweep to obtain best-fit model parameters 101
6.6 Prediction of the FASP amplitude and phase angle using a simple analytical expression 103
6.7 FE model implemented as 2D shell including layer definitions and boundary conditions 105
6.8 FE model-to-measurement comparison of FASP amplitude over a circular segment of 120° at 10 cm axial distance 107
6.9 Impact of high and low structural loss factors on the modeled frequency response amplitude of a TAS III transducer. 109
6.10 Measured and modeled acoustic attenuation for two of the passive materials used for manufacturing the TAS III. 110
6.11 FE model to measurement comparison of the FASP amplitude over a circular segment of 120° at 10 cm axial distance after the parameter fit 113

7.1 Results of a parametric sweep using the 2D KLM model to obtain a reduction in center frequency by 0.5 MHz 119

7.2 Predicted changes in the frequency response amplitude and directivity when increasing h_0 and r_0 . . . 120
7.3 Impact on the opening angle Φ_t and the directivity when varying the elastic modulus E_{adh} . . . 121
7.4 Impact on the opening angle Φ_t and the overall directivity when varying the thickness h_{ml} . . . 122
7.5 Resulting directivity and FASP amplitude when adding a convex lens 124
7.6 Analysis of sensitivity fluctuations by applying different time windows to a measured impulse response . . . 125
7.7 Vibration behavior of a single TAS III transducer at two distinct frequencies showing bending of the piezoceramic fiber. . . . 126
7.8 Changes in the predicted impulse response with the FE model when varying the material of the filler. . . . 127
7.9 Predicted FASP amplitude and phase angle of the proposed transducer redesign . . . 129

8.1 Ultrasound transducer technologies based on microfabrication techniques (schemes adopted from [147]). . . . 132
8.2 Single-crystal piezoelectric materials . . . 133
8.3 Prototype transducers with single-crystal composites . . . 135
8.4 Measured and modeled FASP amplitude of single-crystal octagon test transducer . . . 136
8.5 Prototype of AlN PMUT designed at UAB . . . 138
8.6 Prototype transducers from PMUT samples after die and wire bonding 138
8.7 EMI characterization of PMUT samples using a manual needle prober 139
8.8 Processes to finalize the PMUT test transducers . . . 141
8.9 Measured and modeled FASP amplitude of a PMUT test transducer at 20 mm distance . . . 142
8.10 Surface depositions and FASP amplitude after applying a protective PDMS layer . . . 143
8.11 Polymer-based CMUT technology developed at UBC . . . 146

A.1 Block diagram of analytical transducer model covering parasitic elements in the supply line, two spatial dimensions (planar and thickness resonator) and two matching layers. . . . 153

List of Tables

2.1 Overview of USCT systems under investigation 22

3.1 Requirements for 3D USCT III transducers 31
3.2 Used adhesives for the production of the TAS III 40

4.1 Ten EMI characteristics for quantitative impedance evaluation 54
4.2 Classifiers for quality control of TAS III 62
4.3 Profiles for temperature cycling tests 67

5.1 Requirements vs. mean TAS III performance 90

6.1 Parameters to fit the 2D KLM model 101
6.2 Comparison of the initial FE model and measurement results 107
6.3 Coefficients of loss factor model 111
6.4 Comparison of the fitted FE model and exemplary measurement . . . 114

7.1 Recommended design adjustments to optimize the performance of the TAS III 128
7.2 Quantitative comparison of functional ultrasound characteristics for the redesign proposal 129

8.1 Functional ultrasound characteristics of tested PMUT transducers . . 144

A.1 TAS III parameters for 2D KLM model 158
A.2 TAS III piezoelectric constants for FE model 159
A.3 TAS III material parameters for FE model 160
A.4 Parameter set of KLM model for single-crystal test transducer 161

List of Publications

Journal articles

[1] M. Angerer, M. Zapf, B. Leyrer, and N. V. Ruiter, “Model-guided manufacturing of transducer arrays based on single-fibre piezocomposites,” *Appl. Sci.*, vol. 10, no. 4927, 2020.

Conference contributions

[2] M. Angerer, M. Zapf, S. Gebhardt, H. Neubert, and N. V. Ruiter, “Enhanced KLM model for single-fibre piezocomposite transducers,” in *Proceedings of 2020 IEEE Ultrasonics*, IEEE.

[3] M. Angerer, M. Zapf, B. Leyrer, and N. V. Ruiter, “Semi-automated packaging of transducer arrays for 3D ultrasound computer tomography,” in *Proceedings of 2020 IEEE Sensors*, IEEE.

[4] M. Angerer, M. Zapf, J. Koppenhöfer, and N. V. Ruiter, “Method to extract frequency dependent material attenuation for improved transducer models,” in *Proceedings of 2021 IEEE Ultrasonics*.

[5] M. Angerer, M. Zapf, M. Koch, and N. V. Ruiter, “Quality control of ultrasound transducers using distribution-free overlapping coefficients,” in *Proceedings of 2021 IEEE Sensors*, IEEE.

[6] M. Zapf, T. Hopp, H. Gemmeke, M. Angerer, Z. Lu, O. Molchanova, N. Rashvand, R. Blanco, P. Steck, B. Leyrer, D. Tcherniakhovski,

D. Bormann, K. Schlote-Holubek, and N. V. Ruiter, “Realization of an pseudo-randomly sampled 3D USCT,” in *Proceedings of 2022 SPIE*, vol. 12038.

[7] M. Angerer, M. Zapf, S. Gebhardt, and N. V. Ruiter, “Single-PZT-fiber transducers for 3D ultrasound computed tomography: Characterization and modeling,” in *Proceedings of 2022 IEEE Ultrasonics (accepted)*, IEEE.

Bibliography

[8] World Health Organisation, *World Cancer Report*. Cancer research for cancer prevention, 2020.

[9] European Commision, *Breast cancer incidence and mortality estimates 2020*. [https://ecis.jrc.ec.europa.eu/], Accessed on 02/2022.

[10] R. Sivaramakrishna and R. Gordon, "Detection of breast cancer at a smaller size can reduce the likelihood of metastatic spread: A quantitative analysis," *Academic Radiology*, vol. 4, no. 1, pp. 8–12, 1997.

[11] P. E. Freer, "Mammographic breast density: Impact on breast cancer risk and implications for screening," *RadioGraphics*, vol. 35, no. 2, pp. 302–315, 2015.

[12] R. M. Mann, C. K. Kuhl, and L. Moy, "Contrast enhanced MRI for breast cancer screening," *Journal of Magnetic Resonance Imaging*, vol. 50, no. 2, pp. 377–390, 2019.

[13] K. J. Murphy, J. A. Brunberg, and R. H. Cohan, "Adverse reactions to gadolinium contrast media: a review of 36 cases," *American Journal of Roentgenology*, vol. 167, no. 4, pp. 847–849, 1996.

[14] M. A. Perazella, "Gadolinium-contrast toxicity in patients with kidney disease: Nephrotoxicity and nephrogenic systemic fibrosis," *Current drug safety*, vol. 3, no. 1, p. 67–75, 2008.

[15] X. Ying, X. Lin, Y.and Xia, B. Hu, Z. Zhu, and P. He, "A comparison of mammography and ultrasound in women with breast disease: A receiver

operating characteristic analysis," *The Breast Journal*, vol. 18, no. 2, pp. 130–138, 2012.

[16] N. Duric, P. J. Littrup, O. Rama, and E. T. Holsapple, *Computerized ultrasound risk evaluation CURE: First clinical results*, vol. 28. Springer, Dordrecht, 2006.

[17] F. Greenleaf, A. Johnson, R. C. Bahn, and R. B., "Cross-sectional imaging of ultrasound parameters," in *1977 IEEE Ultrasonics Symposium Proc.*, p. 989–995.

[18] N. Duric, P. Littrup, L. Poulo, A. Babkin, R. Pevzner, E. Holsapple, O. Rama, and C. Glide, "Detection of breast cancer with ultrasound tomography: First results with the computed ultrasound risk evaluation (CURE) prototype," *Medical physics*, vol. 34, pp. 773–85, 2007.

[19] S. Atsuro, T. Yushi, T. Takahide, Y. Hiroko, K. Fumi, N. Mutsumi, S. Megumi, and K. Ken-ichi, "Optimized source estimation for full waveform inversion in ultrasound computed tomography," in *Proc.SPIE*, vol. 11602.

[20] K. J. Opieliński, P. Pruchnicki, T. Gudra, P. Podgórski, J. Kurcz, T. Krasnicki, M. Sasiadek, and J. Majewski, "Imaging results of multi-modal ultrasound computerized tomography system designed for breast diagnosis," *Computerized Medical Imaging and Graphics*, vol. 46, pp. 83–94, 2015.

[21] H. Gemmeke, L. Berger, T. Hopp, M. Zapf, W. Tan, R. Blanco, R. Leys, I. Peric, and N. V. Ruiter, "The new generation of the KIT 3D USCT," in *International Workshop on Medical Ultrasound Tomography*, vol. 1, pp. 271–281, KIT Scientific Publishing, 2018.

[22] N. Ruiter, *Dreidimensionale Ultraschall-Computertomographie: Vom Konzept zur klinischen Anwendung (German)*. Habilitation thesis, Karlsuhe Institute of Technology, 2016.

[23] R. Blanco, *Customized Integrated Circuits for Scientific and Medical Applications*. PhD thesis, Karlsruhe Institute of Technology, 2019.

[24] Z. Lu, R. Blanco, K. Schlote-Holubek, M. Zapf, H. Gemmeke, I. Perić, and N. V. Ruiter, "Novel front-end design with high-voltage transceiver asics for ultrasound computed tomography," in *2021 IEEE International Ultrasonics Symposium (IUS)*.

[25] A. Menshikov, M. Balzer, and M. Kleifges, "MTCA.4RTM Modulbasierend auf dem DRS-4 Capacitor Array," vol. 2015 of *DESY-PROC*, pp. 127–138, Verlag Deutsches Elektronen-Synchrotron, 2015.

[26] C. Calderon, D. Vilkomerson, R. Mezrich, K. F. Etzold, B. Kingsley, and M. Haskin, "Differences in the attenuation of ultrasound by normal, benign, and malignant breast tissue," *Journal of Clinical Ultrasound*, vol. 4, no. 4, pp. 249–254, 1976.

[27] R. Dapp, *Abbildungsmethoden für die Brust mit einem 3D-Ultraschall-Computertomographen (German)*. PhD thesis, Karlsruhe Institute of Technology, 2015.

[28] T. Hopp, F. Zuch, P. A. Comby, and N. V. Ruiter, "Fat ray ultrasound transmission tomography: preliminary experimental results with simulated data," in *2020 SPIE Medical Imaging*, vol. 11319, pp. 125–133.

[29] S. R. Doctor, T. E. Hall, and L. D. Reid, "SAFT — the evolution of a signal processing technology for ultrasonic testing," *NDT International*, vol. 19, no. 3, pp. 163–167, 1986.

[30] E. Kretzek, M. Zapf, M. Birk, H. Gemmeke, and N. V. Ruiter, "GPU based acceleration of 3D USCT image reconstruction with efficient integration into MATLAB," in *2013 SPIE Medical Imaging*, vol. 8675, pp. 196–205.

[31] N. V. Ruiter, M. Zapf, T. Hopp, R. Dapp, and H. Gemmeke, "Optimization of the aperture and the transducer characteristics of a 3D ultrasound computer tomography system," in *2014 Proceedings of SPIE*, vol. 9040.

[32] W. G. Cady, *Piezoelectricity*. New York: Dover Publications, 1 ed., 1964.

[33] D. Berlincourt, D. Curran, and H. Jaffe, *Piezomagnetic Materials and Their Function in Transducers*. New York: Academic, 1 ed., 1964.

[34] R. Newnham, *Properties of Materials*. Oxford: Oxford University Press, 2005.

[35] P. Curie and J. Curie, "Développement par compression de l'électricité polaire dans les cristaux hémièdres à faces inclinées (French)," *Bulletin de la Société minéralogique de France*, vol. 3, no. 4, 1880.

[36] J. L. Butler and H. H. Herman, *Transducers and Arrays for Underwater Sound*. Springer, 2 ed., 2016.

[37] "IRE standards on piezoelectric crystals: Measurements of piezoelectric ceramics, 1961," *Proceedings of the IRE*, vol. 49, no. 7, pp. 1161–1169, 1961.

[38] IEC 60483, *Guide to dynamic measurements of piezoelectric ceramics with high electromechanical coupling*. International Electrotechnical Commision, 1976.

[39] N. G. Fenu, N. Giles-Donovan, M. R. Sadiq, and S. Cochran, "Full set of material properties of lead-free PIC 700 for transducer designers," *IEEE Transactions on Ultrasonics, Ferroelectrics, and Frequency Control*, vol. 68, no. 5, pp. 1797–1807, 2021.

[40] G. Chevallier, S. Ghorbel, and A. Benjeddou, "A benchmark for free vibration and effective coupling of thick piezoelectric smart structures," *Smart Materials and Structures*, vol. 17, p. 065007, 2008.

[41] T. Scholehwar, *Charakterisierung der Struktur- Gefüge-Eigenschafts-beziehung von piezokeramischen Werkstoffen des Systems PZT/SKN (German)*. Doctoral thesis, 2010.

[42] ANSI Standard 176-1987, *IEEE Standard on Piezoelectricity*. IEEE, 1987.

[43] A. R. Selfridge, G. S. Kino, and B. T. Khuri-Yakub, “Fundamental concepts in acoustic transducer array design,” in *IEEE Ultrasonics Symposium*, pp. 989–993, 1980.

[44] J. Krautkrämer and H. Krautkrämer, *Werkstoffprüfung mit Ultraschall (German)*, vol. 5. Springer-Verlag Berlin Heidelberg, 1986.

[45] C. S. Desilets, J. D. Fraser, and G. S. Kino, “The design of efficient broad-band piezoelectric transducers,” *IEEE Transactions on Sonics and Ultrasonics*, vol. 25, no. 3, pp. 115–125, 1978.

[46] M. G. Silk, *Ultrasonic Transducers for Nondestructive Testing*. Bristol: Adam Hilger Ltd, 1984.

[47] S. Cochran, *Piezoelectricity and basic configurations for piezoelectric ultrasonic transducers*, book section 1. Cambridge, UK: Woodhead Publishing Limited, 2012.

[48] A. Safari, V. F. Janas, and A. Bandyopadhyay, “Development of fine-scale piezoelectric composites for transducers,” *AIChE Journal*, vol. 43, no. S11, pp. 2849–2856, 1997.

[49] A. Safari, “Development of piezoelectric composites for transducers,” *J. Phys. III France*, vol. 4, pp. 1129 – 1149, 1994.

[50] T. R. Gururaja and R. K. Panda, “Current status and future trends in ultrasonic transducers for medical imaging applications,” in *Proceedings of the Eleventh IEEE International Symposium on Applications of Ferroelectrics*, pp. 223–228.

[51] S. Rhee, T. A. Ritter, K. K. Shung, H. Wang, and W. Cao, “Materials for acoustic matching in ultrasound transducers,” in *IEEE Ultrasonics Symposium*, vol. 2, pp. 1051–1055, 2001.

[52] ISO 60601-1-2, *Medical electrical equipment – General requirements for basic safety and essential performance*. International Electrotechnical Commision, 2014.

[53] E. R. McKeighen, “Design guidelines for medical ultrasonic arrays,” in *Proceedings of SPIE*, vol. 3341, 1998.

[54] C. M. Sayers and C. E. Tait, “Ultrasonic properties of transducer backings,” *Ultrasonics*, vol. 22, pp. 57–60, 1984.

[55] R. Boubenia, E. Rosenkrantz, F. Despetis, P. Combette, and J. Y. Ferrandis, “Particulate metal composites as backing for ultrasonic transducers for continuous nondestructive measurements at moderate and high temperatures,” *IEEE Transactions on Ultrasonics, Ferroelectrics, and Frequency Control*, vol. 67, no. 10, pp. 2164–2175, 2020.

[56] Q. Zhou, K. H. Lam, H. Zheng, W. Qiu, and K. K. Shung, “Piezoelectric single crystal ultrasonic transducers for biomedical applications,” *Progress in Materials Science*, vol. 66, pp. 87–111, 2014.

[57] W. Haifeng, T. Ritter, C. Wenwu, and K. K. Shung, “High frequency properties of passive materials for ultrasonic transducers,” *IEEE Transactions on Ultrasonics, Ferroelectrics, and Frequency Control*, vol. 48, no. 1, pp. 78–84, 2001.

[58] G. F. Schwarzenberg, *Untersuchung der Abbildungseigenschaften eines 3D-Ultraschall-Computertomographen zur Berechnung der 3D-Abbildungsfunktion und Herleitung einer optimierten Sensorgeometrie (German)*. PhD thesis, Karlsruhe Institute of Technology, 2008.

[59] M. K. Feldman, S. Katyal, and M. S. Blackwood, “Us artifacts,” *RadioGraphics*, vol. 29, no. 4, pp. 1179–1189, 2009.

[60] N. Ruiter, G. Göbel, L. Berger, M. Zapf, and H. Gemmeke, “Realization of an optimized 3D USCT,” in *2011 Procceedings of SPIE*, vol. 7968.

[61] J. Rouyer, S. Mensah, E. Franceschini, P. Lasaygues, and J. P. Lefebvre, “Conformal ultrasound imaging system for anatomical breast inspection,” *IEEE Trans Ultrason Ferroelectr Freq Control*, vol. 59, no. 7, pp. 1457–69, 2012.

[62] D. Mingyue, S. Junjie, Z. Liang, W. Shanshan, and Y. Ming, "In vitro and in vivo evaluations of breast ultrasound tomography imaging system in hust," in *2018 Proc.SPIE*, vol. 10580.

[63] V. Z. Marmarelis, T.-S. Kim, and R. E. N. Shehada, "High-resolution ultrasonic transmission tomography," in *Medical Imaging 2003: Ultrasonic Imaging and Signal Processing*, vol. 5035, pp. 33–40, SPIE, 2003.

[64] L. Chang, X. Chenyang, C. Binzhen, G. Z., and H. Changde, "The application of an ultrasound tomography algorithm in a novel ring 3D ultrasound imaging system," *Sensors (Basel, Switzerland)*, vol. 18, no. 5, p. 1332, 2018.

[65] L. Chang, B. Zhang, X. Chenyang, Z. Wendong, Z. Guojun, and C. Yijun, "Multi-perspective ultrasound imaging technology of the breast with cylindrical motion of linear arrays," *Applied Sciences*, vol. 9, p. 419, 2019.

[66] N. Duric, P. Littrup, C. Li, O. Roy, S. Schmidt, R. Janer, X. Cheng, J. Goll, O. Rama, L. Bey-Knight, and W. Greenway, "Breast ultrasound tomography: Bridging the gap to clinical practice," *Progress in Biomedical Optics and Imaging - Proceedings of SPIE*, vol. 8320, p. 23, 2012.

[67] B. Malik, R. Terry, J. Wiskin, and M. Lenox, "Quantitative transmission ultrasound tomography: Imaging and performance characteristics," *Medical Physics*, vol. 45, no. 7, pp. 3063–3075, 2018.

[68] T. Gudra and K. J. Opielinski, "The ultrasonic probe for the investigating of internal object structure by ultrasound transmission tomography," *IEEE International Ultrasonics Symposium (IUS)*, vol. 44, pp. 679–683, 2006.

[69] M. André, J. Wiskin, and D. Borup, *Clinical Results with Ultrasound Computed Tomography of the Breast*, pp. 395–432. Springer Netherlands, 2013.

[70] B. Malik, E. Iuanow, and J. Klock, "An exploratory multi-reader, multi-case study comparing transmission ultrasound to mammography on recall rates and detection rates for breast cancer lesions," *Academic Radiology*, vol. 29, pp. S10–S18, 2022.

[71] N. V. Ruiter, M. Zapf, R. Dapp, T. Hopp, W. A. Kaiser, and H. Gemmeke, "First results of a clinical study with 3D ultrasound computer tomography," in *2013 IEEE International Ultrasonics Symposium (IUS)*, pp. 651–654.

[72] N. Duric, "The story of ultrasound tomography: A decades long journey from the bench to the clinic," in *Conference on Mathematics of Wave Phenomena*, February 14-18, 2022.

[73] G. Göbel, *Entwicklung von Ultraschallsensorarrays mit miniaturisierten Komponenten (German)*. Master thesis, University of Applied Sciences Karlsruhe, 2002.

[74] R. Stotzka, H. Widmann, T. Müller, K. Schlote-Holubek, H. Gemmeke, N. Ruiter, and G. Göbel, "Prototype of a new 3D ultrasound computer tomography system: Transducer design and data recording," *Proc SPIE Medical Imaging*, vol. 5373, pp. 70–79, 2004.

[75] H. Gemmeke and N. V. Ruiter, "3D ultrasound computer tomography for medical imaging," *Nuclear Instruments and Methods in Physics Research Section A: Accelerators, Spectrometers, Detectors and Associated Equipment*, vol. 580, no. 2, pp. 1057–1065, 2007.

[76] M. Zapf, P. Pfistner, C. I. Liberman, K. W. A. Van Dongen, B. Leyrer, H. Gemmeke, and N. V. Ruiter, "Dice-and-fill single element octagon transducers for next generation 3D USCT," in *International Workshop on Medical Ultrasound Tomography*, pp. 159–177, KIT Scientific Publishing, Karlsruhe, 2017.

[77] P. Pfistner, *Composite-based Ultrasound Transducers for a 3D Ultrasound Computer Tomograph*. Master thesis, Karlsruhe Institute of Technology, 2017.

[78] K. Hohlfeld, S. Gebhardt, A. Schönecker, and A. Michaelis, “PZT components derived from polysulphone spinning process,” *Advances in Applied Ceramics*, vol. 114, pp. 231–237, 2015.

[79] M. Zapf, K. Hohlfeld, N. V. Ruiter, P. Pfistner, K. W. A. van Dongen, H. Gemmeke, A. Michaelis, and S. E. Gebhardt, “Development of single-fiber piezocomposite transducers for 3D ultrasound computer tomography,” *Adv. Eng. Mater.*, vol. 20, 2018.

[80] J. F. Gelly and F. Lanteri, “Comparison of piezoelectric (thickness mode) and mems transducers,” in *IEEE Symposium on Ultrasonics, 2003*, vol. 2, pp. 1965–1974 Vol.2, 2003.

[81] N. Felix, L. Ratsimandresy, and L. Dufait, “High bandwidth, high density arrays for advanced ultrasound imaging,” in *2001 IEEE Ultrasonics Symposium. Proceedings. An International Symposium*, pp. 1123–1126.

[82] H. Fang, Z. Qiu, A. J. Mulholland, R. L. O’Leary, and A. Gachagan, “Broadband 1–3 piezoelectric composite transducer design using sierpinski gasket fractal geometry,” *IEEE Transactions on Ultrasonics, Ferroelectrics, and Frequency Control*, vol. 65, no. 12, pp. 2429–2439, 2018.

[83] H. Gemmeke, L. Althaus, K. W. A. v. Dongen, H. Egger, J. Hesser, J. Mayer, N. V. Ruiter, M. Zapf, and T. Hopp, “Wave equation based transmission tomography,” in *2016 IEEE International Ultrasonics Symposium (IUS)*, pp. 1–4.

[84] S. E. Gebhardt, K. Hohlfeld, P. Günther, and H. Neubert, “Manufacturing technologies for ultrasonic transducers in a broad frequency range,” in *International Workshop on Medical Ultrasound Tomography*, (Speyer), pp. 147–158, 2017.

[85] M. Zapf, K. Hohlfeld, G. Shah, S. Gebhardt, K. W. A. Van Dongen, H. Gemmeke, A. Michaelis, and N. V. Ruiter, “Evaluation of piezo composite based omnidirectional single fibre transducers for 3D USCT,” in *IEEE International Ultrasonics Symposium (IUS)*, IEEE, 2015.

[86] J. Koppenhöfer, *Measurement Environment for Acoustic Material Properties for Ultrasound Computed Tomography*. Master Thesis, Karlsruhe Institute of Technology, 2020.

[87] Epoxy Technology, "Tech tipp 13: Surface preparation," report, 2015.

[88] P. Savolainen, "Failure modes in conductive adhesives," report, DfR Solutions, 2021.

[89] Epoxy Technology, "Tech tipp 3: Viscosity and thixotropic index," report, 2015.

[90] G. Park and D. J. Inman, "Structural health monitoring using piezoelectric impedance measurements," *Philosophical Transactions of the Royal Society A: Mathematical, Physical and Engineering Sciences*, vol. 365, no. 1851, pp. 373–392, 2007.

[91] APC International Ltd., *Piezoelectric Ceramics: Principles and Applications*. APC International, 2011.

[92] Keysight Technologies, "Impedance measurement handbook 6th edition," report, Keysight Technologies, 2020.

[93] M. Bonamente, *Statistics and Analysis of Scientific Data*. Springer New York, 2nd ed., 2017.

[94] J. L. Devore, *Modern Mathematical Statistics with Applications*. Springer International Publishing, 3rd ed., 2021.

[95] S. G. Walker, "A new measure of overlap: An alternative to the p–value," *Preprint*, [https://arxiv.org/abs/2106.01821], 2021.

[96] N. Altman and M. Krzywinski, "P values and the search for significance," *Nature Methods*, vol. 14, no. 1, pp. 3–4, 2017.

[97] H. F. Inman and E. L. Bradley, "The overlapping coefficient as a measure of agreement between probability distributions and point estimation of the overlap of two normal densities," *Communications in Statistics - Theory and Methods*, vol. 18, no. 10, pp. 3851–3874, 1989.

[98] B. W. Silvermann, *Density Estimation for Statistics and Data Analysis*. Chapman and Hall, 1986.

[99] M. Pastore and A. Calcagnì, "Measuring distribution similarities between samples: A distribution-free overlapping index," *Frontiers in Psychology*, vol. 10, 2019.

[100] M. Pastore, "Overlapping: a R package for estimating overlapping in empirical distributions," *Journal of Open Source Software*, vol. 3, no. 32, p. 1023, 2018.

[101] H. Aguinis, R. K. Gottfredson, and H. Joo, "Best-practice recommendations for defining, identifying, and handling outliers," *Organizational Research Methods*, vol. 16, no. 2, pp. 270–301, 2013.

[102] B. Rosner, "Percentage points for a generalized ESD many-outlier procedure," *Technometrics*, vol. 25, no. 2, p. 165, 1983.

[103] Linear Technology Cooperation, "Datasheet lt6233 rev. c," report, 2022.

[104] S. Kraft, "Architectural rework of instrumentation software for automated characterization of ultrasound transducers," report, Karlsruhe Institute of Technology, 2021.

[105] M. O'Donnell, "Coded excitation system for improving the penetration of real-time phased-array imaging systems," *IEEE Transactions on Ultrasonics, Ferroelectrics, and Frequency Control*, vol. 39, no. 3, pp. 341–351, 1992.

[106] G. Turin, "An introduction to matched filters," *IEEE Transactions on Information Theory*, vol. 6, no. 3, pp. 311–329, 1960.

[107] A. Mertins, *Signaltheorie (German)*. Springer, 2nd ed., 2013.

[108] R. Y. Chiao and H. Xiaohui, "Coded excitation for diagnostic ultrasound: a system developer's perspective," vol. 52, no. 2, pp. 160–170, 2005.

[109] J. A. Jensen, S. I. Nikolov, K. L. Gammelmark, and M. H. Pedersen, "Synthetic aperture ultrasound imaging," *Ultrasonics*, vol. 44, pp. e5–e15, 2006.

[110] U. Taskin, *Full-Waveform Inversion for Breast Ultrasound.* PhD thesis, Delft University of Technology, 2021.

[111] O. Warshavski, C. Meynier, N. Sénégond, P. Chatain, J. Rebling, D. R. Razansky, N. Felix, and A. Nguyen-Dinh, "Experimental evaluation of cMUT and PZT transducers in receive only mode for photoacoustic imaging," in *2016 Proc.SPIE*, vol. 9708.

[112] S. Cochran, C. Demore, and C. Courtney, *Modelling ultrasonic transducer performance: One-dimensional models*, pp. 187–219. Woodhead Publishing, 2012.

[113] S. Butterworth, "On electrically-maintained vibrations," *Proceedings of the Physical Society of London*, vol. 27, no. 1, pp. 410–424, 1914.

[114] K. S. Van Dyke, "The piezo-electric resonator and its equivalent network," *Proceedings of the Institute of Radio Engineers*, vol. 16, no. 6, pp. 742–764, 1928.

[115] A. Lenk, R. Ballas, and W. G., *Electromechanical Systems in Microtechnology and Mechatronics*. Springer Nature, 2011.

[116] R. Krimholtz, D. A. Leedom, and G. L. Matthaei, "New equivalent circuits for elementary piezoelectric transducers," *Electronic Letters*, vol. 6, no. 13, p. 2, 1970.

[117] J. M. Galliere, L. Latorre, and P. Papet, "A 2D KLM model for disk-shape piezoelectric transducers," in *Advances in Circuits, Electronics and Micro-Electronics*, pp. 40–44, IEEE, 2009.

[118] W. Shi, H. Shekhani, H. Zhao, J. Ma, Y. Yao, and K. Uchino, "Losses in piezoelectrics derived from a new equivalent circuit," *Journal of Electroceramics*, vol. 35, 2015.

[119] M. Castillo, P. Acevedo, and E. Moreno, "KLM model for lossy piezoelectric transducers," *Ultrasonics*, vol. 41, no. 8, pp. 671–679, 2003.

[120] S. J. H. van Kervel and J. M. Thijssen, "A calculation scheme for the optimum design of ultrasonic transducers," *Ultrasonics*, vol. 21, no. 3, pp. 134–140, 1983.

[121] J. O. Attia, *Electronics and Circuit Analysis using Matlab*. Boca Raton: CRC Press, 1999.

[122] CeramTec GmbH, Plochingen, Germany, *Material Datasheet SONOX P505*. 2019.

[123] A. R. Selfridge, "Approximate material properties in isotropic materials," *IEEE Transactions on Sonics and Ultrasonics*, vol. 32, no. 3, pp. 381–394, 1985.

[124] H. Wang, T. A. Ritter, W. Cao, and K. K. Shung, "Passive materials for high-frequency ultrasound transducers," vol. 3664, 1999.

[125] E. L. Kinsler, *Fundamentals of Acoustics*. John Wiley and Sons, 4th ed., 2000.

[126] ONDA Cooperation, *Hydrophone Handbook*. CA, USA, 2015.

[127] N. N. Abboud, G. L. Wojcik, D. K. Vaughan, J. Mould, D. J. Powell, and L. Nikodym, "Finite element modeling for ultrasonic transducers," in *1998 Proceedings of SPIE medical imaging*, vol. 3341.

[128] R. McKeighen, "Finite element simulation and modeling of 2-D arrays for 3-D ultrasonic imaging," *IEEE Transactions on Ultrasonics, Ferroelectrics, and Frequency Control*, vol. 48, no. 5, 2001.

[129] COMSOL, "Multiphysics Reference Manual v5.6," report, Comsol Inc., 2020.

[130] P. Langer, M. Maeder, C. Guist, M. Krause, and S. Marburg, "More than six elements per wavelength: The practical use of structural finite element

models and their accuracy in comparison with experimental results," *Journal of Computational Acoustics*, vol. 25, no. 04, p. 1750025, 2017.

[131] COMSOL Inc., *Tonpilz transducer example*. [https://www.comsol.de/model/piezoelectric-tonpilz-transducer-11478], Accessed in 09/2021.

[132] A. D. Nashif, D. I. Jones, and J. P. Henderson, *Vibration Damping*. John Wiley and Sons, 1986.

[133] B. C. Chakraborty and R. Debdatta, *Polymers for Vibration Damping Applications*. Amsterdam: Elsevier, 2020.

[134] L. H. Sperling and C. D. R., "Sound and vibration damping with polymers," *ACS Symposium Series*, vol. 424, pp. 5–22, 1990.

[135] K. P. Menard, *Dynamic Mechanical Analysis: A Practical Introduction*. Boca Raton: CRC Press LLC, 1999.

[136] J. F. Guess and J. S. Campbell, "Acoustic properties of some biocompatible polymers at body temperature," *Ultrasound in Medicine and Biology*, vol. 21, no. 2, pp. 273–277, 1995.

[137] T. Szabo and J. Wu, "A model for longitudinal and shear wave propagation in viscoelastic media," *The Journal of the Acoustical Society of America*, vol. 107, pp. 2437–46, 2000.

[138] X. Liu and Q. Feng, *Chapter 12 - Statistical energy analysis of tire/road noise*, pp. 271–296. Butterworth-Heinemann, 2020.

[139] COMSOL Inc., *Damping in Structural Dynamics: Theory and Sources*. [https://www.comsol.com/blogs/damping-in-structural-dynamics-theory-and-sources/], 2019.

[140] N. V. Ruiter, R. Dapp, M. Zapf, and H. Gemmeke, "Evaluation of 3D point spread function of a semi-ellipsoidal ultrasound computer tomography system," in *2011 IEEE International Ultrasonics Symposium (IUS)*, pp. 242–245.

[141] Y. Zhang, L. Wang, L. Qin, C. Zhong, and S. Hao, "Spherical–omnidirectional piezoelectric composite transducer for high-frequency underwater acoustics," *IEEE Transactions on Ultrasonics, Ferroelectrics, and Frequency Control*, vol. 68, no. 5, pp. 1791–1796, 2021.

[142] R. De Luca, M. Bassani, L. Francalanci, F. Bertocci, F. Gelli, P. Palchetti, D. Coppini, and L. Bocchi, "A mathematical model for reverberations in biomedical ultrasound transducers: a case study," IEEE, 2018.

[143] Matweb, *Overview of materials for Thermoplastic Polyurethane*. [https://www.matweb.com/search/datasheetText.aspx?bassnum=O5040], Accessed on 12/2021.

[144] P. N. Sherlock, *Relaxor-PT Single Crystals for Broad Bandwidth, High Power Sonar Projectors*. PhD thesis, 2010.

[145] P. C. Eccardt and K. Niederer, "Micromachined ultrasound transducers with improved coupling factors from a CMOS compatible process," *Ultrasonics*, vol. 38, no. 1, pp. 774–780, 2000.

[146] S. G. Ergun, G. G. Yaralioglu, and P. Khuri-Yakub, "Capacitive micromachined ultrasonic transducers: Theory and technology," *Journal of Aerospace Engineering*, vol. 16, no. 2, pp. 76–84, 2003.

[147] V. J. Qiu, Y.and Gigliotti, F. Wallace, M.and Griggio, E. M. C. Demore, S. Cochran, and S. Trolier-McKinstry, "Piezoelectric micromachined ultrasound transducer (PMUT) arrays for integrated sensing, actuation and imaging," *Sensors*, vol. 15, no. 4, 2015.

[148] J. Jung, W. Lee, W.and Kang, E. Shin, J. Ryu, and H. Choi, "Review of piezoelectric micromachined ultrasonic transducers and their applications," *Journal of Micromechanics and Microengineering*, vol. 27, no. 11, 2017.

[149] K. Brenner, A. Ergun, K. Firouzi, M. Rasmussen, Q. Stedman, and B. Khuri–Yakub, "Advances in capacitive micromachined ultrasonic transducers," *Micromachines*, vol. 10, no. 2, p. 152, 2019.

[150] J. Luo, S. J. Zhang, T. R. Shrout, and W. S. Hackenberger, "Advances in manufacturing relaxor piezoelectric single crystals," in *2007 Sixteenth IEEE International Symposium on the Applications of Ferroelectrics*, pp. 557–560.

[151] CTS Corporation, "Piezoelectric PMN-PT single crystal product brochure and datasheet," Accessed in 07/2022.

[152] Ibule, Inc., "Datasheet PMN-PT," Accessed in 07/2022.

[153] E. Ledesma, I. Zamora, F. Torres, A. Uranga, V. Tzanov, N. Barniol, E. Marigo, and M. Soundara-Pandian, "AlN piezoelectric micromachined ultrasonic transducer array monolithically fabricated on top of pre-processed CMOS substrates," in *2019 20th International Conference on Solid-State Sensors, Actuators and Microsystems*, pp. 655–658.

[154] E. Ledesma, I. Zamora, V. Tzanov, F. Torres, A. Uranga, N. Barniol, E. Marigo, and M. Soundara-Pandian, "Liquid operable aln pmut with high output pressure capabilities," in *IEEE International Ultrasonics Symposium (IUS)*, IEEE.

[155] E. Ledesma, I. Zamora, A. Uranga, and N. Barniol, "Tent-plate aln pmut with a piston-like shape under liquid operation," *IEEE Sensors Journal*, 2020.

[156] D. Horsley, Y. Lu, and O. Rozen, *Flexural Piezoelectric Resonators*, pp. 153–173. Springer International Publishing, 2017.

[157] A. Das, *Characterization and Modeling of Piezoelectric Micromachined Ultrasound Transducer*. Master Thesis, Karlsruhe Institute of Technology, 2021.

[158] I. Zamora, E. Ledesma, A. Uranga, and N. Barniol, "Monolithic single PMUT-on-CMOS ultrasound system with +17 dB SNR for imaging applications," *IEEE Access*, vol. 8, 2020.

[159] D. S. Lin, X. Zhuang, S. H. Wong, M. Kupnik, and B. T. Khuri-Yakub, "Encapsulation of capacitive micromachined ultrasonic transducers using viscoelastic polymer," *Journal of Microelectromechanical Systems*, vol. 19, no. 6, 2010.

[160] M. F. l. Cour, M. B. Stuart, M. B. Laursen, S. E. Diederichsen, E. V. Thomsen, and J. A. Jensen, "Investigation of pdms as coating on CMUTs for imaging," in *2014 IEEE International Ultrasonics Symposium*, pp. 2584–2587.

[161] G. Luo, Y. Kusano, and D. Horsley, "Immersion PMUTs fabricated with a low thermal-budget surface micromachining process," in *2018 IEEE International Ultrasonics Symposium*, pp. 1–4.

[162] E. Ledesma, I. Zamora, A. Uranga, and N. Barniol, "9.5 % scandium doped ALN PMUT compatible with pre-processed CMOS substrates," in *2021 IEEE 34th International Conference on Micro Electro Mechanical Systems*, pp. 887–890.

[163] S. Sadeghpour, P. Pobedinskas, K. Haenen, and R. Puers, "A piezoelectric micromachined ultrasound transducers (pMUT) array, for wide bandwidth underwater communication applications," *Proceedings*, vol. 1, no. 4, 2017.

[164] G. Caliano, A. S. Savoia, C. Longo, A. Caronti, M. Pappalardo, A. Iula, and S. Rothmann, "cMUT sensor for applications as a wide-band acoustic receiver in the MHz range," in *2010 IEEE International Ultrasonics Symposium*, pp. 1869–1872.

[165] M. S. Salim, M. F. Abd Malek, R. B. W. Heng, K. M. Juni, and N. Sabri, "Capacitive micromachined ultrasonic transducers: Technology and application," *Journal of Medical Ultrasound*, vol. 20, no. 1, pp. 8–31, 2012.

[166] A. S. Erguri, H. Yongli, Z. Xuefeng, O. Oralkan, G. G. Yarahoglu, and B. T. Khuri-Yakub, "Capacitive micromachined ultrasonic transducers: fabrication technology," *IEEE Transactions on Ultrasonics, Ferroelectrics, and Frequency Control*, vol. 52, no. 12, pp. 2242–2258, 2005.

[167] M. M. Chang, M. T. Deng, J. T. Gwo, J. D. Mai, and E. Hsu, "Polymer-based capacitive micromachined ultrasonic transducers (CMUT) for micro surgical imaging applications," in *2006 1st IEEE International Conference on Nano/Micro Engineered and Molecular Systems*, pp. 61–65.

[168] D. A. Hutchins, D. R. Billson, R. J. Bradley, and K. S. Ho, "Structural health monitoring using polymer-based capacitive micromachined ultrasonic transducers (CMUTs)," *Ultrasonics*, vol. 51, no. 8, pp. 870–877, 2011.

[169] C. D. Gerardo, E. Cretu, and R. Rohling, "Fabrication and testing of polymer-based capacitive micromachined ultrasound transducers for medical imaging," *Microsystems and Nanoengineering*, vol. 4, no. 1, 2018.

[170] A. Omidvar, C. D. Gerardo, R. Rohling, E. Cretu, and A. J. Hodgson, "Flexible polymer-based capacitive micromachined ultrasound transducers (polyCMUTs): Fabrication and characterization," in *2021 IEEE International Ultrasonics Symposium*, pp. 1–4.

[171] W. P. Mason, *Electromechanical Transducers and Wave Filters*. New York: D. Van Nostrand Corp., 1942.

[172] D. M. Pozar, *Microwave Engineering*. University of Massachusetts at Amherst: John Wiley and Sons Inc., 2012.

[173] J. L. San Emeterio and A. Ramos, *Models for Piezoelectric Transducers Used in Broadband Ultrasonic Applications*, pp. 55–67. Berlin, Heidelberg: Springer, 2004.

[174] Epoxy Technology, “Tech tipp 19: Understanding mechanical properties of epoxies for modeling, finite element analysis (FEA),” report, 2015.

[175] J. Karpiesiuk, “Young’s modulus and poisson’s ratio of polyurethane adhesive in lightweight floor system,” *Technical Transactions*, pp. 1–14, 2020.

Acknowledgments

First of all, I would like to thank my advisor Dr. Nicole Ruiter. I am very grateful for all the support, encouragement and guidance in the various endeavors during my PhD. Also many thanks to my main supervisor Prof. Marc Weber for the support and valuable feedback, especially in the final phase of the thesis, and my co-supervisor Prof. Ulrich Lemmer. Many thanks to the IEEE-UFFC society and the KSETA graduate school for the extensive training programs, and Prof. Carl Herickhoff for the great mentorship experience. Furthermore, many thanks to Prof. Nuria Barniol and Prof. Edmond Cretu for enabling two exciting research stays.

Special thanks to all my colleagues of the Software Methods group. Thanks to Nima Rashvand for the great experience in sharing an office, thanks to my fellow PhD colleagues Olga Molchanova, Zewei Lu and Sarah Said for sharing the excitement (and sometimes burden) of conducting a PhD. Thanks to Michael Zapf for the various discussions, relentless feedback loops and the energy in improving my scientific scope. Thanks to Dr. Torsten Hopp, Prof. Hartmut Gemmeke, Dr. Patrick Pfistner and Simon Kraft for all the fruitful discussions and support, I really enjoyed my time in the group! Furthermore, I would like to thank all colleagues at IPE, especially Benjamin Leyrer, Bernhard Osswald, Peter Hoffmann, Klaus Schlote-Holubek and the admin team for their relentless support in the last years.

Moreover, I would like to thank my family and friends, especially my parents Fridolin and Renate Angerer for all the encouragement, and the "Grandpa Herb" team for still sharing adventures. Finally, thank you Ilaria Lucarelli for all your sympathy, patience and energy during this exciting time of my life.